Stony Brook University

Exploring Systematic Effects in Thermonuclear Supernovae

A Dissertation Presented

by

Aaron Perry Jackson

to

The Graduate School

in Partial Fulfillment of the

Requirements

for the Degree of

Doctor of Philosophy

in

Physics

Stony Brook University

August 2011

Stony Brook University

The Graduate School

Aaron Perry Jackson

We, the dissertation committee for the above candidate for the Doctor of Philosophy degree, hereby recommend acceptance of this dissertation.

Alan Calder – Dissertation Advisor
Assistant Professor, Department of Physics and Astronomy

Michael Zingale – Chairperson of Defense
Assistant Professor, Department of Physics and Astronomy

Jin Koda
Assistant Professor, Department of Physics and Astronomy

Dean Townsley
Assistant Professor, Department of Physics and Astronomy
The University of Alabama, Tuscaloosa, AL

Xiangmin Jiao
Assistant Professor, Department of Applied Mathematics and Statistics

This dissertation is accepted by the Graduate School.

Lawrence Martin
Dean of the Graduate School

Abstract of the Dissertation

Exploring Systematic Effects in Thermonuclear Supernovae

by

Aaron Perry Jackson

Doctor of Philosophy

in

Physics

Stony Brook University

2011

Type Ia supernovae (SNe) are bright astrophysical explosions that form a remarkably homogeneous class of objects serving as the premier distance indicators for studying the expansion history of the Universe and the nature of dark energy. Despite the widespread acceptance of the surprising discovery of the acceleration of the expansion of the Universe and the existence of the mysterious dark energy driving it that followed from these studies, the progenitor systems of these explosions are unknown. Knowledge of the progenitor system is required to understand possible systematic effects due to properties of the parent stellar population or host galaxy. While several scenarios have been proposed, the most widely accepted one is the thermonuclear explosion of a near-Chandrasekhar-mass, carbon-oxygen white dwarf (WD). Under this scenario, the explosive burning begins near the center as a deflagration (subsonic burning) that transitions to a detonation (supersonic burning) some time later after the WD has expanded in response to the energy release. Turbulence, either pre-existing or generated by burning, serves to increase the surface area of the burning front, thus enhancing the fuel consumption rate. In addition, turbulence–flame interaction (TFI) may be responsible for deflagration–detonation transition (DDT). Simulations of this explosion scenario typically parameterize the DDT to occur when the flame reaches a particular density.

I performed a suite of two-dimensional (2D) simulations with the compressible, hydrodynamics code FLASH to evaluate the influence of the DDT density on the

average yield of radioactive ^{56}Ni that powers the SN light curve. In addition, I considered the compositional dependence of the DDT density to explore one way in which metallicity may influence the explosion outcome. My results have confirmed a new pathway to explain observed trends in the average peak brightness of SNe Ia with host galaxy metallicity.

In a separate study, I address the basic physics of modeling flames and turbulent combustion. The disparate length scales in the SN necessitate use of a flame model to capture the effect of burning on unresolved scales. I implemented a method to measure the strength of unresolved turbulence, which is used to estimate the amount of wrinkling of the unresolved flame surface. In addition, the measure of turbulent strength may be used to improve the criterion by which DDT is initiated. These improvements will allow three-dimensional (3D) simulations of the early flame evolution in the presence of strong pre-existing turbulence.

The research conducted for this dissertation has led to important insights into the explosion mechanism of SNe Ia. In addition, improvements to the model have allowed and will continue to allow simulations of unprecedented realism of the complex process of exploding WDs in a thermonuclear SN.

To Mr. John Karg, my high school physics teacher,
who continually raised the bar and
never let me earn a perfect score.

And to my loving wife Shona,
who has supported me throughout this experience.

Contents

List of Figures

List of Tables

Abbreviations

SN	supernova
WD	white dwarf
M_{ch}	Chandrasekhar mass
SD	single degenerate
DD	double degenerate
RT	Rayleigh–Taylor
KH	Kelvin–Helmholtz
DDT	deflagration–detonation transition
PPM	piecewise parabolic method
EOS	equation of state
AMR	adaptive mesh refinement
1D	one-dimensional
2D	two-dimensional
3D	three-dimensional
ADR	advection-diffusion-reaction
RD	reaction-diffusion
NSQE	nuclear statistical quasi-equilibrium
NSE	nuclear statistical equilibrium
ZND	Zel'dovich–von Neumann–Döring
TFI	turbulence–flame interaction
SGS	sub-grid scale

Pr Prandtl number

Le Lewis number

Ka Karlovitz number

Re Reynolds number

FIR full inertial range

GS Gibson scale

PLFW power-law flame wrinkling

Acknowledgements

The text of this dissertation in part is a reprint of the materials as it appears in *The Astrophysical Journal* 720:99–113 (2010). The co-authors listed in the publication directed and supervised the research that forms the basis for this dissertation. The publication has been reproduced by permission of the AAS.

I thank Dr. Alan Calder for advising me throughout my dissertation. He has provided support and encouragement. Dr. Dean Townsley has also provided advice, support and enthusiasm for my research. Drs. Frank Timmes, Ed Brown, and David Chamulak have been supportive and responsive collaborators. Thanks to the SUNY Nuclear Astrophysics Research Group for insightful weekly meetings (NAP time) and countless useful discussions. In particular, I appreciate many useful discussions with my officemate and colleague, Brendan Krueger.

This work was supported by NASA through grant NNX09AD19G and by the Department of Energy under grant DE-FG02-87ER40317. The software used in this work was in part developed by the DOE-supported ASC/Alliances Center for Astrophysical Thermonuclear Flashes at the University of Chicago. I thank Nathan Hearn for making his QuickFlash analysis tools publicly available at http://quickflash.sourceforge.net. This work was also supported in part by the US Department of Energy, Office of Nuclear Physics, under contract DE-AC02-06CH11357 and utilized resources at the New York Center for Computational Sciences at Stony Brook University/Brookhaven National Laboratory which is supported by the U.S. Department of Energy under Contract No. DE-AC02-98CH10886 and by the State of New York.

Chapter 1

Introduction

Type Ia supernovae (SNe) are extremely bright astrophysical phenomena that form a remarkably homogeneous class of light curves that are spectroscopically characterized by the absence of hydrogen and presence of a strong silicon P Cygni feature near peak brightness indicative of out-flowing material [1]. Due to their near homogeneity and apparent brightness, these objects were targeted as standard candles. These objects became even more accurate distance indicators when Phillips [2] recognized that brighter SNe Ia tended to fade from view over a longer period of time. This "brighter is broader" property of SN Ia light curves, also known as the Phillips relation, allows a one-parameter empirical fit to infer relative distances among many events, thus named "standardizable" candles. While this empirical fit improves distance estimates, systematic effects exist that are not necessarily accounted for by the fitting procedure. When anchored with independent nearby distance indicators, such as period–luminosity relation in Cepheid Variable stars, SNe Ia determine extragalactic distances to $\sim$ 10% and have led to the discovery that the expansion of the Universe is accelerating [3, 4]. The discovery contradicted expectations that the expansion should decelerate by the force of gravity, triggering a revolution in our understanding of cosmology by indicating that an unknown force dubbed "dark energy" is responsible for the acceleration. SNe Ia have proved to be the best tool to study and quantify the nature of dark energy.

Despite being used as standardizable candles, properties of the SN light curve have been observed to vary systematically with the morphological type of the host galaxy [5]. Observational campaigns have continued to improve the significance of these correlations [see, *e. g.*, 6]; however, much of the underlying cause remains unknown. Understanding these correlations among observables requires knowledge of the explosion mechanism and its sensitivities to the surrounding stellar environment and is one of the goals of the present dissertation. The standardization process of converting a raw light curve to a calibrated one introduces possible systematic errors that must be considered. Because the physics of the explosion is not well understood, the scatter about the Phillips relation may be influenced by properties of the SNe Ia environment such as mean age of the parent stellar population, metallicity, and dust. The better we understand the physical connections between metallicity, age, dust, and the light curve of the event, the more precisely we may calibrate the tools used to probe the properties of dark energy. Contemporary studies require the maximum luminosity of SNe Ia to be known to about 1% in order to distinguish between cosmological model predictions. At present, our understanding of the systematics of SNe Ia is not at this level.

In addition to probing the nature of dark energy, SNe Ia are worthy of study in their own right. The explosion mechanism requires the knowledge of physics gained in laboratory experiments conducted on Earth to predict phenomena in extreme astrophysical regimes that are impossible to test. The study of SN forces current theories of combustion to admit assumptions that may not be valid in the extreme astrophysical limit. This scrutiny allows deeper insight into the complex physical processes that describe turbulent combustion.

The goal of the dissertation research presented here is twofold: to identify systematic effects in the explosion outcome of SNe Ia through computational simulation and to increase realism in the computational method. I will provide the context and scope for my dissertation research in the remainder of Chapter 1 followed by a description of the computational method used to simulate SNe Ia in Chapter 2. Included in Chapter 3 is a peer-reviewed article published in *The Astrophysical Journal* describing an exploration of a systematic effect in the explosion outcome due to metallicity. Chapter 4 is an article submitted to *The Astrophysical Journal* describing an extension to the flame model, a component of the computational method. In Chapter 5, I provide conclusions and direction for future research.

1.1 Observational Evidence

The modern era of SN observation has led to the discovery and classification of many events. The presence of hydrogen in the spectra distinguishes between type I (lacking hydrogen) and type II (with hydrogen). Because hydrogen is the most abundant element in the Universe, relatively few explosion scenarios exist that explain a lack of hydrogen in the resulting spectra. Additional classifications exist, including the presence of a silicon P Cygni feature that defines SNe Ia. In general, SNe Ia have been observed to have high-velocity spectral lines from intermediate mass elements, such as silicon, near maximum light. As the light fades, low-velocity iron group elements appear indicating a stratified ejecta structure with iron-peak nuclei near the center of the explosion and intermediate mass elements in a layer above the core. Most of the iron group elements are in the form of radioactive ^{56}Ni, the total yield of which principally determines the brightness of the explosion. No compact object has ever been observed to be associated with a SN Ia leading to the hypothesis that the energy released during the explosion is greater than the gravitational binding energy of the progenitor star.

In addition, the ejecta mass may be estimated from the observed ejecta velocity and rise-time of the light curve. Most observations of SNe Ia indicate an ejecta mass consistent with the Chandrasekhar mass ($M_{\rm ch} \approx 1.4$ M$_\odot$)—the critical mass at which electron degeneracy pressure can no longer support the weight of the star. Because the majority of SNe Ia observations indicate an ejecta mass of roughly $M_{\rm ch}$ and spectra that lack hydrogen, the explosion is thought to arise from a degenerate stellar core, known as a white dwarf (WD), that is near $M_{\rm ch}$. Due to the overall energy of the explosion, the source is thought to be thermonuclear, rather than gravitational as in core-collapse SNe. Thermonuclear SNe release energy via nuclear fusion of light elements that compose these WDs. In addition, as a WD approaches $M_{\rm ch}$, the central temperature rises sufficiently to ignite ^{12}C. Because temperature in degenerate WD material is essentially independent of density, carbon burning is unregulated and a thermonuclear runaway may occur [7]. The energy immediately released

from fusion is mostly converted to kinetic energy serving to overcome the gravitational binding energy of the WD resulting in no remnant and ejecta velocities $\sim 10,000$ km s^{-1}. The subsequent radioactive decay of ^{56}Ni synthesized during the explosion is responsible for powering the SN light curve, providing the characteristic decline from maximum light [8, 9]. The width–luminosity relation, or Phillips relation [2], is understood physically as originating from having both the luminosity and dominant source of opacity being set by the variable mass of ^{56}Ni synthesized, while the total mass of the WD is fixed [10–13]. The light curves and spectra of SNe Ia are well described by an explosion of a near-$M_{\rm ch}$ ^{12}C-^{16}O WD that yields $\sim 0.3 - 0.8$ M$_\odot$ of radioactive ^{56}Ni.

The use of SNe Ia observations as "standardizable" candles with the Phillips relation to infer distances out to redshift $z \sim 1$ have implied that the expansion of the Universe is accelerating [3, 4, 14–16]. This major scientific break-through relied on the presumption that high-z SNe are statistically equivalent to nearby SNe Ia. Therefore, it is important to identify properties that vary with redshift that influence the explosion outcome. Many observational campaigns have been launched with the goal of increasing the significance of these findings (BAOSS [17, 18]; LOSS [18, 19]; SNLS [20]; CSP [21]; Nearby SN Factory [22]; Skymapper [23]; ESSENCE [24]; STRESS [25]; SDSS-II [26]; SXDS [27, 28]; PQ [29]; CfA [30]; CRTS [31]; PTF [32]; Pan-STARRS; the La Silla SN Search) and the future promises even more (the Dark Energy Survey, LSST, JDEM, see Howell et al. [33]). Distance estimates accurate to $\sim 1\%$ are required to differentiate between competing cosmological models.

The intrinsic luminosity of SNe Ia have long been known to correlate with the morphological type of the host galaxy with early-type galaxies hosting fainter SNe on average than late-type galaxies [5]; however, the underlying reason for this correlation has been difficult to discern. Early-type galaxies tend to be more massive due to previous mergers with other galaxies, while late-type galaxies tend to be less massive. During the merger process, elliptical galaxies are thought to lose much of their gas and dust that prevents further star formation. Therefore, the mean age of the stellar population tends to be older in these galaxies than in late-type galaxies. Additionally, more massive galaxies retain more metals produced in SNe explosions within the gravitational potential well. Therefore, early-type galaxies tend to be more massive, more metal-rich, less dusty, and contain older stars, while late-type galaxies tend to be less massive, less metal-rich, more dusty, and contain actively-forming stars. Apart from considering dust, it is more physical to discuss systematic effects in terms of the parent stellar populations of SNe Ia rather than the morphological type of the host galaxy.

Stellar populations are generally characterized by their age and metallicity, and several observational studies aim to ascertain any correlations of the peak brightness with age and metallicity. Scannapieco and Bildsten [34] and Mannucci et al. [35] find evidence for two populations of SNe Ia differentiated by the mean age of the parent stellar population. Howell et al. [36] find that the younger population of SNe Ia occurring in active star-forming galaxies are brighter on average than the older population with Gallagher et al. [37] finding the progenitor metallicity a weaker effect on the peak brightness. However, it is difficult to measure accurate metallicities for the parent stellar population, both due to the mass-metallicity relationship within galaxies [38] and that the measured metallicity at the time of explosion may not accurately represent the metallicity at the time of progenitor star formation for SNe Ia arising from older stellar populations [39]. The metallicity and/or age may

also influence other properties of the light curve apart from the peak luminosity [40].

In addition to the observed trends of "normal" SNe Ia, several peculiar events have been observed including the sub-luminous SN 1991bg [41], super-luminous SN 1991T [42], Ca-rich SN 2002cx [43], and super-$M_{\rm ch}$ SN 2007if [44]. While these SNe Ia are relatively rare events, they illustrate the uncertainty in the progenitor system and explosion mechanism, and may point to multiple progenitor channels.

1.2 Progenitor Systems

While there is agreement on the energy source of thermonuclear SNe, the progenitor systems that give rise to the explosion remain a mystery. The most straight-forward way to uncover possible systematic effects in the observable spectra and light curve is to identify the progenitor system and understand the explosion mechanism. The possible progenitor systems are generally divided into two categories: single degenerate (SD) [45–47] and double degenerate (DD) [47, 48] (*i. e.*, a binary system composed of either one WD or two), although the direct collision of two WDs in a globular cluster may also produce SNe Ia [49]. A further distinction among explosion models may be made from whether the mass of the WD approaches $M_{\rm ch}$. $M_{\rm ch}$ models have been favored based on estimates of the ejecta mass and that ^{12}C will reach conditions for a thermonuclear runaway before the collapse to a neutron star. However, massive C-O WDs are not thought to form naturally during stellar evolution. Instead, the C-O WD must gain additional mass from a companion after it has formed.

Whelan and Iben [45] initially proposed that SNe Ia may arise from a WD accreting material from its non-degenerate companion through the SD channel. Subsequent work by Nomoto [46] examined the range of accretion rates that may result in a successful SNe Ia. If the accretion rate is too low, a layer of hydrogen or helium will build up on the surface and eventually result in a classical nova explosion or a helium flash. In the case of a nova outburst on a C-O WD, more mass may be lost than accreted resulting in net mass loss from the system [50]. A surface helium detonation (a supersonic reaction front driven by compression waves) may result in a similar event to an SN Ia called a "point Ia" described for a tenth of the brightness of a typical Ia [51]. However, depending on the strength of the detonation, converging compression waves near the center of the sub-$M_{\rm ch}$ WD may create sufficiently high temperatures to launch a second detonation that incinerates the entire WD in the "double detonation" scenario [52]. If the accretion rate is high enough, hydrogen will burn stably as it is accreted. Subsequent shell burning will process the material to carbon and oxygen. On the other hand, if the accretion rate is too high, the accretion efficiency drops due to radiation-driven winds. Since the companion star has to be less massive than the WD on the main sequence for it to be less evolved than the WD, the range of mass configurations and accretion rates are limited and may seem too contrived. However, accretion physics is complex and advances in our understanding may lead to a wider range of scenarios in which a near-$M_{\rm ch}$ WD is achievable through the SD channel.

Iben and Tutukov [47] and Webbink [48] proposed that a near-$M_{\rm ch}$ C-O WD may be achieved through the DD channel via the merger of a binary pair of WDs. However, early investigations by Nomoto and Iben [53] and Saio and Nomoto [54] indicated that carbon may ignite on-edge leading to quiescent burning resulting in an O-Ne-Mg WD that would

eventually collapse rather than explode. Research of SNe Ia have since heavily favored the SD channel; however, recent observations of several peculiar SN including SN 2003fg, SN 2006gz, SN 2007if, and SN 2009dc [44, 55–61] provide evidence for a super-$M_{\rm ch}$ progenitor, which has renewed theoretical interest in the DD channel. Achieving a WD mass that approaches $M_{\rm ch}$ through the DD channel is also problematic. First, the two WDs must be close enough to merge via gravitational radiation within a Hubble time. This configuration relies on detailed binary population synthesis algorithms that treat the common envelope phase with parameterized physics. Second, the tidal disruption and subsequent merger of the less massive WD must yield accretion rates that are not high enough to ignite ^{12}C at the edge, which would lead to an accretion induced collapse rather than an SNe Ia [54, 62, 63]. Recently, Pakmor et al. [64, 65] showed that under certain circumstances, carbon-ignition is expected to launch a detonation which will lead to an SN Ia via the "violent merger" scenario. On the other hand, if the accretion rate is low enough, the primary may accrete enough mass to approach $M_{\rm ch}$ [66]. The system as a whole will contain more than $M_{\rm ch}$ worth of material, which may explain the observational inferences of a super-$M_{\rm ch}$ progenitor. While slowly rotating WDs in the SD channel would be unable to explain a super-$M_{\rm ch}$ progenitor, Liu et al. [67] have explored fast-rotating, super-$M_{\rm ch}$ WDs as possible progenitors of these events.

1.2.1 Explosion Mechanisms of Near-$M_{\rm ch}$ WDs

Regardless of the channel by which a near-$M_{\rm ch}$ WD is formed, these objects appear to best reproduce properties of most SNe Ia. In general, sub-$M_{\rm ch}$ explosion models are sub-luminous SNe Ia due to the flat density structure of the degenerate stellar interior. It is not until a WD nears $M_{\rm ch}$ that its central density increases and subsequent ignition is expected to produce copious amounts of ^{56}Ni that produce "normal" SNe Ia. Here, normal SNe Ia yield ≈ 1 M$_\odot$ of Fe-group material and ~ 0.3 M$_\odot$ of intermediate mass elements such as ^{28}Si. The spectra are stratified with intermediate mass elements observed to expand at $\sim 10,000$ km s^{-1} and Fe-group elements much slower remaining near the center. Because exploding near-$M_{\rm ch}$ WDs naturally recover the observed stratification of ejecta, the discussion is oriented towards explosion mechanisms involving near-$M_{\rm ch}$ WDs.

Various explosion mechanisms of these objects have been proposed with major differences arising from uncertainties as to whether burning is expected to be subsonic or supersonic (*i. e.*, a deflagration or detonation). Once the WD approaches $M_{\rm ch}$ by either channel, the core temperature rises to ignite ^{12}C which begins the thermonuclear runaway [7, 68]. While the explosion is inevitable, a thermonuclear flame is not expected to form until the energy generation rate from ^{12}C-burning exceeds the combined cooling rates from free-streaming neutrinos and convection. By the time the energy generation rate exceeds the cooling rate, the inner $0.8 - 1.0$ M$_\odot$ is fully convective with $\sqrt{\langle v^2 \rangle} \sim 300$ km s^{-1} [69]. The explosion of a near-$M_{\rm ch}$ C-O WD has received the most attention; and therefore, many scenarios have been explored.

Historically, the main question was whether carbon burning proceeded as a detonation [70, 71] or deflagration [72] or some combination of the two [73]. Pioneering work by Nomoto [74], Nomoto et al. [75] ruled out detonation-only models due to the over-production of ^{56}Ni, while the *W7* deflagration-only model (with a prescribed burning velocity) was able

to reproduce inferred ^{56}Ni yields and observed ejecta stratification remarkably well. While the *W7* model has proved to be a useful tool, the burning velocity is essentially tuned to achieve an acceptable result, and has little physical connection to turbulent combustion. Khokhlov [76] argued that a deflagration–detonation transition (DDT) may occur as nuclear burning reaches densities $\rho \sim 10^7$ g cm^{-3}. While *W7* reproduces observations well, Höflich and Khokhlov [77] demonstrated that delayed detonation models provide similar results. These one-dimensional (1D) spherically symmetric models cannot capture the expected fluid mixing. In addition, variations in the yield of ^{56}Ni necessarily arise from changing the burning velocity in the *W7* model or the transition density in the DDT model, neither of which are well-constrained quantities. The push to multidimensional models is a result of increased computing power as well as a desire to remove "free parameters" from the explosion model, thus increasing the reliability of the results. Multidimensional simulations allow the burning propagation velocity to be computed directly, but the extra degree(s) of freedom allow fluid instabilities such as Rayleigh–Taylor (RT) and Kelvin–Helmholtz (KH) to develop and influence the burning rate. Because the ash behind the C-O flame is less dense than the fuel around it, buoyant forces become very important, particularly if the ignition is off-center [78–80]. With particular choices of the initially burned region, multidimensional models with improved treatment of the burning velocity have been able to recover the ejecta stratification and range of ^{56}Ni yields that were desirable features of 1D models [81–84]. Due to the sensitivity of the initially burned region, the primary source of variation in ^{56}Ni yields is likely due to the ignition condition rather than the combustion velocity or transition density. In addition, multidimensional simulations have lead to the realization that deflagration-only models only seem capable of explaining sub-luminous events [85]. A delayed detonation is required to allow the star to expand in response to burning initially, but still sweep through the whole star to process intermediate mass elements like ^{28}Si and leave very little unburnt ^{12}C behind. A few processes by which a delayed detonation may be triggered have been proposed including the DDT [76], the gravitationally confined detonation (GCD) or detonating failed deflagrations [86], and the pulsating reverse detonation [87].

The DDT mechanism through the SD channel is the most widely accepted scenario for SNe Ia due to the success that one-dimensional models have had in reproducing observed features [77]. Through other works, the delayed detonation of a near-$M_{\rm ch}$ C-O WD explains the observed stratification of ejecta, the kinetic energy released, range of peak brightnesses, width-luminosity relation, secondary maximum in the near-infrared, and thermal X-ray emission from SN Ia remnants [13, 88–92]. While much evidence exists to support a delayed detonation explosion mechanism, the evidence for an SD or DD formation channel is less clear and relies on SNe Ia rates, delay times, and population synthesis. In fact, both channels may be important and explain observational evidence for two populations of SNe Ia that differ in the elapsed time between star formation and explosion [34, 35, 93]. However, the difference might be explained as a systematic effect with age (or the time since last star formation) in one progenitor channel [94].

1.3 Systematic Effects

One avenue to explore systematic effects is to explore the dependence of the explosion outcome on properties of the progenitor WD. While this avenue requires the presumption of a particular explosion mechanism, specific predictions may be made concerning correlation between observable properties of SNe Ia. The exploration of the impact of these parameters on the SNe Ia outcome have been the topic of a number studies with a variety of explosion models. Several of these were accomplished in one dimension [95–98]; however, the deflagration phase is subject to fluid instabilities that can only be captured by multi-dimensional simulations. While the sensitivity to the initial conditions poses a challenge to reproduce realistic explosions, it may also be responsible for some of the intrinsic scatter observed in SNe Ia properties. Townsley et al. [99] was the first to explore both realistic explosions and realistic scatter in the outcome in a statistical ensemble of multi-dimensional explosion models (described in Section 2.3). Due to the highly non-linear evolution of multi-dimensional explosion models, a statistical approach must be adopted to study systematic effects in a meaningful way [100]. In contrast, the three-dimensional (3D) study performed by Röpke et al. [101] calculated one explosion for each set of independent parameters in a deflagration-only explosion model, one that reproduces only sub-luminous events. Given the success of the DDT scenario [77], I chose to explore systematic effects presuming this explosion mechanism. Therefore, the following discussion of possible systematic effects will orient around this explosion channel.

Theoretically, there are many parameters that define the properties of the progenitor WD prior to the thermonuclear runaway including WD structure and composition. These properties are influenced by the formation channel of the progenitor system including the progenitor age as well as the metallicity content of the host galaxy. As "standardizable" candles, SNe Ia light curves are described by a one-parameter family of solutions that relates the peak brightness to the width of the light curve (stretch factor) [102] or decline rate from maximum light in the B-band over 15 days (Δm_{15}) [2]. In order to reduce systematic uncertainties in the distances to these events, correlations between the fitting parameter (or peak brightness) and other potential observables such as mean stellar population age, host galaxy metallicity, intrinsic metallicity, intrinsic color variation, and extrinsic color variation due to dust, either in the circumstellar medium (CSM) or interstellar medium (ISM) must be identified and understood. The main goal of exploring systematic effects is to link properties of the progenitor system and parent stellar population to properties of the light curve, a process which requires detailed analysis of stellar evolution as well as the accretion, explosion, and expansion/radiative transfer phases of the event. This process may lead to disentangling intrinsic scatter from extrinsic scatter among the observed correlations. The dissertation research presented here focuses on the analysis of the explosion phase taking as input properties of the WD expected from star formation in the host galaxy, subsequent stellar evolution, and the accretion history. The explosion phase begins with the birth of the thermonuclear flame and ends with the approximate free expansion of material when energy generation has ceased and the kinetic energy has exceeded the gravitational binding energy.

The state of the WD prior to the explosion depends on many factors including the metallicity of the molecular cloud from which the star formed, the main sequence mass of the progenitor star, the time the WD spent in isolation prior to accretion, the accretion

history, and convective ^{12}C burning prior to flame ignition. The mass of the progenitor dictates the main sequence lifetime as well as the mass and compositional structure of C-O WD that forms during the post-main-sequence evolution. A more massive star will form a more massive WD, which during core helium burning will have a higher central temperature favoring ^{16}O over ^{12}C due to the increased $^{12}\mathrm{C}\,(\alpha,\gamma)\,^{16}\mathrm{O}$ rate [103]. In layers outside the core, shell burning on the asymptotic giant branch produces more ^{12}C over ^{16}O due to the reduced temperature and $^{12}\mathrm{C}\,(\alpha,\gamma)\,^{16}\mathrm{O}$ rate. During helium burning, the ^{12}C, ^{14}N, and ^{16}O that accounts for most of the original metallicity is processed to ^{22}Ne [104]. The ^{22}Ne contained in the WD serves as a direct tracer of the metallicity of the main sequence star and of the parent stellar population. Once formed, the WD may experience a period of isolation prior to accretion. Throughout its isolation, the WD continues to cool and becomes more degenerate. Additionally, ^{22}Ne sedimentation, crystallization, and/or C-O separation may influence the WD structure and compositional profile prior to accretion (for example, see Althaus et al. [105]). Lesaffre et al. [106] showed that after the onset of accretion, the central density at the time of ^{12}C-ignition increases with increasing WD cooling time. Additionally, M_{ch} itself depends on metallicity since the metallicity increases the neutron excess—or the number of baryons each electron must support. A WD of the same mass with higher neutron excess will have a higher central density. Additional electron captures take place during convective carbon burning phase just prior to flame ignition increasing the neutron excess further in an amount comparable to that due to the metallicity [107, 108].

Rather than computationally evolve stars from the main sequence that have properties representative of their parent stellar population all the way to carbon ignition, I choose to vary properties of the pre-ignition WD that I believe to be most strongly influenced by the metallicity or mean stellar age. Townsley et al. [99] consider the influence of neutron excess on the energy release and flame speed, while Krueger et al. [94] consider the variation of the central density of the WD at flame ignition. In Chapter 3, I describe the influence of variations in the conditions for DDT due to metallicity. Additionally, the core ^{12}C abundance may be influenced by both the mean stellar age and metallicity and also directly influences DDT, flame speeds, and the overall energy release. An exploration of this effect is planned for future work.

To vary these parameters self-consistently with the mass and metallicity of the progenitor WD is at present too difficult. By instead isolating individual parameters, we may better understand the explosion mechanism, and the influence on the explosion outcome may be incorporated into any theory linking parameters of the pre-ignition WD to the progenitor star's mass and metallicity. Apart from the formation process, the composition influences many physical processes during the explosion itself including the flame-ignition density, DDT, energy release, flame speed, and nucleosynthetic yield. The dynamical effects such as energy release, flame speed, and nucleosynthetic yield are handled self-consistently by the explosion model described in Chapter 2.

Chapter 2

Method

The simulation code FLASH was used to perform the numerical studies of SNe Ia presented in this dissertation. FLASH was originally developed by the ASC/Alliance Center for Astrophysical Thermonuclear Flashes at the University of Chicago [109, 110]. FLASH is an Eulerian code that utilizes a high-order shock-capturing compressible hydrodynamics method, the piecewise parabolic method [PPM, 111], adapted to treat a general equation of state [EOS, 112]. FLASH applies this hydrodynamics method on an adaptively refined, tree-structured, non-moving Eulerian grid managed by PARAMESH [113]. Extensive use is made of this adaptive mesh refinement (AMR) capability, using different resolutions (ranging from $\sim 1 - 1000$ km) for burning fronts, the initial hydrostatic star, and the region of negligible density initially outside the star. For the purpose of studying SNe Ia, a tabulated, fully ionized electron-ion plasma EOS is used [109, 114]. Additional development on the ignition condition, flame model, nuclear energetics scheme, refinement criteria, DDT ignition, and unresolved turbulent-flame interaction are described in this dissertation and Vladimirova et al. [115], Calder et al. [116], Townsley et al. [117], and Townsley et al. [99].

The hydrodynamics module within FLASH solves the fully compressible Euler equations in conservative form

$$\frac{\partial \rho}{\partial t} + \nabla \cdot \rho \boldsymbol{v} = 0, \tag{2.1}$$

$$\frac{\partial \rho \boldsymbol{v}}{\partial t} + \nabla \cdot \rho \boldsymbol{v}\boldsymbol{v} + \boldsymbol{\nabla} p = \rho \boldsymbol{g}, \tag{2.2}$$

$$\frac{\partial \rho E}{\partial t} + \nabla \cdot (\rho E + p)\, \boldsymbol{v} = \rho \boldsymbol{v} \cdot \boldsymbol{g}, \tag{2.3}$$

where ρ is the fluid density, $\boldsymbol{v}$ is the fluid velocity, p is the pressure, E is the sum of the internal energy ϵ and kinetic energy per unit mass

$$E = \epsilon + \frac{1}{2} v^2, \tag{2.4}$$

$\boldsymbol{g}$ is the acceleration due to gravity, and t is the time coordinate. The pressure is a function of density and internal energy given by the EOS. Mass scalars are advected by the flow with

$$\frac{\partial \rho Q}{\partial t} + \nabla \cdot \rho Q \boldsymbol{v} = 0, \tag{2.5}$$

where $0 \leq Q \leq 1$ is any mass scalar, including reaction progress variables used to describe the flame model in Section 2.1. The equations are solved with PPM, a high-order Godunov scheme in which fluxes through cell boundaries are computed by solving Riemann's shock tube problem. The left and right states of the Riemann problem are reconstructed from cell-averaged quantities using a high-order polynomial that recovers the correct cell-average quantity for each cell used in the reconstruction. Multidimensional flows are computing using Strang splitting (or dimensional splitting). Full details of the implementation of this scheme are provided in Fryxell et al. [109].

While FLASH is publicly available, the framework allows for modular components and the inclusion of customized modules. I will highlight some of the important additions provided by myself and collaborators Dean Townsley and Alan Calder including the flame model in Section 2.1, the nuclear energetics scheme in Section 2.2, and the statistical framework in Section 2.3. Additional details concerning tracer particles, nucleosynthesis, refinement criteria for AMR, etc., may be found in Townsley et al. [99], Calder et al. [116], Townsley et al. [117], and in Chapter 3.

2.1 Flame Model

The need for a flame model becomes apparent when the length scales of the target problem are discussed. The explosive event that leads to the observation of a SNe Ia is a macroscopic phenomenon that requires simulation of the full WD star and surrounding space for the star to explode into. The radius of a degenerate WD is $\sim 10^8$ cm, comparable to the size of Earth, while a $^{12}\mathrm{C} + {}^{12}\mathrm{C}$ flame is resolved at $10^{-4} - 10^3$ cm for the relevant density range in the WD [116]. Even with AMR, state-of-the-art 3D calculations obtain resolutions of $\sim 10^5$ cm. Therefore, the physics that describes combustion is unresolvable, and a model that describes the unresolved processes associated with the flame must be constructed.

The flame-capturing model used in this dissertation was originally developed by Khokhlov [118] following an advection-diffusion-reaction (ADR) equation for a reaction progress variable ϕ that increases monotonically from 0 (fuel) to 1 (ash) given by

$$\frac{\partial \phi}{\partial t} + \boldsymbol{v} \cdot \boldsymbol{\nabla} \phi = \kappa \nabla^2 \phi + \frac{1}{\tau} R\left(\phi\right), \tag{2.6}$$

where the reaction term $R(\phi)$, time-scale τ, and diffusion constant κ are chosen so that the front propagates at the desired speed with the desired width. The diffusion constant and reaction timescale are computed dynamically following Vladimirova et al. [115] with $\kappa \equiv sb\Delta x/16$ and $\tau \equiv b\Delta x/16s$, where Δx is the cell width, s is the desired front-propagation speed, and b sets the approximate number of zones desired to resolve the flame. The reaction term is given by

$$R\left(\phi\right) = \frac{f}{4}\left(\phi - \epsilon_0\right)\left(1 - \phi + \epsilon_1\right), \tag{2.7}$$

where $0 < \epsilon_0, \epsilon_1 \ll 1$ and f is an additional factor that depends on ϵ_0 and ϵ_1 and the flame

width to match the behavior of the Kolmogorov Petrovski Piskunov (KPP) reaction term from which this was derived [117]. This formulation results in a fully localized flame front allowing ϕ to take on additional meaning, such as a mass fraction, far from the flame. With this reaction term, the ADR scheme does not need to be corrected for thermal expansion as long as energy is released in proportion to ϕ [115], but $R(\phi)$ is discontinuous at $\phi = 0$ and $\phi = 1$ introducing noise that is controlled by ϵ_0 and ϵ_1. Townsley et al. [117] found that $\epsilon_0 = \epsilon_1 = 10^{-3}$, $f = 1.309$, and $b = 3.2$ provide a well-localized flame at acceptable noise levels.

It is important to note that the ADR scheme is implemented to conserve energy and provide an implicit interface that is resolvable by the computational grid. It is not intended to represent the physics of combustion or mimic the real internal flame structure. That is, the reaction and diffusion terms are not chosen to reflect the physics of the problem. True thickened-flame approaches thicken the real internal flame structure by a fixed amount that may or may not be resolved on the computational domain. While this approach may be advantageous, the ADR scheme presented here has been studied extensively, and it's use with FLASH is well tested [115, 117].

2.2 Nuclear Energetics

For fully resolved calculations, the nuclear flame and energetics would be captured directly by temperature sensitive reaction rates, thermal diffusion, and species diffusion, and would require tracking many nuclear species. For even the simplest reaction networks, typically 13 nuclear species are required to reasonably capture the energy generation rate [109, 119]. Even though the flame is unresolved and replaced with the ADR flame-front model, the memory requirement for even a modest number of nuclear species is prohibitive in large multidimensional calculations. Instead, the nuclear reactions occurring in C-O WDs can be characterized as a 3-stage process beginning with the driving reaction, $^{12}\mathrm{C} + {}^{12}\mathrm{C}$, followed by $^{16}\mathrm{O}$ consumption to nuclear statistical quasi-equilibrium (NSQE), and ending with the relaxation of NSQE to full nuclear statistical equilibrium (NSE). Townsley et al. [117] define three reaction progress variables to represent these burning stages

$$\phi_{fa} = \text{processing fuel to carbon-burning ashes,} \tag{2.8}$$

$$\phi_{aq} = \text{processing of ash to NSQE,} \tag{2.9}$$

$$\phi_{qN} = \text{relaxation of NSQE to full NSE,} \tag{2.10}$$

which release different amounts of energy over different timescales. When the transition to different burning stages is unresolved on the computational domain, the energy release is smeared out and governed by the ADR equation; however, if the transition is resolved, the energy is released over a characteristic timescale relevant for the burning stage [99, 116, 117].

The energy release is dictated by the bulk fluid properties instead of the mass fractions of individual nuclear species. The fluid properties of interest are the number of electrons per baryon, Y_e, the number of fluid ions per baryon, Y_{ion}, and the average nuclear binding energy per baryon, $\bar{q}$. These properties are mass specific and advected by the flow instead of individual nuclear species. The advantage of this approach is that the relevant timescales and

nuclear energy release can be computed accurately once using a large 430-nuclide network for relevant densities and temperatures [116], and then incorporated as a table look-up into multidimensional models where a large network is prohibitive.

Because the $^{12}C + {}^{12}C$ flame is unresolved (hence the motivation for a model flame), the reaction progress variable representing carbon-burning is defined to be equivalent to the reaction-diffusion (RD) front, $\phi_{fa} \equiv \dot{\phi}$. Then, the subsequent burning stages follow with $\phi_{fa} \geq \phi_{aq} \geq \phi_{qN}$. Neutronization (or $\dot{Y}_e$) due to weak reactions occurring in NSE are implemented in a straight-forward fashion since Y_e is advected with the fluid and ϕ_{qN} represents the partial fluid density of material in NSE [116]. Estimates of the final composition may be made from these progress variables and fluid properties after α particles "freeze out" of NSE due to the expanding and cooling material [117]. In particular, Y_e indicates how much material in NSE will be in the form of stable, neutron-rich Fe-group nuclides and how much will be in the form of radioactive ^{56}Ni that powers the light curve [99].

2.3 Statistical Framework

Townsley et al. [99] developed a statistical framework for evaluating systematic effects in the explosion outcome. The framework is designed on the presumption of the DDT explosion mechanism due to the success that 1D models have had in reproducing observations [77]. In these calculations, the DDT is parameterized as occurring once the flame reached a particular density, $\rho_{\rm DDT}$. This parameterization incorporates a theory of the microphysics which predicts a specific range of densities the transition is likely to occur as well as sensitivities to composition and turbulence as described in Section 3.5.2. In 1D simulations, the ignition is necessarily spherically symmetric at the center of the WD, and a range of ^{56}Ni yields are obtained by variations in $\rho_{\rm DDT}$. For higher transition densities, the star does not expand as much by the time DDT conditions are met leading to the synthesis of more Fe-group elements. The DDT density essentially served as a free parameter that could be "dialed" to produce the desired outcome. While some variation is expected from $\rho_{\rm DDT}$, the dominant source of scatter in the yield of ^{56}Ni is thought to arise from variations in the ignition condition. Multidimensional calculations allow an exploration of the outcome of the explosion with more realistic variations arising from an aspherical ignition condition. Townsley et al. [99] choose to specify a unique (although unknown) transition density, such that variations in the ^{56}Ni yield arise from the ignition condition (all else remaining constant). With this formalism, systematic effects due to variations in model parameters may be explored with a distribution of ignition conditions that reproduces a realistic sample population of SNe Ia.

SNe Ia are inferred to produce a range of ^{56}Ni yields between about 0.3 and 0.8 $M_\odot$ [120]; therefore, a somewhat randomized ignition condition is required to reproduce this result. The ignition condition is motivated by the expectation that the pre-existing convection field will spread the flame around during the early deflagration. The initial flame surface is constructed by perturbing a spherically symmetric burned region with spherical harmonics ranging over several modes. In two dimensions, only $m = 0$ spherical harmonics are possible, but two- and three-dimensional formulations are provided normalized to contain the same

amount of power in the perturbations. The position of the flame surface is described by

$$r_{\mathrm{2D}}(\theta) = r_0 + \mathrm{d}r_0 \sum_{l=l_{\min}}^{l_{\max}} A_l Y_l^0(\theta), \tag{2.11}$$

$$r_{\mathrm{3D}}(\theta,\phi) = r_0 + \mathrm{d}r_0 \sum_{l=l_{\min}}^{l_{\max}} \frac{1}{\sqrt{2l+1}} \sum_{m=-l}^{l} A_l^m e^{i\pi\delta_l^m} Y_l^m(\theta,\phi), \tag{2.12}$$

where r_0 is the overall radial size of the ignition region, $\mathrm{d}r_0$ is the magnitude of the perturbations, A_l^m are randomly chosen from a normal distribution centered at 0 with $\sigma = 1$, δ_l^m are chosen from a uniform distribution between -1 and 1. The choice of parameters r_0, $\mathrm{d}r_0$, $l_{\min}$, and $l_{\max}$ to yield a desirable range of explosion outcomes depends on resolution and dimensionality. For full details about the random number generator and further motivation for the choices of these parameters, see Townsley et al. [99]. These ignition conditions provide a well-defined framework from which studies involving systematic variations in model parameters may be conducted. Chapter 3 describes one such study on the variation of the transition density, ρ_{DDT}.

Chapter 3

The Influence of Deflagration to Detonation Density

The transition density is the defining feature of DDT explosion models that have been successful at reproducing observed features of SNe Ia [77, 83, 99]. While many studies infer "favored" values of the DDT density, the mechanism is actively debated and may occur over a wide range of densities if it occurs at all [96, 121–130]. 1D studies that explore the influence of the transition density [*e. g.*, 131] necessarily parameterize the burning velocity during the deflagration phase, and variations in the explosion outcome are directly linked to the transition density. While the transition density is expected to strongly influence the explosion outcome, this study is the first to quantitatively explore its physical effect in multidimensional simulations, where even for the same transition density a range of explosion outcomes is expected. The range of transition densities was chosen to reflect previous estimates, and on the lower end, a limitation of our algorithm.

I led the following investigation with the co-authors' support and encouragement. The co-authors developed, in part, the FLASH code that was used in this investigation. Their modifications of the publicly available FLASH are described in Calder et al. [116] and Townsley et al. [99, 117]. I was responsible for performing all simulations and analysis, and implemented key modifications to the FLASH code that allowed for non-uniform, ^{22}Ne-enriched compositions, as well as an automated algorithm to trigger the transition from deflagration to detonation. Dean Townsley implemented improvements to the burning model described in Section 3.3.1.

The following is reproduced by permission of the AAS.

EVALUATING SYSTEMATIC DEPENDENCIES OF TYPE Ia SUPERNOVAE: THE INFLUENCE OF DEFLAGRATION TO DETONATION DENSITY

Aaron P. Jackson[1], Alan C. Calder[1,2], Dean M. Townsley[3], David A. Chamulak[4,5], Edward F. Brown[5,6], and F. X. Timmes[5,7]

[1] Department of Physics & Astronomy, The State University of New York-Stony Brook, Stony Brook, NY, USA
[2] New York Center for Computational Sciences, The State University of New York-Stony Brook, Stony Brook, NY, USA
[3] Department of Physics & Astronomy, The University of Alabama, Tuscaloosa, AL, USA
[4] Argonne National Laboratory, Argonne, IL, USA
[5] The Joint Institute for Nuclear Astrophysics, Michigan State University, East Lansing, MI 48824, USA
[6] Department of Physics & Astronomy, Michigan State University, East Lansing, MI, USA
[7] School of Earth and Space Exploration, Arizona State University, Tempe, AZ, USA

Received 2010 April 9; accepted 2010 July 6; published 2010 August 5

ABSTRACT

We explore the effects of the deflagration to detonation transition (DDT) density on the production of ^{56}Ni in thermonuclear supernova (SN) explosions (Type Ia supernovae). Within the DDT paradigm, the transition density sets the amount of expansion during the deflagration phase of the explosion and therefore the amount of nuclear statistical equilibrium (NSE) material produced. We employ a theoretical framework for a well-controlled statistical study of two-dimensional simulations of thermonuclear SNe with randomized initial conditions that can, with a particular choice of transition density, produce a similar average and range of ^{56}Ni masses to those inferred from observations. Within this framework, we utilize a more realistic "simmered" white dwarf progenitor model with a flame model and energetics scheme to calculate the amount of ^{56}Ni and NSE material synthesized for a suite of simulated explosions in which the transition density is varied in the range (1–3) $\times 10^7$ g cm^{-3}. We find a quadratic dependence of the NSE yield on the log of the transition density, which is determined by the competition between plume rise and stellar expansion. By considering the effect of metallicity on the transition density, we find the NSE yield decreases by $0.055 \pm 0.004\ M_\odot$ for a $1\ Z_\odot$ increase in metallicity evaluated about solar metallicity. For the same change in metallicity, this result translates to a $0.067 \pm 0.004\ M_\odot$ decrease in the ^{56}Ni yield, slightly stronger than that due to the variation in electron fraction from the initial composition. Observations testing the dependence of the yield on metallicity remain somewhat ambiguous, but the dependence we find is comparable to that inferred from some studies.

Key words: hydrodynamics – nuclear reactions, nucleosynthesis, abundances – supernovae: general – white dwarfs

Online-only material: color figures

1. INTRODUCTION

Type Ia supernovae (SNe Ia) are bright stellar explosions that are characterized by strong P Cygni features in Si and by a lack of hydrogen in their spectra (see Hillebrandt & Niemeyer 2000; Filippenko 1997 and references therein). Observations of SNe Ia (serving as distance indicators; Phillips 1993; Riess et al. 1996; Albrecht et al. 2006) are at present the most powerful and best proven technique for studying dark energy (Riess et al. 1998; Perlmutter et al. 1999; Kolb et al. 2006; Hicken et al. 2009; Lampeitl et al. 2010), and, accordingly, there are many observational campaigns underway striving to gather information about the systematics of these events and to better measure the expansion history of the universe (see Kirshner 2009 and references therein).

The most widely accepted model for these events is the "single-degenerate" scenario, which is the thermonuclear explosion of a white dwarf (WD) composed principally of ^{12}C and ^{16}O that has accreted mass from a companion (for a review of explosion models, see Hillebrandt & Niemeyer 2000; Livio 2000; Röpke 2006). The peak brightness of the supernova (SN) is set by the radioactive decay of ^{56}Ni produced in the explosion to ^{56}Co and then to ^{56}Fe. The empirical "brighter is broader" relation between the peak brightness of the light curve and the decay time from its maximum is understood to follow from the fact that both the luminosity and opacity are set by the mass of ^{56}Ni synthesized in the explosion (Arnett 1982; Pinto & Eastman 2000; Kasen & Woosley 2007). Because of the dependence of the light curve on the amount of radioactive ^{56}Ni synthesized during an explosion and the ability to infer the ^{56}Ni yield from observations (Mazzali et al. 2007), research into modeling thermonuclear SNe typically focuses on the production and distribution of ^{56}Ni as well as other nuclides (such as ^{28}Si) as the measure with which to compare models to observations.

One-dimensional simulations of the single-degenerate case showed that the most successful scenario is an initial deflagration (subsonic reaction front), born in the core of the WD which at some point becomes a (supersonic) detonation, i.e., a deflagration–detonation transition (DDT; Khokhlov 1991; Höflich & Khokhlov 1996). A delayed detonation naturally accounts for the high-velocity Ca features (Kasen & Plewa 2005) and the chemical stratification of the ejecta. While these one-dimensional models are able to reproduce observed features of the light curve and spectra, much of the physics is missing from these models. The presence of fluid instabilities during the deflagration warranted the development of multidimensional models, allowing a physically motivated calculation of the velocity of the burning front and thus removing a free parameter. By relaxing the symmetry constraints on the model, buoyancy instabilities are naturally captured leading to a strong dependence on the initial conditions of the deflagration that often result in too little

expansion of the star by the time DDT conditions used in previous one-dimensional studies are met (Niemeyer et al. 1996; Calder et al. 2003, 2004; Livne et al. 2005). Multidimensional models may reach the expected amount of expansion prior to the DDT with the choice of particular ignition conditions and thus retain the desirable features from one-dimensional models (Gamezo et al. 2004; Plewa et al. 2004; Röpke et al. 2006; Jordan et al. 2008).

Due to the strong dependence on ignition conditions, multidimensional simulations of the DDT model are able to produce a wide range of peak luminosities (via the production of a range of ^{56}Ni yields) consistent with a common explosion mode suggested from observations (Mazzali et al. 2007). Differences in the mass of synthesized ^{56}Ni can follow from properties such as metallicity and central density of the progenitor and/or differences in the details of the explosion mechanism such as the density at which the transition from deflagration to detonation occurs. Timmes et al. (2003) found that metallicity should affect the ^{56}Ni yield based on approximate lepton number conservation. The metallicity sets the fractional amount of material in nuclear statistical equilibrium (NSE) that is radioactive ^{56}Ni. Bravo et al. (2010) found a stronger dependence on metallicity due to a significant amount of ^{56}Ni that is synthesized during incomplete Si burning.

Observational results to date are consistent with a shallow dependence of ^{56}Ni mass on metallicity but are unable to rule out a trend entirely (Gallagher et al. 2005, 2008; Neill et al. 2009; Howell et al. 2009). Determining the metallicity dependence is challenging not only because the effect appears to be small, but also due to the difficulty in measuring accurate metallicities for the parent stellar population and problems with strong systematic effects associated with the mass–metallicity relationship within galaxies (Gallagher et al. 2008). This effect is also difficult to decouple from the apparently stronger effect of the age of the parent stellar population on the mean brightness of SNe Ia (Gallagher et al. 2008; Howell et al. 2009; Krueger et al. 2010). Howell et al. (2009) note that the scatter in brightness of this observed relation is unlikely to be explained by the effect of metallicity. In general, the source of scatter can be explained by the development of fluid instabilities during the deflagration phase that contribute to differing rates of expansion between instances of SNe. However, by considering the effect of metallicity on the DDT density, scatter in the metallicity relation may be enhanced beyond its intrinsic value inferred from fluid instabilities.

Townsley et al. (2009) investigated the direct effect of metallicity via initial neutron excess and found it to have a negligible influence on the amount of material synthesized to NSE. However, the neutron excess sets the amount of material in NSE that favors stable Fe-group elements over radioactive ^{56}Ni. Therefore, the initial metallicity directly influences the yield of ^{56}Ni. In this work, we expand that study to include the potential indirect effect of metallicity in the form of the ^{22}Ne mass fraction (X_{22}) through its influence on the density at which the DDT takes place. To this end, we explore the effect of varying the transition density, a proxy for varying the microphysics that determine the conditions for a DDT. The conditions under which a DDT occurs are still a subject of debate. Niemeyer & Woosley (1997), Niemeyer & Kerstein (1997), and Khokhlov et al. (1997) proposed that a necessary condition is the transition to a distributed burning regime, in which turbulence disrupts the reaction zone of the flame. More recent numerical studies (Pan et al. 2008; Woosley et al. 2009; Schmidt et al. 2010) that describe the conditions for a DDT include dependencies on the turbulent cascade and the growth of a critical mass of fuel with sufficiently strong turbulence. For this study, we assume the DDT density to be the density at which thermonuclear burning is expected to enter the distributed regime. This choice links the explosion outcome to the dynamical evolution of the progenitor density structure during the deflagration phase. By analyzing the effect of transition density on the NSE yield, we can later analyze how the details of the microphysics affect the DDT density. For the purposes of this study, we will consider only the effect of X_{22} on the DDT density. In reality, the ^{12}C mass fraction will also be important in determining the DDT density, but we choose to leave the exploration of the effect of ^{12}C to future work. Many other possible systematic effects exist that are outlined in Townsley et al. (2009), such as the central ignition density (Krueger et al. 2010), which are all held fixed in this study. The interdependence of all of these effects will be considered in the construction of the full theoretical picture in a future study.

We describe the details of our model in Sections 2 and 3, and the properties of our statistical sample in Section 4. We present our findings on the dependence of transition density on NSE yield in Section 5.1. In Sections 5.2 and 5.3, we assume a dependence of the transition density on ^{22}Ne content and construct the functional dependence of the ^{56}Ni yield on metallicity through the ^{22}Ne content. In Section 6, we discuss our conclusions and future work.

2. PARAMETERIZED REALISTIC WHITE DWARF PROGENITOR

In order to include relevant processes in explosion models, we first estimate the compositional profile of the progenitor WD just prior to the birth of the flame. We begin by estimating the compositional profile resulting from the evolution of the post-main-sequence star that later becomes a WD. Recall that the initial metallicity of the star is, by mass, almost entirely in the form of CNO. As a result of the C–N–O cycle, these all end up in helium layers as ^{14}N, the target of the slowest proton capture in the cycle. Subsequent reactions during helium burning convert ^{14}N into ^{22}Ne; therefore, X_{22} is proportional to the initial metallicity of the star (Timmes et al. 2003). The composition of the inner portion of the star ($\approx$0.3–0.4 $M_\odot$) is set during core helium burning resulting in a reduced carbon mass fraction with respect to that of the outer layers, which is set by shell burning on the asymptotic giant branch (see Straniero et al. 2003 and references therein).

At some point after the WD has formed, it begins to accrete material from its companion. As the mass of the accreting WD approaches the Chandrasekhar mass limit, the core temperature and density increase such that carbon begins to fuse. The energy released by carbon burning drives convection in the core. The convective carbon-burning ("simmering") phase lasts approximately 1000 years before the central temperature is high enough to spark a thermonuclear flame (Woosley et al. 2004). During the simmering phase, carbon is consumed from the convective core. Concurrently, though, the convective zone grows with increasing central temperature, pulling in relatively carbon-rich material from the outer layer. Thus, the net effect is to increase the carbon abundance in the convective region. We show the growth of the convective zone in Figure 1, where dashed lines show the compositional profile prior to the simmering phase and the corresponding solid lines show the compositional profile at the start of our simulations of the explosion.

For our WD models, we consider a parameterized three-species compositional structure consisting of ^{12}C, ^{16}O, and ^{22}Ne,

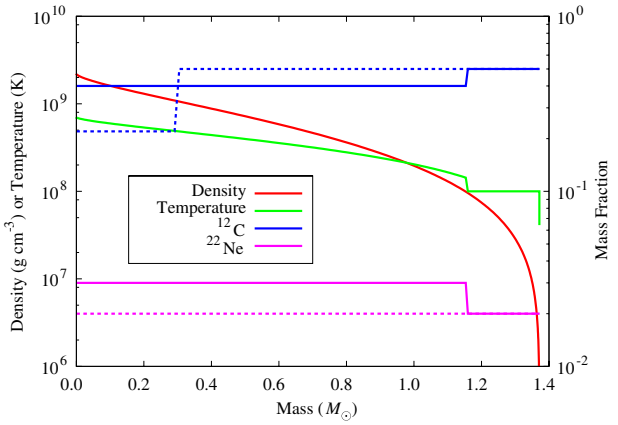

Figure 1. Composition, density, and thermal profiles of the progenitor white dwarf star used in the simulations for this study (solid lines). The compositional profile of the progenitor prior to the simmering phase is also shown (dashed lines).

(A color version of this figure is available in the online journal.)

which is sufficient to capture the nuclear burning rates. Since ^{22}Ne is the only element in our parameterization that has more neutrons than protons, the neutron excess from simmering is accounted for by a parameterized ^{22}Ne mass fraction

$$X'_{22} = X_{22} + \Delta X_{22}(\Delta Y_e), \quad (1)$$

where X_{22} is proportional to the initial metallicity coming from helium burning (Timmes et al. 2003) and $\Delta X_{22}(\Delta Y_e)$ represents the effective enhancement of ^{22}Ne in the core following from the change in electron fraction during convective carbon burning. The electron fraction (Y_e) is related to X_{22} by

$$Y_e = \frac{10}{22} X_{22} + \frac{1}{2}(1 - X_{22}) \quad (2)$$

such that a change in X_{22} constitutes a change in Y_e. The prime on X'_{22} in Equation (1) indicates inclusion of effects of neutronization during carbon burning and this convention applies to the expressions below. We choose the composition of the WD at the end of the simmering phase to consist of $X_{12} = 0.4$ and $X'_{22} = 0.03$ in the core and $X_{12} = 0.5$ and $X'_{22} = 0.02$ in the outer layer. Note that $X_{22} = X'_{22}$ in the outer layer because neutronization due to carbon burning only occurs in the convective core.

For comparison, a compositional profile can be estimated for the WD prior to the onset of carbon burning. For simplicity, consider the production of one neutron for every 6 ^{12}C burned (i.e., $dY_e/dY_{12} \approx 1/6$, where Y_{12} is the molar abundance of ^{12}C) (Chamulak et al. 2008; Piro & Bildsten 2008). For $\Delta X_{22} = 0.01$ in our progenitor model, this constitutes burning 0.04 $M_\odot$ of carbon during simmering. Assuming that prior to simmering, the core mass is $\approx$0.3 $M_\odot$ (Straniero et al. 2003) and the outer layer consists of $X_{12} = 0.5$ material, we can account for all ^{12}C and conserve the total mass of the WD to estimate $X_{12} \approx 0.2$ in the carbon-reduced core of the WD prior to simmering as shown in Figure 1.

Table 1 shows the composition of the progenitor WD before and after the simmering phase using the parameterized ^{22}Ne mass fraction as well as the core mass. Note that throughout this study, we choose to neglect any variation of the amount of neutronization during simmering due to the initial Z. Accordingly, $\Delta X_{22}(\Delta Y_e)$ is treated as a constant and, therefore, $dX'_{22} = dX_{22}$

Table 1
Composition of the Core and Outer Layer of the Progenitor White Dwarf

Evolutionary Stage	Core				Outer Layer		
	X_{12}	X_{16}	X'_{22}	M_c ($M_\odot$)	X_{12}	X_{16}	X'_{22}
Pre-simmering	0.22	0.76	0.02	0.30	0.50	0.48	0.02
Pre-deflagration	0.40	0.57	0.03	1.16	0.50	0.48	0.02

Table 2
Flame Speeds and Widths Changing ^{22}Ne to Carbon-simmering Ashes Holding $Y_e = 0.498636$ Fixed and Using $X_{12} = 0.4$

ρ_9 (g cm^{-3})	s' (km s^{-1})	s (km s^{-1})	Diff. (%)
0.1	0.926	1.012	8.5
0.2	4.194	4.570	8.2
0.3	11.372	12.106	6.1
0.4	18.785	19.466	3.5
0.5	24.352	25.057	2.8
0.6	29.162	29.916	2.5
0.7	33.527	34.322	2.3
0.8	37.571	38.401	2.2
0.9	41.364	42.228	2.0
1.0	44.978	45.871	1.9
ρ_9 (g cm^{-3})	δ' (cm)	δ (cm)	Diff. (%)
0.1	1.4018×10^2	1.3829×10^2	−1.4
0.2	2.7439×10^3	2.4097×10^3	−13.9
0.3	8.5650×10^4	8.1055×10^4	−5.7
0.4	4.6600×10^4	4.9033×10^4	−5.0
0.5	3.5373×10^4	3.4319×10^4	−3.1
0.6	2.6457×10^4	2.5756×10^4	−2.7
0.7	2.0980×10^4	2.0437×10^4	−2.7
0.8	1.7167×10^4	1.6820×10^4	−2.1
0.9	1.4557×10^4	1.4199×10^4	−2.5
1.0	1.2562×10^4	1.2251×10^4	−2.5

Note. Primed quantities parameterize the effects of neutronization during carbon burning as additional ^{22}Ne.

and derivatives involving the true ^{22}Ne mass fraction proportional to metallicity, X_{22}, are equivalent to derivatives involving the parameterized ^{22}Ne mass fraction, X'_{22}.

Because we consider the enhancement of the laminar flame speed by ^{22}Ne (Chamulak et al. 2007), we need to consider the effects of our parameterization of the ^{22}Ne content with care. In actuality, the neutronization during carbon simmering produces ^{13}C, ^{23}Na, and ^{20}Ne and not ^{22}Ne (Chamulak et al. 2008). A priori, this difference could alter the nuclear burning rates and hence the laminar flame speed and width. Table 2 shows the laminar flame speeds and widths for the same Y_e exchanging ΔX_{22} for carbon-simmering ash for a composition of 40% ^{12}C, 2.0% ^{22}Ne, 55.5% ^{16}O, 0.6% ^{13}C, 0.9% ^{20}Ne, and 1.0% ^{23}Na by mass using the same method as described by Chamulak et al. (2007). The flame speeds and widths calculated using the parameterized ^{22}Ne mass fraction (3% by mass) are denoted with primes. For high densities ($\gtrsim 2.5 \times 10^8$ g cm^{-3}) in which the flame speed is not dominated by the buoyancy-driven Rayleigh–Taylor (RT) instability, the difference is $\lesssim$5%; therefore, our parameterization of the neutronization via X_{22} accurately captures the corresponding enhancement of the laminar flame speed in this regime.

While the central temperature and central density of the progenitor just prior to the birth of the flame are primarily set by the accretion history of the WD, which varies and is largely unknown, we choose a fiducial central density of $\rho_c = 2.2 \times 10^9$ g cm^{-3} and central temperature of $T_c = 7 \times 10^8$ K. We construct isentropic profiles of density and temperature in

the (convective) core and isothermal profiles in the (thermally conductive) outer layer while maintaining hydrostatic equilibrium. We choose a fiducial isothermal temperature of the outer layer to be $T_{\rm iso} = 10^8$ K. The total mass of the WD progenitor model is 1.37 $M_\odot$.

Due to the difference in composition between the core and outer layer, requiring a neutral buoyant condition at this interface no longer reduces to a continuous temperature as it does for a compositionally uniform WD (Piro & Chang 2008). In reality, we might expect some convective overshoot and mixing between the core and the outer layer, but because the physics of convective overshoot are complex and not well understood, the width of the transition region is unknown. For simplicity, we assume no mixing region. The composition, density, and thermal profiles of the progenitor used for this study immediately prior to deflagration are the solid lines shown in Figure 1.

3. SIMULATION METHODS

We use a customized version of the FLASH Eulerian compressible adaptive-mesh hydrodynamics code (Fryxell et al. 2000; Calder et al. 2002). Modifications to the code include a nuclear burning model, composition-dependent laminar flame speeds, particular mesh refinement criteria, and instructions for determining the conditions for a DDT (for details, see Calder et al. 2007; Townsley et al. 2007, 2009). In particular, the adaptive mesh refinement (AMR) capability of the code was utilized to achieve particular resolutions for burning fronts (4 km) and the initial hydrostatic star (16 km) for which the solution has converged (Townsley et al. 2009).

The burning model is used for both subsonic (deflagration) and supersonic (detonation) burning fronts. The laminar flame width for densities and compositions characteristic of a massive C–O WD is unresolved on the scale of our grid (4 km; Chamulak et al. 2007); therefore, we use an artificially thickened flame represented by the advection–reaction–diffusion equation (Khokhlov 1995; Vladimirova et al. 2006) to which our nuclear energetics scheme is coupled. Appropriate measures have been taken to ensure this coupling is acoustically quiet and stable such that the buoyant instability of the burning front is accurately captured (Townsley et al. 2007). The shock-capturing capabilities of FLASH naturally handle the propagation of detonation fronts given an accurate nuclear energetics scheme (Meakin et al. 2009). We note that the only common components between our code and that of Plewa (2007) are those publicly available as components of FLASH, which excludes all components treating the nuclear burning; differences are discussed in Townsley et al. (2007).

In this section, we discuss an improvement to our burning model and an improvement to the method by which the transition from deflagration to detonation is made. The changes to the burning model reflect recent work to better match steady-state detonation structures that are partially resolved on the grid. This is important for obtaining accurate particle tracks for post-processing nucleosynthetic yields. Additionally, changes to the DDT method were necessary to ensure consistency between individual simulations using different DDT densities and/or different initial configurations of the flame.

3.1. Improved Burning Model

For the calculations presented here we utilize the latest revision of a parameterized three-stage model for the nuclear burning (Calder et al. 2007; Townsley et al. 2007, 2009; Meakin et al. 2009; Seitenzahl et al. 2009b). The details of this latest version will be published separately (D. M. Townsley et al. 2010, in preparation) along with extensive comparisons to nuclear network calculations of steady-state detonations, but we summarize the major changes here. This work represents the first time a burning model which correctly reproduces the nuclear statistical quasi-equilibrium (NSQE; Khokhlov 1989) to NSE transition timescales and length scales during incomplete silicon burning has ever been used in a multidimensional SN Ia calculation, as validated by comparison to steady-state detonation structures calculated out to the pathological point with the Zel'dovich–von Neumann–Döring (ZND) model (see, e.g., Fickett & Davis 1979). Accurate reproduction of this low-density burning regime is essential because a significant portion of the ^{56}Ni is produced in incomplete burning (Bravo et al. 2010) so that the overall ^{56}Ni yield is determined by the details of how this low-density cutoff of ^{56}Ni production occurs.

Obtaining a satisfactory reproduction of ZND detonation structures involved two main changes to the three-stage burning model. First, we found that the progress variable representing the NSQE to NSE transition, $\phi_{\rm qn}$, which also gives the mass fraction of Fe-group (NSE) material, did not match the time and space structure of this transition in steady-state detonations calculated with a full nuclear network. The kinetics for this stage, first proposed by Khokhlov (1991) and adopted in Calder et al. (2007), are given by the simple form $d\phi_{\rm qn}/dt = (1-\phi_{\rm qn})/\tau_{\rm NSE}$ where $\tau_{\rm NSE}$ is a calibrated timescale that depends mainly on temperature. We have found, however, that a far more appropriate match to steady-state detonations at densities important for incomplete silicon burning, $\rho \lesssim 10^7$ g cm^{-3}, is obtained with the alternative form $d\phi_{\rm qn}/dt = (1-\phi_{\rm qn})^2/\tau_{\rm NSE}$. This necessitates a recalibration of $\tau_{\rm NSE}$, since it now plays a different role, but it is still sufficient for it to depend only on temperature. Although this change in derivative significantly improves the match between the parameterized burning and the ZND structure at the densities of interest, it is still not exact at all densities. It is therefore unclear if this form is indicative of some underlying physical process, and whether or not it is specific to detonations. There are several relaxation processes proceeding simultaneously, so that it is non-trivial to quantify separate contributions. This will be investigated in more detail in future work on post-processing nucleosynthesis.

The second major burning model change was motivated by needing to match the thermodynamic, i.e., T, ρ, profiles at densities at which the portion of the detonation structure representing the NSQE to NSE transition is resolved on the grid. Our previous treatment released all of the nuclear binding energy change to the NSE state by the end of the second stage, leaving the third stage NSQE to NSE transition energetically inert. This lack of an energy release on the NSE timescale leads to an incorrect progression of the density fall-off behind the shock front in the detonation. The abbreviated energy release leads to an underprediction of the temperature immediately behind the unresolved earlier burning stages in a propagating detonation. A very good match of thermodynamic profiles to the full-network steady-state detonation was obtained by tying the completion of the energy release to $\phi_{\rm qn}$, so that energy release occurs in three distinct stages. Note that the previous change involving the kinetics used for $\phi_{\rm qn}$ is also an important contributor to the realism of the thermodynamic profiles obtained.

Finally, although detailed nucleosynthesis based on post-processing tracer particle histories will be published in future work (D. M. Townsley et al. 2010, in preparation), we have

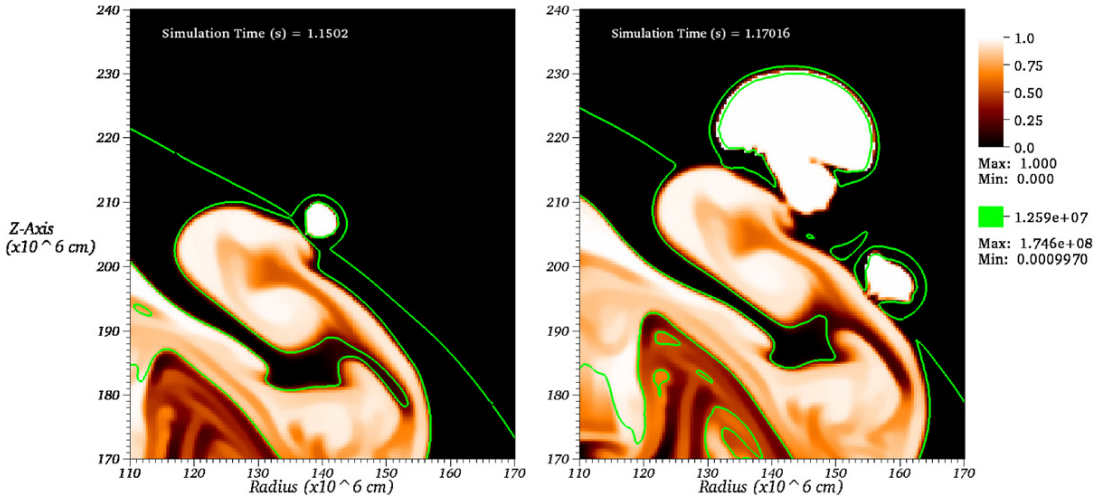

Figure 2. Snapshots of realization 2 just after one (left) and then another (right) detonation were ignited at the specified transition density of 1.26×10^7 g cm^{-3} (green contour). The reaction progress variable representing carbon burning is in color. The detonating regions are the rapidly expanding regions of completely burned carbon ahead of the plume.

(A color version of this figure is available in the online journal.)

performed two important tests for the burning model used in this work. The composition profiles obtained from post-processed histories for hydrodynamic simulations of steady-state detonations match the steady-state structure calculated via the ZND method with a large network with remarkable accuracy. Additionally, a preliminary version of the post-processing under development has been applied to the calculations presented here, and we have found good agreement between $\phi_{\rm qn}$ and the fraction of material in the form of Fe-group nuclides found from post-processing on both an overall basis and in ejection velocity bins. Overall, the burning model changes led to a modest but significant (around 0.2 $M_\odot$) increase in the overall Fe-group yields for the same explosion. The yields found here are not quite this much higher than similar cases from Townsley et al. (2009) because the progenitors used here have a lower central carbon fraction.

3.2. Improved Detonation Ignition Conditions

In order to study the systematic effects associated with changing the DDT density, we need to minimize any systematics in our method of starting a detonation. Previously, in Townsley et al. (2009), we visualized the simulation data from the deflagration phase and plotted a density contour at the DDT density. When the flame reached ≈64 km away from the contour, we picked a computational cell half-way between the flame front and the DDT density contour to place a detonation ignition point with a radius of 8 km. The placement and size of the detonation point was chosen to be as close to the flame front as possible while still allowing the detonation point to develop into a self-sustained, stable detonation front. If the detonation point is placed too close to the flame front, then the flame will interact with the detonation point before it develops into a self-sustained detonation. Comparisons of simulations from identical initial conditions with 8 and 12 km ignition radii finds the NSE yield differs by $\lesssim$0.5% throughout the evolution. This results indicates that the total yield is insensitive to the choice of detonation ignition radius for radii less than the characteristic size of a rising plume (as can be seen in Figure 2). We adopt 12 km for the detonation ignition radius in our study as it produces more robust detonations at low density.

To ensure that we do not introduce unintended systematic effects in this study, we improve our method of detonation ignition point placement over the previous "by hand" method by precisely defining the criteria for a DDT that is used in an algorithm. Parameters in this algorithm are chosen to be consistent with Townsley et al. (2009). Once the flame front reaches the specified DDT density in a simulation, a detonation is ignited 32 km radially outward away from the flame front. Here the reaction–diffusion (RD) front is defined by the variable representing progress of the subsonic burning wave, $\phi_{\rm RD}$, with the leading edge defined as the region between the values 0.001 and 0.01 of this variable. During the deflagration phase of a simulation, $\phi_{\rm RD}$ is equivalent to the carbon-burning reaction progress variable, ϕ_{fa}. At the leading edge of the RD front, very little carbon has burned and the local density is approximately equal to the unburned density. This provides a definition of the DDT density that is much more precise and accurate. We chose these criteria that ignite the detonation ahead of the RD front to avoid any issues with the detonation ignition point overlapping with the artificially thickened flame. If we were to choose criteria that would initiate a detonation inside a thickened flame, the detonation structure would need to be altered in some way to be consistent with the artificial nature of that region.

Our detonation ignition conditions also restrict detonation ignition points to be at least 200 km away from each other. This choice ensures that each rising plume starts 2–3 detonations, which is consistent with Townsley et al. (2009). In the case that multiple points within 200 km meet the detonation ignition conditions, the point furthest from the center of the star is preferred ensuring the ignition of detonations on plume "tops." In reality, the location of the spontaneous detonation points is not well known and is the subject of active research. For instance, Röpke et al. (2007) argue that a spontaneous detonation is triggered by the extreme turbulence found in the roiling fuel underneath the plume caps. Under the assumption that the DDT occurs when the flame reaches the low density for distributed burning, we place ignition points on the tops of the rising plumes. Future studies, however, will explore other physically motivated detonation methods in which the location of the detonation ignition is not necessarily specified relative to a plume, but

rather determined by the local turbulence field, composition, density, and temperature (Röpke et al. 2007; Woosley et al. 2009). Figure 2 shows the placement of first one detonation point, and then another more than 200 km away from the first, both at the specified DDT density.

Each detonation ignition point is defined by the profile of the reaction progress variable representing carbon burning, ϕ_{fa}. Within the detonation ignition radius $\phi_{fa} = 1$, and, because we are igniting in fuel, $\phi_{fa} = 0$ outside this region. The subsequent energy release from this change in ϕ_{fa} drives a shock strong enough to ignite the surrounding unburned material. This top-hat profile is a simple approach to igniting a detonation and has some drawbacks. At densities below $\approx 10^7$ g cm^{-3}, this detonation ignition method does not produce a sufficiently strong shock to burn the fuel. The improvements to our DDT method place the detonation point radially outward from the specified DDT density; therefore, the density within the detonation point is actually somewhat less than that specified by the DDT density. This differs from the method described in Townsley et al. (2009) in that the detonation point was placed at a density that was somewhat higher than the specified DDT density. Igniting a detonation specifying a DDT density below $10^{7.1}$ g cm^{-3} is impossible using a top-hat profile because the detonation ignition point is actually placed $\approx 10^7$ g cm^{-3}. In future works, we will explore the use of a gradient in ϕ_{fa} motivated by Seitenzahl et al. (2009a) to describe the detonation ignition point profile which should result in the formation of stronger shocks that will burn the surrounding low-density fuel.

4. PROPERTIES OF STATISTICAL SAMPLE AND METHOD

To study the systematic effect of transition density on the ^{56}Ni yield synthesized during a simulated explosion, we utilize the statistical framework developed in Townsley et al. (2009). In order to compare results between this study and Townsley et al. (2009), we use the same sample population using the same initial seed. The initial seed defines the starting point to a stream of random numbers used to characterize our sample population of thermonuclear SNe as described in Townsley et al. (2009). In that study, we found that the sample dispersion in the estimated NSE yield does not asymptote until more than 10 realizations. Accordingly, our sample is made up of 30 realizations.

During the early part of the deflagration phase ($\approx$0.1 s), the flame is most affected by convective motion in the core of the WD. Because the velocity field in the core and the number of ignition points are largely uncertain, we choose to characterize the initial flame surface using spherical harmonics, each with a random coefficient picked sequentially from the initial seed. Each realization is defined with a unique perturbation on the initial spherically symmetric flame surface using

$$r(\theta) = r_0 + a_0 \sum_{l=l_{\rm min}}^{l_{\rm max}} A_l Y_l^0(\theta), \quad (3)$$

where r_0 is the radius of flame surface, a_0 is the amplitude of the perturbations, A_l is a randomly chosen coefficient corresponding to the spherical harmonic Y_l^0, and $l_{\rm min}$ and $l_{\rm max}$ set the range of spherical modes used to perturb the flame surface. This method serves to initialize RT-unstable plumes of random relative strengths, which we would expect from various distributions of ignition points and varying strengths of the convective velocity field found in the real population of progenitors. In this study, $r_0 = 150$ km, $a_0 = 30$ km, $l_{\rm min} = 12$, and $l_{\rm max} = 16$. The choices of these parameters are motivated by the resolution of our study and the desire to obtain reasonable ^{56}Ni yields inferred from observations. These choices are discussed in further detail in Townsley et al. (2009).

We choose to analyze the dependence on transition density by choosing five different transition densities equidistant in log space at $\mathcal{L}\rho_{\rm DDT} = \{7.1, 7.2, 7.3, 7.4, 7.5\}$ in cgs units, where $\mathcal{L}\rho_{\rm DDT} = \log_{10}\rho_{\rm DDT}$. The range of DDT densities chosen for this study is motivated both by previous work and computational challenges. Below $\mathcal{L}\rho_{\rm DDT} = 7.1$, a more realistic detonation structure is needed to successfully launch a detonation wave as described in the previous section and in Seitenzahl et al. (2009a). While recent studies have suggested a wider range of DDT densities are possible (Pan et al. 2008; Schmidt et al. 2010), we suggest that trends resulting from varying the DDT density are captured with a maximum $\mathcal{L}\rho_{\rm DDT} = 7.5$.

A simulation is performed for each of the 30 realizations in our sample at each DDT density for a total of 150 simulations. We choose not to explore DDT densities below this specified range for computational reasons. Because of the approximate power-law density profile of the WD, DDT densities were chosen in log space because these densities correspond to relatively evenly spaced radial coordinates of the WD. The amount of ^{56}Ni synthesized in the explosion principally depends on the amount of expansion during the deflagration phase. Therefore, spatially separated detonation ignition conditions will allow the amount of expansion to vary a non-negligible amount and we can more easily analyze the dependence of the yield on DDT density.

We find that extrapolating our results to a DDT density of $\mathcal{L}\rho_{\rm DDT} = 6.83$ yields an estimated average ^{56}Ni yield of $\simeq 0.60\,M_\odot$ with a standard deviation of $0.21\,M_\odot$ (from the fits described below and listed in Table 4) that is consistent with observations (Howell et al. 2009). Because the actual DDT density is unknown and the subject of ongoing research (Pan et al. 2008; Aspden et al. 2008, 2010; Woosley et al. 2009; Schmidt et al. 2010), we are free to choose this value of the DDT density as the fiducial DDT density, $\mathcal{L}\rho_{\rm DDT,0} = 6.83$. This choice is relevant for analysis and comparison to other works as discussed in Section 5. The distribution of ^{56}Ni material synthesized during the explosion is shown in Figure 3 for different transition densities at $\mathcal{L}\rho_{\rm DDT} = 6.83$, 7.10, and 7.30.

The NSE mass, $M_{\rm NSE}$, is defined as $\int \phi_{\rm qn}\rho dV$ integrated over the star. We determine the NSE yield by running the simulation until $M_{\rm NSE}$ is no longer increasing as a function of simulation time. This condition is defined as

$$\frac{dM_{\rm NSE}}{dt} < 0.01\frac{M_\odot}{s}. \quad (4)$$

Because we estimate the ^{56}Ni yield as a fraction of the NSE yield, we consider the ^{56}Ni yield to have plateaued when the NSE yield has plateaued. Considering additional ^{56}Ni from incomplete Si burning in NSQE material and the efficient capture of excess neutrons onto Fe-group elements changes the final ^{56}Ni estimate by $\lesssim$1%. Therefore, to good approximation, the ^{56}Ni yield is a fraction of the NSE yield. Figure 4 shows the evolution of the NSE yield as a function of simulation time showing the DDT time and the NSE yield plateau time for each DDT density for realization 2. Discernible from this figure, there is a clear dependence of the NSE yield on transition density.

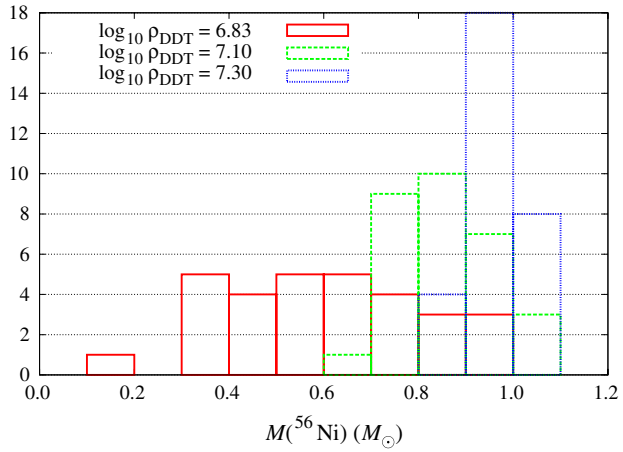

Figure 3. Distributions of the ^{56}Ni yield for three different transition densities $\rho_7 = 0.76$ (solid), 1.26 (dashed), and 2.00 (dotted). Note that the variance increases with decreasing transition density. The distribution corresponding to $\rho_7 = 0.76$ is calculated by extrapolating the dependence of DDT density as described in Section 5.1 such that the mean $M(^{56}\mathrm{Ni}) \simeq 0.60\,M_\odot$ is consistent with observations.

(A color version of this figure is available in the online journal.)

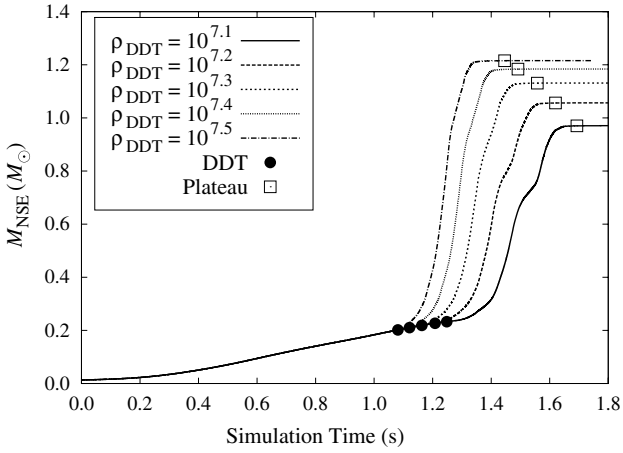

Figure 4. NSE yields for realization 2 at each transition density used in this study. The closed circles indicate the time the flame first reaches the DDT density. The open squares show the time the NSE yield has plateaued as defined by Equation (4).

5. RESULTS

Within the DDT paradigm for thermonuclear SNe, the conditions under which a transition occurs are still not completely understood (Aspden et al. 2008, 2010). Generally, though, a hypothesized transition occurs when the flame enters the distributed burning regime, which occurs when the flame speed equals the turbulent velocity at the scale of the flame width assuming a Kolmogorov turbulent cascade (Niemeyer & Woosley 1997). Recent work has placed more stringent requirements on the DDT (Pan et al. 2008; Woosley et al. 2009; Schmidt et al. 2010) and fundamental questions concerning deflagration in the limit of disruptive turbulence remain (Poludnenko & Oran 2010). Regardless of the actual DDT mechanism, it is likely that the DDT conditions will depend on composition because both the width and burning rate of the flame depend on the abundances ^{12}C and ^{22}Ne. For the current study, we assume that a DDT will occur at a unique density given a particular composition, regardless of the microphysics involved. This assumption is reasonable given that the characteristics of the flame depend strongly on density. Using this assumption, we can delay the analysis of the particular microphysics that lead to a specific transition density and analyze the dependence of the amount of material synthesized to NSE during the explosion on the transition density. Therefore, we can think of each transition density as a proxy for changing the composition that determines the conditions for a DDT via the appropriate microphysics.

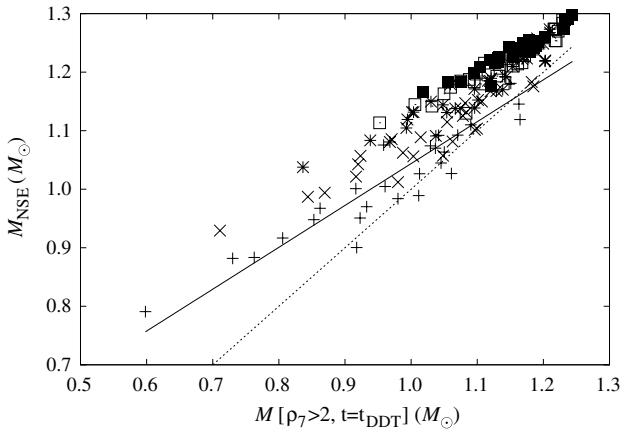

Figure 5. Mass burned to NSE as compared to the mass above a density of 2×10^7 g cm^{-3} at the first DDT time for each realization in our sample. The different shapes plotted (+, ×, ∗, □, ■) correspond to different transition densities ($10^{7.1}$, $10^{7.2}$, $10^{7.3}$, $10^{7.4}$, $10^{7.5}$), respectively. The solid line shows the linear fit to yields produced with a DDT density of $10^{7.1}$ g cm^{-3} most closely matching the DDT density used in Townsley et al. (2009). The dashed line shows a 1:1 correlation between the NSE yield and mass above 2×10^7 g cm^{-3}. The lowest two DDT densities are less than the density threshold 2×10^7 g cm^{-3} and thus show more scatter about the linear relation due to increased dependence on the plume morphology.

As discussed in detail in Townsley et al. (2009), many systematic effects exist that influence the outcome of an SN. In that study, the direct effect of ^{22}Ne was explored and found to have a negligible influence on the NSE yield. Therefore, we do not vary the initial ^{22}Ne mass fraction, but rather study the effect of varying the DDT density with the expectation that the NSE yield will be influenced indirectly by ^{22}Ne and ^{12}C abundances through the DDT density. We focus on the indirect effect of the ^{22}Ne abundance on the NSE yield, following up previous work in Townsley et al. (2009) and neglect the effect of varying the carbon abundance. Additionally, we neglect effects due to the central ignition density, compositional and thermodynamic WD structure, and the total WD mass. The effects due to these variables will be studied in turn in future works with the goal of addressing interdependencies once individual effects are better understood.

5.1. Dependence on Transition Density

The evolution of the amount of material above a density threshold ($M_{\rho>\rho_{\rm thres}} = \int_{\rho_{\rm thres}} \rho dV$, where we take $\rho_{\rm thres} = 2 \times 10^7$ g cm^{-3}) principally determines the dependence of the NSE yield on DDT density. This is due largely to the linear relationship between the NSE yield and $M_{\rho_7>2}(t = t_{\rm DDT})$ shown in Figure 5, where $t_{\rm DDT}$ is defined as the time the flame first reaches the specified DDT density. This definition is consistent with our assumption that DDT conditions are met on the tops of rising plumes. As mentioned above, other DDT locations are possible, such as the highly turbulent region underneath plume

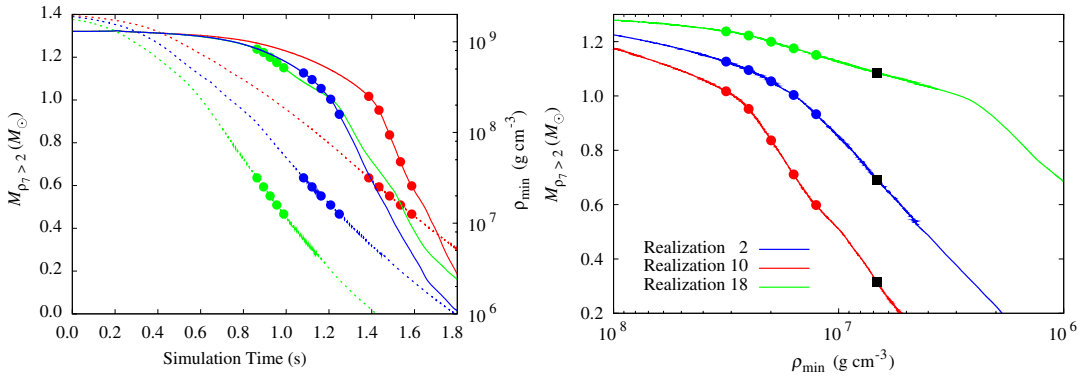

Figure 6. Comparison of the evolution of the white dwarf defined by the mass above the density threshold ($M_{\rho_7>2}$) to the plume evolution defined by the minimum flame density ($\rho_{\rm min}$). The left panel presents the evolution of $M_{\rho_7>2}$ (solid) and $\rho_{\rm min}$ (dotted) as a function of simulation time for realizations 2 (blue), 10 (red), and 18 (green) showing the expansion rate of the WD and the plume rise time with DDT times (circles) associated with each DDT density emphasized. $M_{\rho_7>2}$ is defined as the total mass with density greater than 2×10^7 g cm^{-3} and $\rho_{\rm min}$ is defined as the minimum density at which the flame is burning material. The translation into $M_{\rho_7>2}$ as a function of $\rho_{\rm min}$ is shown in the right panel for comparison to $M_{\rm NSE}$ as a function of $\rho_{\rm DDT}$ shown in Figure 7. We also highlight the fiducial DDT density as black squares. These plots emphasize the importance of the rate of expansion of the WD and the plume rise time as a function of density in determining the relation between the NSE yield and DDT density. Realization 2 produces NSE yields that are close to the average while realizations 10 and 18 produce the lowest and highest yields, respectively.

(A color version of this figure is available in the online journal.)

"caps," which would result in a higher DDT density correlated to our present definition via the density structure local to the rising plume. As shown in Figure 4, the deflagration phase burns only a relatively small fraction of the WD and the majority of material is burned during the detonation. Once a detonation has started, the propagation speed of the burning wave is much greater than the rate of expansion; therefore, the NSE yield is essentially independent of the evolution of $M_{\rho_7>2}$ for $t > t_{\rm DDT}$. The number of detonation points and their corresponding distribution in time and location contributes to the variance of the relation between the NSE yield and $M_{\rho_7>2}$. The relation between the NSE yield and DDT density via $M_{\rho_7>2}$ also depends on the acceleration of the RT-unstable plumes not being too great near $t_{\rm DDT}$. For a constant plume rise rate near $t_{\rm DDT}$, there is a linear relationship between the DDT density and $t_{\rm DDT}$. This relationship allows the evolution of $M_{\rho_7>2}$ to translate directly into a dependence of the NSE yield on DDT density. Figure 6 shows the evolution of $M_{\rho_7>2}$ and $\rho_{\rm min}$ as a function of simulation time for three different realizations where $\rho_{\rm min}$ is the minimum density at which the flame is burning material. The evolution of $\rho_{\rm min}$ shows the linear relationship between the log of the DDT density and $t_{\rm DDT}$ where the filled circles represent the $t_{\rm DDT}$ times for each of the five transition densities and the filled squares show the fiducial DDT density. For the times corresponding to the DDT conditions, the evolution of $M_{\rho_7>2}$ is in a region where the rate of expansion of the star becomes significant and $M_{\rho_7>2}$ begins to drop off relatively quickly.

We find, for each individual realization, the NSE yield depends quadratically on transition density. Table 3 lists the NSE yields for each realization at each of five transition densities equidistant in log space. Table 4 shows the coefficients used to fit the quadratic dependence of NSE yield on transition density for

$$M_{\rm NSE}(M_\odot) = a\,(\mathcal{L}\rho_{\rm DDT})^2 + b\mathcal{L}\rho_{\rm DDT} + c. \qquad (5)$$

Figure 7 shows fits to the NSE yield for each realization and the average yields at each transition density. The NSE yields for individual realizations are plotted as blue crosses and the individual curves showing the dependence of NSE yield on DDT density are shown in gray. The average NSE yields at each DDT density are shown in red. At a transition density of $10^{7.5}$ g cm^{-3}, notice that the dependence on DDT density has flattened out for almost all realizations and the variance of the

Table 3
NSE Yields in $M_\odot$ for each Realization at each Transition Density, $\mathcal{L}\rho_{\rm DDT}$

Rel.	$\mathcal{L}\rho_{\rm DDT}$				
#No.	7.1	7.2	7.3	7.4	7.5
1	0.989	1.082	1.152	1.207	1.236
2	0.970	1.056	1.131	1.184	1.215
3	0.948	1.043	1.119	1.174	1.209
4	0.951	1.062	1.144	1.197	1.226
5	1.027	1.101	1.168	1.214	1.242
6	1.074	1.138	1.185	1.219	1.248
7	1.076	1.132	1.179	1.215	1.243
8	1.110	1.167	1.210	1.239	1.260
9	0.917	1.022	1.105	1.163	1.199
10	0.791	0.929	1.038	1.113	1.166
11	1.092	1.147	1.189	1.229	1.255
12	1.240	1.258	1.273	1.289	1.301
13	0.882	0.987	1.083	1.145	1.183
14	1.070	1.125	1.185	1.223	1.250
15	1.119	1.176	1.218	1.254	1.274
16	0.883	0.994	1.081	1.142	1.183
17	1.026	1.115	1.171	1.213	1.241
18	1.181	1.223	1.249	1.270	1.290
19	0.967	1.057	1.132	1.185	1.220
20	1.005	1.089	1.138	1.180	1.218
21	1.222	1.248	1.268	1.284	1.297
22	1.045	1.104	1.170	1.216	1.244
23	1.001	1.085	1.150	1.187	1.223
24	0.900	1.012	1.091	1.130	1.176
25	0.989	1.057	1.139	1.193	1.226
26	1.092	1.150	1.192	1.228	1.254
27	1.192	1.222	1.251	1.274	1.290
28	1.145	1.183	1.220	1.253	1.273
29	1.063	1.131	1.175	1.210	1.235
30	1.179	1.225	1.249	1.273	1.288
$\bar{M}$	1.038	1.111	1.169	1.210	1.239
σ	0.110	0.082	0.059	0.046	0.036
$\sigma_{\bar{M}}$	0.020	0.015	0.011	0.008	0.007

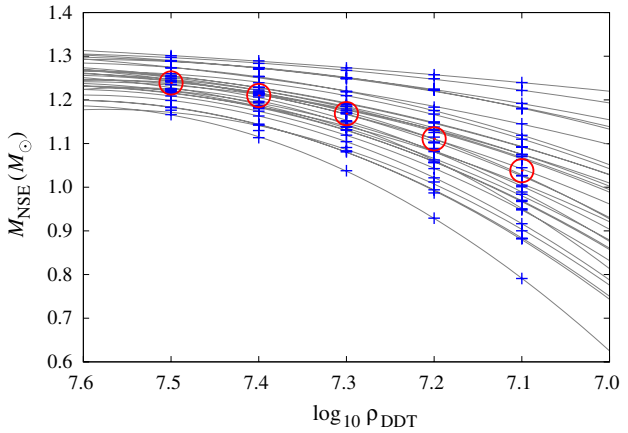

Figure 7. Quadratic fits (gray lines) to the NSE yields for each realization (blue crosses) and the average NSE yield at each transition density (red circles). The qualitative similarity between this figure and the right panel of Figure 6 is due to the near 1:1 correlation between $M_{\rm NSE}$ and $M_{\rho_7>2}(t = t_{\rm DDT})$.

(A color version of this figure is available in the online journal.)

Table 4
Coefficients used to Fit the Quadratic Dependence of Transition Density on NSE Yield Using Equation (5)

No.	$a\,(M_\odot)$	$b\,(M_\odot)$	$c\,(M_\odot)$	$M_{\rm NSE}(\mathcal{L}\rho_{\rm DDT,0})$
1	−1.024	15.56	−57.9	0.637
2	−0.933	14.24	−53.1	0.633
3	−1.010	15.40	−57.5	0.589
4	−1.388	20.95	−77.8	0.515
5	−0.815	12.43	−46.2	0.732
6	−0.595	9.12	−33.7	0.852
7	−0.480	7.42	−27.4	0.876
8	−0.619	9.41	−34.5	0.898
9	−1.164	17.70	−66.1	0.515
10	−1.454	22.17	−83.3	0.279
11	−0.442	6.87	−25.4	0.902
12	−0.083	1.36	−4.3	1.183
13	−1.212	18.45	−69.0	0.456
14	−0.557	8.58	−31.8	0.844
15	−0.575	8.78	−32.2	0.910
16	−1.173	17.88	−66.9	0.470
17	−0.963	14.58	−54.0	0.712
18	−0.348	5.34	−19.2	1.048
19	−0.926	14.15	−52.8	0.628
20	−0.708	10.86	−40.4	0.740
21	−0.210	3.25	−11.3	1.134
22	−0.583	9.03	−33.6	0.798
23	−1.093	16.47	−60.9	0.696
24	−1.219	18.46	−68.7	0.502
25	−0.782	12.04	−45.1	0.671
26	−0.490	7.56	−27.9	0.896
27	−0.248	3.86	−13.7	1.080
28	−0.276	4.36	−15.9	1.006
29	−0.685	10.42	−38.4	0.827
30	−0.429	6.54	−23.6	1.032

Note. The NSE mass in units of $M_\odot$ is evaluated at $\mathcal{L}\rho_{\rm DDT,0}$ using the coefficients.

yields among all realizations is small. This behavior is due to the fact that the progenitor WD star has a finite mass of 1.37 $M_\odot$. At the highest transition density, the expansion rate of the star is relatively small, and the evolution of $M_{\rho_7>2}$ is relatively slowly declining as compared to lower DDT densities (see Figure 6).

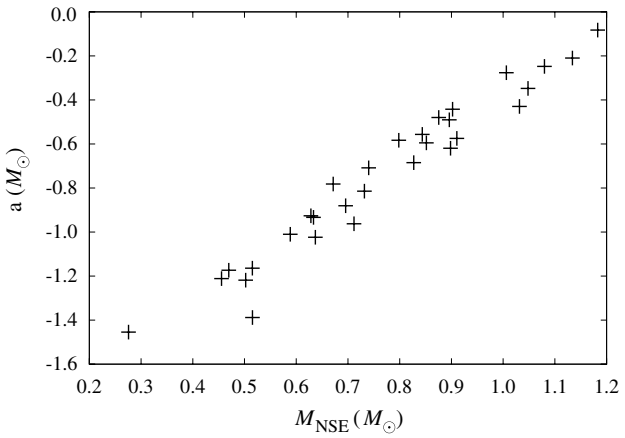

Figure 8. Correlation between the NSE yield at the fiducial DDT density $\mathcal{L}\rho_{\rm DDT,0} = 6.83$ and the fitting parameter a from Equation (5). A lower yield indicates a stronger curvature with DDT density.

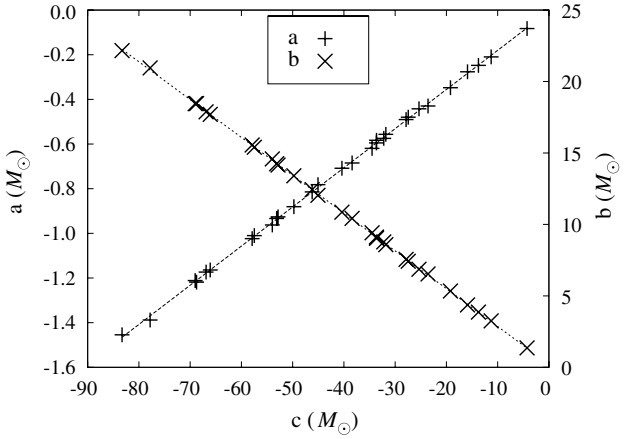

Figure 9. Correlation between the NSE yield fitting parameter, c, with the fitting parameters a (left axis) and b (right axis) from Table 4 for each realization. The fitting parameters are defined by Equation (5) and the relations between the fitting parameters are given by Equations (6) and (7).

The curvature of the NSE yield dependence on DDT density, a, is well correlated with the NSE yield at a given DDT density. Figure 8 shows this correlation for $\mathcal{L}\rho_{\rm DDT,0} = 6.83$; however, a correlation exists for all DDT densities as may be discernible from Figure 7 noting that most black lines representing individual realizations do not cross. The lower the NSE yield for a given realization, the stronger the dependence on transition density. This result is likely due to realizations with lower yields having multiple competing plumes that release more energy allowing the star to expand more rapidly leading to a stronger dependence on the transition density.

After fitting the dependence on DDT density for each realization, we find an interesting correlation between the fitting parameters from Equation (5). Figure 9 shows the correlation between the fitting parameters a, b, and c with c on the horizontal axis. The tight correlation between these parameters indicates that a single parameter describes the dependence on DDT density for a given realization. The fitting parameters a and b can be expressed as a function of c:

$$a = \alpha c + \beta, \tag{6}$$

$$b = \delta c + \gamma, \tag{7}$$

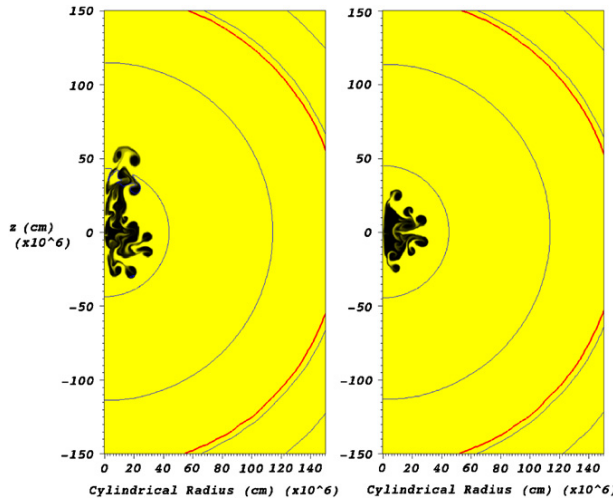

Figure 10. Snapshots of realization 18 (left) and realization 10 (right) at a simulation time of 0.4 s. Realization 18 produced the highest yield and shows the development of a single dominant plume while realization 10 had the lowest yield and shows all plumes developing at about the same rate. Shown in color are fuel and burning products: unburned C, O, Ne (yellow) and Fe-group (NSE, black). Density in g cm^{-3} is indicated by contours (blue) logarithmically spaced at integer powers of 10 as well as the DDT density of 1.26×10^7 g cm^{-3} (red). (A color version of this figure is available in the online journal.)

where $\alpha = (1.754 \pm 0.003) \times 10^{-2}$, $\beta = -0.005 \pm 0.002$, $\delta = -0.2646 \pm 0.0005$, and $\gamma = 0.21 \pm 0.02$. These parameters were calculated using a least-squares method and the associated errors were calculated from the corresponding covariance matrix.

Each realization has a different random initial perturbation of the central ignition condition that sets the plume morphology. Dominant single plumes tend to allow the star to expand less prior to reaching the conditions for a detonation, while multiple competing plumes tend to release more energy during the deflagration phase, allowing more expansion prior to reaching the conditions for a DDT. Shown in Figure 10 are the RT unstable plumes for the realizations with the highest and lowest yields a few tenths of seconds into the deflagration. Unfortunately, no strong correlation exists between the properties of the initial flame surface, such as mass enclosed, surface to volume ratio, or amount of power in the perturbation, for a given realization and the single fitting parameter c. This lack of a correlation implies there is no way to tell whether a particular initial condition will seed a single dominant plume or multiple competing plumes.

Physically, we might expect two competing effects that influence the NSE yield: plume morphology (rise time) and the rate of expansion. In our two-dimensional simulations, these two effects appear to be correlated as seen in Figure 6. Our results indicate that plumes near the symmetry axis tend to rise faster than plumes rising near the equator and we attribute this result to the fact that our simulations are two-dimensional. A plume that develops near the symmetry axis naturally becomes dominant in two dimensions and determines the DDT time and thus the NSE yield. In addition, a plume near the symmetry axis represents less volume than a plume of similar size near the equator. This indicates that energy is being deposited into a smaller volume allowing for a lesser rate of expansion. This explains why the overall rate of expansion of the star is correlated to the rise time of the first plume to reach DDT conditions.

In order to evaluate the dependence on DDT density without this unphysical correlation, we need to perform three-dimensional simulations. A suite of three-dimensional simulations will likely create a two-parameter family (plume rise and expansion rates) of solutions which describe the yield as a function DDT density. Additionally, we expect three-dimensional plumes to behave similarly to two-dimensional on-axis plumes implying a faster plume rise time.

Table 5
Statistical Properties of the Fitting Parameter c and the NSE Yield at $\rho_{\rm DDT} = 6.76 \times 10^6$ g cm^{-3}

Parameter	Mean	Std. Dev.	Std. Dev. of Mean
c ($M_\odot$)	−42	21	4
$M_{\rm NSE,0}$ ($M_\odot$)	0.77	0.22	0.04

As a result of the tight correlation for a and b and the determination of Equations (6) and (7), the average relation is characterized by just the average c—or equivalently, the average NSE yield at a specified $\rho_{\rm DDT}$. We evaluate the average and standard deviation of the fitting parameter c as well as the statistical properties of the NSE yield at the fiducial transition density of $10^{6.83}$ g cm^{-3} shown in Table 5.

5.2. NSE Yield Dependence on ^{22}Ne

Recall that for the purposes of this study, we are neglecting the effects of varying the core carbon abundance, the central ignition density, the WD structure, etc., except for the indirect effect of X_{22}, the neutron excess produced during simmering, and the DDT density. In order to derive the NSE yield dependence on X_{22}, we need to expand the derivative of $M_{\rm NSE}$ with respect to X_{22} which involves only a couple of terms given our assumptions

$$\frac{dM_{\rm NSE}}{dX_{22}} = \frac{\partial M_{\rm NSE}}{\partial \mathcal{L}\rho_{\rm DDT}} \frac{d\mathcal{L}\rho_{\rm DDT}}{dX_{22}} + \frac{\partial M_{\rm NSE}}{\partial X_{22}}. \quad (8)$$

Townsley et al. (2009) showed that $\frac{\partial M_{\rm NSE}}{\partial X_{22}} = 0$. In that study, they employed an estimate of the mass burned to NSE by measuring the amount of mass above a density of 2×10^7 g cm^{-3}. That correlation is confirmed by our current study as shown in Figure 5 where we plot the NSE yield of all realizations at each transition density. The correlation between NSE yield and mass above 2×10^7 g cm^{-3} at $t_{\rm DDT}$ for a transition density of 1.26×10^7 g cm^{-3}, closest to the transition density used for that study, is highlighted. Given our assumptions and the result that the NSE yield does not depend directly on X'_{22} (Townsley et al. 2009), the NSE yield only depends directly on the DDT density. The effect of X'_{22} on the yield enters through the DDT density. Therefore, we will construct the functional dependence of $\mathcal{L}\rho_{\rm DDT}$ on X'_{22}.

The DDT density depends on X_{22} via the microphysics involved in determining the conditions under which the flame transitions from a deflagration to a detonation, which, as noted above, is incompletely understood. We assume the transition occurs at a particular density at which the flame enters the distributed burning regime, but more stringent conditions for the DDT include dependences on the turbulent cascade and the growth of a critical mass of fuel with sufficiently strong turbulence (Pan et al. 2008; Woosley et al. 2009; Schmidt et al. 2010). The dependence on composition of these models may be explored and applied to the trends with DDT density presented in this study. Under our assumptions, the flame enters the distributed burning regime when the laminar flame width

Table 6
Coefficients for log–log Fits to Equation (11)

Parameter	$X_{22} = 0.02$	$X_{22} = 0.06$
a_s	0.7942	0.7745
b_s	−12.735	−12.121
a_δ	−1.3550	−1.3507
b_δ	19.17	18.88

Note. The subscript denotes whether fitting for the laminar flame speed (s) or flame width (δ).

becomes of the order of the Gibson length (l_G), where

$$l_G = L\left(\frac{s_l}{u'}\right)^3. \quad (9)$$

Here, L is the length scale on which the strength of the turbulent velocity (u') is evaluated, and s_l is the laminar flame speed (see, e.g., Peters 2000). By using the laminar flame speeds and widths which depend on X_{22} from Chamulak et al. (2007), we choose the conditions for a detonation are met at $X_{22} = 0.02$ at a particular transition density ($\mathcal{L}\rho_{\rm DDT}$) when the Gibson length is equal to the laminar flame width. The strength of the turbulent velocity field is calculated assuming a Kolmogorov turbulence cascade:

$$u' = s_l(\rho, X_{22} = 0.02)\left(\frac{\delta_l(\rho, X_{22} = 0.02)}{L}\right)^{1/3}. \quad (10)$$

Using u', we solve for the change in transition density, $\Delta\mathcal{L}\rho_{\rm DDT}$, by changing ^{22}Ne to $X_{22} = 0.06$ and again setting the Gibson length equal to the laminar flame width where L cancels out of the equation. This evaluation yields a change in transition density over a change in X_{22}, or $\frac{d\mathcal{L}\rho_{\rm DDT}}{dX_{22}}$.

We use log–log fits to the flame speed and flame width as a function of density using the table generated by Chamulak et al. (2007). We use only densities above 10^8 g cm^{-3} for $X_{12} = 0.3$ and above 5×10^8 for $X_{12} = 0.5$. Within this parameter space, a power-law dependence of the flame speeds and widths on the log of the density is well defined and the algorithm used to solve the flame characteristics is more stable at higher densities. Our resulting expressions for the density dependence on flame speed, s, and flame width, δ_l, at the carbon mass fraction used in this study ($X_{12} = 0.4$) for $X_{22} = 0.02, 0.06$ are given by

$$\ln s = a \ln \rho + b \quad (11)$$

with coefficients given in Table 6.

Our derived expression for the derivative of transition density as a function of X_{22} is given by

$$\begin{aligned}\frac{d\mathcal{L}\rho_{\rm DDT}}{dX_{22}} &= \frac{b_{\delta,6} - b_{\delta,2} + 3\,(b_{s,2} - b_{s,6}) + \ln \rho_{\rm DDT}\,(3a_{s,2} - a_{\delta,2})}{\ln 10\,(3a_{s,6} - a_{\delta,6})\Delta X_{22}} \\ &\quad - \frac{\mathcal{L}\rho_{\rm DDT}}{\Delta X_{22}} \\ &= u\mathcal{L}\rho_{\rm DDT} + v, \end{aligned} \quad (12)$$

where $u = 0.4315$ and $v = -6.301$. We solve this first-order differential equation and express the DDT density as a function of X'_{22}:

$$\mathcal{L}\rho_{\rm DDT}(X'_{22}) = \frac{v}{u}\left(e^{u(X'_{22} - X'_{22,0})} - 1\right) + \mathcal{L}\rho_{\rm DDT,0}e^{u(X'_{22} - X'_{22,0})}, \quad (13)$$

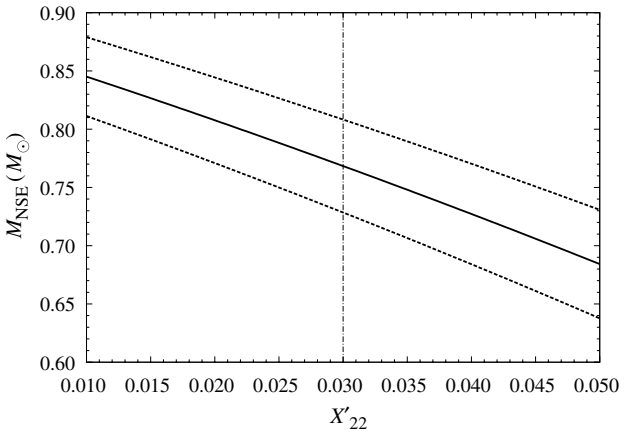

Figure 11. Analytic solution to $M_{\rm NSE}$ as a function of parameterized X'_{22} and using standard error propagation to obtain the uncertainty based on the standard deviation of the mean (dashed lines). The vertical dot-dashed line indicates the parameter space in which this study was performed. These results were evaluated for the fiducial transition density of 6.76×10^6 g cm^{-3} corresponding to $X'_{22} = 0.03$.

where $X'_{22,0}$ is the parameterized ^{22}Ne mass fraction chosen to be associated with the fiducial transition density, $\mathcal{L}\rho_{\rm DDT,0}$. For all the transition densities considered in this study, the interface between the core composition and the composition of the outer layer is at a lower density. Therefore, the relevant ^{22}Ne content to consider is that of the core. Plugging in Equation (13) into Equation (5), we obtain the functional dependence of $M_{\rm NSE}$ on X'_{22}, such that

$$M_{\rm NSE} = M_{\rm NSE}(\mathcal{L}\rho_{\rm DDT}(X'_{22})). \quad (14)$$

Equation (14) is evaluated and plotted in Figure 11 for the fiducial transition density at the ^{22}Ne mass fraction used in this study,

$$\mathcal{L}\rho_{\rm DDT}(X'_{22,0} = 0.03) = \mathcal{L}\rho_{\rm DDT,0} = 6.83. \quad (15)$$

We propagate the standard deviation of the mean evaluated at $\mathcal{L}\rho_{\rm DDT,0}$ for a range of X'_{22}. This is calculated by considering the relation between the standard deviation of the mean of the NSE mass and the standard deviation of the mean of the fitting parameter, c, given by

$$\sigma_{\rm NSE} = (\alpha[\mathcal{L}\rho_{\rm DDT}(X'_{22})]^2 + \delta\mathcal{L}\rho_{\rm DDT}(X'_{22}) + 1)\sigma_c, \quad (16)$$

where $\sigma_{\rm NSE}$ is the standard deviation of the mean of the NSE mass and σ_c is the standard deviation of the mean in the fitting parameter c. We evaluate σ_c by inverting Equation (16) and solving for $X'_{22} = X'_{22,0}$. Plugging in this solution, the standard deviation of the mean of the NSE mass as a function of X'_{22} becomes

$$\sigma_{\rm NSE}(X'_{22}) = \frac{\alpha[\mathcal{L}\rho_{\rm DDT}(X'_{22})]^2 + \delta\mathcal{L}\rho_{\rm DDT}(X'_{22}) + 1}{\alpha[\mathcal{L}\rho_{\rm DDT,0}]^2 + \delta\mathcal{L}\rho_{\rm DDT,0} + 1}\sigma_{\rm NSE,0}. \quad (17)$$

5.3. ^{56}Ni Yield Dependence on Metallicity

Now that we have constructed the functional dependence of NSE yield on ^{22}Ne we need to consider the dependence of the amount of ^{56}Ni synthesized in the explosion on metallicity through the ^{22}Ne content. A fractional amount of the NSE

material is radioactive ^{56}Ni, which powers the SN light curve. This fraction depends on Y_e (and ^{22}Ne) as described in Timmes et al. (2003):

$$M_{56} = f_{56} M_{\rm NSE}. \tag{18}$$

In order to determine the dependence of M_{56} on metallicity through the DDT density, we must construct f_{56} and explore any dependencies on DDT density and metallicity. From our simulations, we calculate $M_{\rm NSE}$ directly and estimate M_{56} from Y_e choosing the non-^{56}Ni NSE material to be 50/50 ^{54}Fe and ^{58}Ni by mass. Recall that X'_{22} from Equation (1) contains a term, ΔX_{22}, which is a parameterization of the change in Y_e due to neutronization during the carbon-simmering phase. However, not all of the neutron excess evaluated at the $M_{\rm NSE}$ plateau time comes from ^{22}Ne or the carbon-simmering products. Some change in Y_e is due to weak reactions occurring during the explosion that are included in our burning model (Calder et al. 2007; Townsley et al. 2007).

First, we consider the amount of non-^{56}Ni NSE material determined by X'_{22} by equating the initial Y_e to the Y_e of material in NSE. Using baryon and lepton conservation for NSE material, we describe the electron fraction by contributions from ^{54}Fe, ^{58}Ni, and ^{56}Ni

$$Y_e = \frac{26}{54}\left(\frac{1}{2} f_{\rm non-56}\right) + \frac{28}{58}\left(\frac{1}{2} f_{\rm non-56}\right) + \frac{28}{56}(1 - f_{\rm non-56}), \tag{19}$$

where $f_{\rm non-56}$ is the mass fraction of non-^{56}Ni NSE material. For the following evaluation, we approximate the composition to be that of the core because most of the NSE material is within the core. We write the initial Y_e as

$$Y_{e,i} = \frac{10}{22} X'_{22} + \frac{1}{2}(1 - X'_{22}). \tag{20}$$

We can then solve for $f_{\rm non-56}$ by equating Equations (19) and (20) and add a term X_n to represent the additional contribution due to neutronization from weak reactions occurring during the explosion

$$f_{\rm non-56} = \frac{783}{308} X'_{22} + X_n. \tag{21}$$

Then, the ^{56}Ni fraction of material in NSE is

$$f_{56} = 1 - \frac{783}{308} X'_{22} - X_n. \tag{22}$$

We note that the rate of weak reactions occurring during the explosion may depend on the initial composition as well. Accordingly, X_n may have a dependence on X'_{22}. We also expect X_n to vary as a function of the transition density because a higher transition density will have less time for weak reactions to occur.

We construct a statistical sample of f_{56} using the ratio of the ^{56}Ni and NSE yields produced in the simulations. We calculate the dependence of X_n on transition density using a least-squares method and the result is shown in Figure 12. Evaluating the partial derivative of X_n at the fiducial transition density, we find a shallow dependence:

$$\left.\frac{\partial X_n}{\partial \mathcal{L}\rho_{\rm DDT}}\right|_{\mathcal{L}\rho_{\rm DDT} = \mathcal{L}\rho_{\rm DDT,0}} = -0.096. \tag{23}$$

We want to know the dependence of M_{56} on X_{22}. Since f_{56} depends on the neutronization from weak reactions during the explosion, we must consider any dependencies of this neutronization on DDT density or X'_{22}. We show that the dependence of f_{56} on X'_{22} via the effect of X'_{22} on the in situ neutronization is much weaker than the direct dependence due to lepton number conservation. Similar to Equation (18), we write

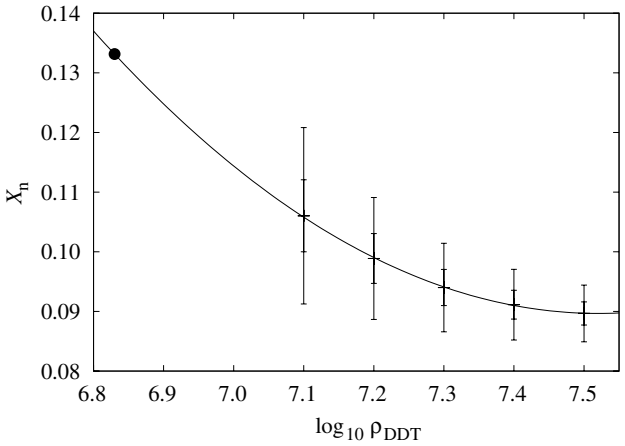

Figure 12. Fraction of non-^{56}Ni NSE material due to weak processes (X_n) is calculated from inverting Equation (22) and using the $f_{56} = M_{56}/M_{\rm NSE}$ averaged over all realizations at each DDT density. The standard deviation of the sample (outer) and mean (inner) are shown as error bars at each DDT density. A quadratic best-fit line is calculated using the standard deviation of the sample. The fiducial DDT density is shown as a black circle where $X_n = 0.133$.

$$\frac{dM_{56}}{dX_{22}} = \frac{\partial M_{56}}{\partial M_{\rm NSE}} \frac{dM_{\rm NSE}}{dX_{22}} + \frac{\partial M_{56}}{\partial X_{22}}. \tag{24}$$

Using Equation (18) and expanding the partial derivative of M_{56} on X_{22}, we obtain

$$\frac{dM_{56}}{dX_{22}} = f_{56} \frac{dM_{\rm NSE}}{dX_{22}} + M_{\rm NSE} \frac{df_{56}}{dX_{22}}. \tag{25}$$

Taking the derivative of Equation (22) and expanding on X_{22}, we obtain

$$\frac{df_{56}}{dX_{22}} = \frac{\partial f_{56}}{\partial X_{22}} - \frac{dX_n}{dX_{22}}. \tag{26}$$

Now we wish to evaluate whether $\frac{dX_n}{dX_{22}}$ is an important contribution to the overall evaluation of the ^{56}Ni mass. Expanding this term yields

$$\frac{dX_n}{dX_{22}} = \frac{\partial X_n}{\partial \mathcal{L}\rho_{\rm DDT}} \frac{d\mathcal{L}\rho_{\rm DDT}}{dX_{22}} + \frac{\partial X_n}{\partial X_{22}}. \tag{27}$$

Referring to Townsley et al. (2009), we can estimate $\frac{\partial X_n}{\partial X_{22}}$ by calculating the average ratio of M_{56} to $M_{\rm NSE}$ at $X_{22} = 0, 0.02$ for the first five realizations whose detonation phases were simulated. The result is $\frac{\partial X_n}{\partial X_{22}} \sim -0.2$. The first term in Equation (27) can be evaluated from multiplying Equation (23) and Equation (12) for $\mathcal{L}\rho_{\rm DDT}$ in the range 7.0–7.5. For the fiducial transition density ($\mathcal{L}\rho_{\rm DDT,0}$), we find

$$\frac{dX_n}{dX_{22}} = (-0.126)(-3.35) - 0.2 \sim 0.2. \tag{28}$$

Comparing to $\frac{\partial f_{56}}{\partial X_{22}} \simeq -2.5$, we find that the magnitude of $\frac{dX_n}{dX_{22}}$ is much smaller and is unimportant for our evaluation of the dependence of the ^{56}Ni yield on X_{22}. Therefore, we can ignore

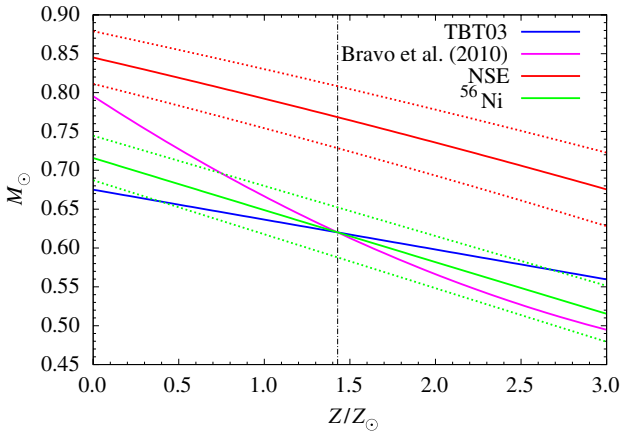

Figure 13. Solution of $M_{\rm NSE}$ (red) and M_{56} (green) computed as a function of metallicity as compared to the ^{56}Ni relations from Timmes et al. (2003; blue) and Bravo et al. (2010; magenta) normalized to the average ^{56}Ni yield from our simulations. The dashed lines show the propagated standard deviation of the mean. The vertical dot-dashed line indicates the parameter space in which this study was performed. These results were evaluated with a fiducial transition density of 6.76×10^6 g cm^{-3} at $Z = 1.4\,Z_\odot$.

(A color version of this figure is available in the online journal.)

this term in the expansion of $\frac{df_{56}}{dX_{22}}$ in Equation (26) and let $\frac{dX_n}{dX_{22}} \sim 0$. The full derivative of f_{56} with respect to X_{22} can now be written as a partial derivative such that

$$\frac{dM_{56}}{dX_{22}} = f_{56}\frac{dM_{\rm NSE}}{dX_{22}} + M_{\rm NSE}\frac{\partial f_{56}}{\partial X_{22}}. \quad (29)$$

While we approximate X_n as constant, we choose to evaluate it at $\mathcal{L}\rho_{\rm DDT,0}$ using the best-fit curve from Figure 12 obtaining $X_n = 0.133$. Now we can relate the metallicity to ^{22}Ne since X_{22} traces metallicity (Timmes et al. 2003). Substituting $X_{22} = 0.014(Z/Z_\odot)$ in Equation (1), we obtain

$$X'_{22} = 0.014\left(\frac{Z}{Z_\odot}\right) + \Delta X_{22}(\Delta Y_e), \quad (30)$$

where $\Delta X_{22} = 0.01$ for this study and X'_{22} is our parameterization of the actual ^{22}Ne mass fraction, X_{22}. The ^{56}Ni yield as a function of X'_{22} is calculated by multiplying Equation (22) by Equation (14) and using $X_n = 0.133$. The ^{56}Ni yield is plotted in Figure 13 using Equation (30) to relate X'_{22} to $Z/Z_\odot$.

6. CONCLUSIONS AND FUTURE WORK

We have analyzed the influence of the DDT density on the total ^{56}Ni synthesized during thermonuclear SNe. We determined that the dependence on DDT density is quadratic in nature, but this dependence can be described by a single parameter. We estimated the dependence of the SN brightness (^{56}Ni yield) on metallicity by assuming a DDT occurs when the flame enters the distributed burning regime and extrapolating the laminar flame speeds and widths down to low densities. We find

$$\left.\frac{dM_{56}}{d(Z/Z_\odot)}\right|_{Z=Z_\odot} = -0.067 \pm 0.004\,M_\odot, \quad (31)$$

which is slightly steeper than Timmes et al. (2003) as seen in Figure 13. The uncertainty was calculated using the standard deviation of the mean of the fitting parameter c—or equivalently, the standard deviation of the mean of the NSE yield at a particular DDT density. The uncertainty in the assumptions about the normalization of the transition density as a function of X'_{22} was not considered for the purpose of evaluating the uncertainty in the derivative. We find the effect of metallicity on DDT density influences the production of NSE material; however, the ratio of the ^{56}Ni yield to the overall NSE yield does not change as significantly and remains similar to the relation estimated from approximate lepton number conservation. We also find that the scatter in SN brightness increases with decreasing transition density.

The very recent work of Bravo et al. (2010) on metallicity as a source of dispersion in the luminosity–width relationship of bolometric light curves addresses many of the same issues as our study and warrants discussion. In particular, Bravo et al. (2010) derive a metallicity dependence on the DDT density similarly to our study. However, the DDT density in their one-dimensional simulations is very different from the DDT density in ours. The principal difference between the work described in this manuscript and that of Bravo et al. (2010) follows from the use of multidimensional simulations. While three-dimensional simulations are required to correctly capture the effects of fluid dynamics and the RT instability, two-dimensional simulations incorporate these effects and relax the assumption of symmetry. Breaking the symmetry and assuming that a DDT initiates as a rising plume approaches $\rho_{\rm DDT}$ produce an expansion history very different from what would be observed in one-dimensional simulations. In fact, using one-dimensional simulations implies that $\rho_{\rm DDT}$ plays an unphysical role. The real physical description of the DDT in an SN Ia will depend on flame–turbulence interactions that will themselves depend on multidimensional effects in the flow. One-dimensional models may be able to capture these effects, but such models must be motivated by more physical multidimensional studies.

In addition, our statistical framework with realizations from randomized initial conditions allows calculation of the scatter inherent in the multidimensional models. The standard deviations calculated for our models averaged over a set of realizations demonstrate that there can be considerable variation following from the randomized initial conditions. These variations follow from the different amounts of expansion occurring during the deflagration phase that follow from the different rising plume morphologies. In one-dimensional models, even with the progenitor metallicity determining $\rho_{\rm DDT}$, there is a one-to-one correspondence between expansion and $\rho_{\rm DDT}$ for a given progenitor.

Bravo et al. (2010) explored two scenarios, a linear and a nonlinear dependence of the ^{56}Ni yield on Z, and report excellent agreement between the nonlinear scenario and observations reported by Gallagher et al. (2008) with the caveat that they used one-dimensional models to arrive at their conclusion. Without comparing results involving the metallicity dependence on $\rho_{\rm DDT}$, Bravo et al. (2010) find a stronger dependence of the ^{56}Ni synthesized from incomplete Si burning on Z than ^{56}Ni coming from NSE material. We find a shallower dependence of the ^{56}Ni yield on Z than Bravo et al. (2010) in part due to our assumption that ^{56}Ni is synthesized as a fraction of NSE material; however, comparing their stratified models to the Timmes et al. (2003) relation results in only a $\sim$20% difference in the dependence of ^{56}Ni yield on Z. This effect is compounded in their "nonlinear" scenario, but again, we must emphasize that $\rho_{\rm DDT}$ plays a completely unphysical role in their simulations and the degree to which this effect is actually enhanced is unknown.

The light curve width calculations and subsequent population synthesis performed by Bravo et al. (2010) after finding a dependence of the ^{56}Ni yield on metallicity are useful in estimating a metallicity dependence in the Hubble residual. For this purpose, we compare the results of the nonlinear scenario of Bravo et al. (2010) to our study along with the expected dependence due to lepton number conservation (Timmes et al. 2003) in Figure 13. Bravo et al. (2010) find an ∼30% steeper dependence of the ^{56}Ni yield on $Z/Z_{\odot}$ evaluated at $Z = 1Z_{\odot}$ than our result in Equation (31). In addition, they find that for high Z the ^{56}Ni yield tends to flatten out becoming more similar to our results. For a particular subrange of metallicites, our results are very similar indicating that by performing the same analysis as Bravo et al. (2010) our results should also agree with the metallicity dependence found by Gallagher et al. (2008).

This similarity depends on the choice of mean ^{56}Ni yield as both Timmes et al. (2003) and Bravo et al. (2010) relations are proportional to this quantity. This implies that the steepness of the relations is affected by the choice of mean ^{56}Ni yield. Our results are not sensitive to this choice. Choosing a higher fiducial DDT density of 10^7 g cm^{-3} that results in a higher mean ^{56}Ni yield of 0.77 $M_{\odot}$ increases Equation (31) by only 0.005 $M_{\odot}$. We see less dependence on the mean ^{56}Ni yield because, although we have a similar dependence on X_{22} due to lepton number conservation, the dependence of the yield on $\mathcal{L}\rho_{\rm DDT}$ is stronger at lower fiducial $\mathcal{L}\rho_{\rm DDT,0}$, as shown in previous sections. This effect is not captured in a simple proportionality relation like that quoted by Bravo et al. (2010), even if this effect is present in their calculations.

It has been discussed whether the source of scatter in peak brightness itself can be attributed to metallicity (Timmes et al. 2003; Howell et al. 2009; Bravo et al. 2010). We submit that multidimensional effects following from fluid instabilities during the deflagration phase leading to varying amounts of expansion provide scatter consistent with observations. The influence of metallicity on the DDT density affects the duration of the deflagration which will secondarily influence the magnitude of the scatter. Our results show that the primary parameter is the degree of (pre-)expansion before DDT—which determines the amount of mass at high density. This is, in turn, controlled by both the expansion rate and the plume rise time. These are also expected to be the basic ingredients in reality.

While our study is consistent with the expected theoretical brightness trend with metallicity (Timmes et al. 2003), observations to date have not been able to confirm this prediction (Gallagher et al. 2005, 2008; Howell et al. 2009). The progenitor age is difficult to decouple from metallicity given the mass–metallicity relationship within galaxy types (Gallagher et al. 2008). Additionally, the dependence of mean brightness of SNe Ia on the age of the parent stellar population appears to be much stronger than any dependence on metallicity (Gallagher et al. 2008; Howell et al. 2009). Seemingly, the only way to observe a dependence on metallicity is to constrain the mean stellar age by selecting galaxies of the same type. This approach was used by Gallagher et al. (2008), but the difficulties in accurately measuring metallicities for the parent stellar population have only constrained the magnitude of the effect on mean brightness, but thus far have not proved that a metallicity effect exists.

In order to determine the dependence of SN brightness (^{56}Ni yield) on metallicity, a better understanding of how the transition density is affected by changes in the ^{22}Ne content is needed. Currently, we have extrapolated data from Chamulak et al. (2007) down to the range of expected transition densities using flame data from densities above 10^8 g cm^{-3}. The trend observed by Chamulak et al. (2007) that increasing X_{22} increases the laminar flame speed is valid for densities above 10^8 g cm^{-3}; however, it is unclear if this trend will hold for densities below 10^7 g cm^{-3}. Direct numerical simulations of the flame are needed for these lower densities to determine whether this trend still holds. However, in this parameter space, the laminar flame is extremely slow requiring a low-Mach-number treatment to model the flow. Regardless of the choice of model for the mechanism that produces a spontaneous detonation, a necessary condition is thought to be distributed burning. Properties of the laminar flame are necessary to estimate when burning becomes distributed. Future studies exploring other DDT mechanisms must also determine their compositional dependencies. So far, we have only explored the effect of varying the ^{22}Ne content directly (Townsley et al. 2009) and indirectly through the DDT density. Other effects exist that we have yet to study such as the carbon composition and flame ignition density (set by the average progenitor age). These properties may be influenced by metallicity such that the net effect on mean brightness is negligible. Additionally, if our assumptions about the dependence of DDT density on metallicity are incorrect and further studies indicate the opposite trend, the metallicity effect on DDT density could negate the effect due to lepton number conservation.

This study stresses the importance of multidimensional effects, but has provided evidence of the limitations of two-dimensional simulations of SNe. In the immediate future, we plan to perform three-dimensional simulations for better realism. In reality, we might expect a two-parameter family in which the morphology of the dominant RT plume is independent of the rate of expansion; however, for our two-dimensional simulations, these two effects appear to be correlated by the choice of cylindrical geometry. A plume developing along the symmetry axis is like three-dimensional RT compared to one near the equator, which is more like two-dimensional RT, and the latter is weaker (slower to develop). In addition to developing faster, plumes near the symmetry axis represent less volume and, therefore, expand the star less. A fast rising plume combined with a slow rate of expansion indicates there will be a shallow dependence on DDT density (since the plume will move through the various DDT densities faster and with less expansion). This result may also depend on our choice that DDT conditions are met at the tops of rising plumes. For these reasons, three-dimensional studies are necessary to ascertain whether there is a physically motivated correlation between the dominant plume morphology and the rate of expansion and whether this correlation depends on the choice of location of the DDT. In transitioning to three-dimensional simulations, we expect the growth of many more plumes; however, the rate of expansion will likely not exceed that found in two dimensions. Because RT develops faster in three dimensions, the conditions for DDT will be met sooner leading to less overall expansion of the star and more mass at high density at the first DDT time. Therefore, we expect three-dimensional results similar to the higher yielding two-dimensional realizations with a shallower dependence on DDT density. In any case, this study indicates that it is possible to determine the susceptibility of a particular model to a change of DDT density (and, hence, a change in the composition which alters the microphysics that set the DDT density). Once the plume morphology has been established several tenths of seconds into

the simulated explosion, it should be possible to estimate the total ^{56}Ni yield to fairly high accuracy given DDT conditions. However, the treatment of turbulent flame properties may be important.

This work was supported by the Department of Energy through grants DE-FG02-07ER41516, DE-FG02-08ER41570, and DE-FG02-08ER41565, and by NASA through grant NNX09AD19G. A.C.C. also acknowledges support from the Department of Energy under grant DE-FG02-87ER40317. D.M.T. received support from the Bart J. Bok fellowship at the University of Arizona for part of this work. The authors acknowledge the hospitality of the Kavli Institute for Theoretical Physics, which is supported by the NSF under grant PHY05-51164, during the programs "Accretion and Explosion: the Astrophysics of Degenerate Stars" and "Stellar Death and Supernovae." The software used in this work was in part developed by the DOE-supported ASC/Alliances Center for Astrophysical Thermonuclear Flashes at the University of Chicago. We thank Nathan Hearn for making his QuickFlash analysis tools publicly available at http://quickflash.sourceforge.net. We also thank the anonymous referee for a careful reading of the manuscript and constructive comments that improved this work. This work was supported in part by the US Department of Energy, Office of Nuclear Physics, under contract DE-AC02-06CH11357 and utilized resources at the New York Center for Computational Sciences at Stony Brook University/Brookhaven National Laboratory which is supported by the U.S. Department of Energy under Contract No. DE-AC02-98CH10886 and by the State of New York.

REFERENCES

Albrecht, A., et al. 2006, arXiv:astro-ph/0609591
Arnett, W. D. 1982, ApJ, 253, 785
Aspden, A. J., Bell, J. B., Day, M. S., Woosley, S. E., & Zingale, M. 2008, ApJ, 689, 1173
Aspden, A. J., Bell, J. B., & Woosley, S. E. 2010, ApJ, 710, 1654
Bravo, E., Domínguez, I., Badenes, C., Piersanti, L., & Straniero, O. 2010, ApJ, 711, L66
Calder, A. C., Plewa, T., Vladimirova, N., Brown, E. F., Lamb, D. Q., Robinson, K., & Truran, J. W. 2003, BAAS, 35, 1278
Calder, A. C., Plewa, T., Vladimirova, N., Lamb, D. Q., & Truran, J. W. 2004, arXiv:astro-ph/0405162
Calder, A. C., et al. 2002, ApJS, 143, 201
Calder, A. C., et al. 2007, ApJ, 656, 313
Chamulak, D. A., Brown, E. F., & Timmes, F. X. 2007, ApJ, 655, L93
Chamulak, D. A., Brown, E. F., Timmes, F. X., & Dupczak, K. 2008, ApJ, 677, 160
Fickett, W., & Davis, W. C. 1979, Detonation (Berkeley, CA: Univ. California Press)
Filippenko, A. V. 1997, ARA&A, 35, 309
Fryxell, B., et al. 2000, ApJS, 131, 273
Gallagher, J. S., Garnavich, P. M., Berlind, P., Challis, P., Jha, S., & Kirshner, R. P. 2005, ApJ, 634, 210
Gallagher, J. S., Garnavich, P. M., Caldwell, N., Kirshner, R. P., Jha, S. W., Li, W., Ganeshalingam, M., & Filippenko, A. V. 2008, ApJ, 685, 752
Gamezo, V. N., Khokhlov, A. M., & Oran, E. S. 2004, Phys. Rev. Lett., 92, 211102
Hicken, M., Wood-Vasey, W. M., Blondin, S., Challis, P., Jha, S., Kelly, P. L., Rest, A., & Kirshner, R. P. 2009, ApJ, 700, 1097
Hillebrandt, W., & Niemeyer, J. C. 2000, ARA&A, 38, 191
Höflich, P., & Khokhlov, A. 1996, ApJ, 457, 500
Howell, D. A., et al. 2009, ApJ, 691, 661
Jordan, G. C., IV, Fisher, R. T., Townsley, D. M., Calder, A. C., Graziani, C., Asida, S., Lamb, D. Q., & Truran, J. W. 2008, ApJ, 681, 1448
Kasen, D., & Plewa, T. 2005, ApJ, 622, L41
Kasen, D., & Woosley, S. E. 2007, ApJ, 656, 661
Khokhlov, A. M. 1989, MNRAS, 239, 785
Khokhlov, A. M. 1991, A&A, 245, 114
Khokhlov, A. M. 1995, ApJ, 449, 695
Khokhlov, A. M., Oran, E. S., & Wheeler, J. C. 1997, ApJ, 478, 678
Kirshner, R. P. 2009, in Dark Energy—Observational and Theoretical Approaches, ed. P. Ruiz-Lapuente (Cambridge: Cambridge Univ. Press), in press (arXiv:0910.0257)
Kolb, E., et al. 2006, Report of the Dark Energy Task Force, available online at http://www.science.doe.gov/hep/files/pdfs/DETF-FinalRptJune30,2006.pdf
Krueger, B. K., Jackson, A. P., Townsley, D. M., Calder, A. C., Brown, E. F., & Timmes, F. X. 2010, ApJ, 719, L5
Lampeitl, H., et al. 2010, MNRAS, 401, 2331
Livio, M. 2000, in Type Ia Supernovae, Theory and Cosmology, ed. J. C. Niemeyer & J. W. Truran (Cambridge: Cambridge Univ. Press), 33
Livne, E., Asida, S. M., & Höflich, P. 2005, ApJ, 632, 443
Mazzali, P. A., Röpke, F. K., Benetti, S., & Hillebrandt, W. 2007, Science, 315, 825
Meakin, C. A., Seitenzahl, I., Townsley, D., Jordan, G. C., Truran, J., & Lamb, D. 2009, ApJ, 693, 1188
Neill, J. D., et al. 2009, ApJ, 707, 1449
Niemeyer, J. C., Hillebrandt, W., & Woosley, S. E. 1996, ApJ, 471, 903
Niemeyer, J. C., & Kerstein, A. R. 1997, New Astron., 2, 239
Niemeyer, J. C., & Woosley, S. E. 1997, ApJ, 475, 740
Pan, L., Wheeler, J. C., & Scalo, J. 2008, ApJ, 681, 470
Perlmutter, S., et al. 1999, ApJ, 517, 565
Peters, N. 2000, Turbulent Combustion (Cambridge: Cambridge Univ. Press)
Phillips, M. M. 1993, ApJ, 413, L105
Pinto, P. A., & Eastman, R. G. 2000, ApJ, 530, 744
Piro, A. L., & Bildsten, L. 2008, ApJ, 673, 1009
Piro, A. L., & Chang, P. 2008, ApJ, 678, 1158
Plewa, T. 2007, ApJ, 657, 942
Plewa, T., Calder, A. C., & Lamb, D. Q. 2004, ApJ, 612, L37
Poludnenko, A., & Oran, E. 2010, Combust. Flame, 157, 995
Riess, A. G., Press, W. H., & Kirshner, R. P. 1996, ApJ, 473, 88
Riess, A. G., et al. 1998, AJ, 116, 1009
Röpke, F. K. 2006, in Reviews in Modern Astronomy, Vol. 19, ed. S. Roeser (Wenheim: Wiley-VCH Verlag), 127
Röpke, F. K., Gieseler, M., Reinecke, M., Travaglio, C., & Hillebrandt, W. 2006, A&A, 453, 203
Röpke, F. K., Woosley, S. E., & Hillebrandt, W. 2007, ApJ, 660, 1344
Schmidt, W., Ciaraldi-Schoolmann, F., Niemeyer, J. C., Röpke, F. K., & Hillebrandt, W. 2010, ApJ, 710, 1683
Seitenzahl, I. R., Meakin, C. A., Townsley, D. M., Lamb, D. Q., & Truran, J. W. 2009a, ApJ, 696, 515
Seitenzahl, I. R., Townsley, D. M., Peng, F., & Truran, J. W. 2009b, At. Data Nucl. Data Tables, 95, 96
Straniero, O., Domínguez, I., Imbriani, G., & Piersanti, L. 2003, ApJ, 583, 878
Timmes, F. X., Brown, E. F., & Truran, J. W. 2003, ApJ, 590, L83
Townsley, D. M., Calder, A. C., Asida, S. M., Seitenzahl, I. R., Peng, F., Vladimirova, N., Lamb, D. Q., & Truran, J. W. 2007, ApJ, 668, 1118
Townsley, D. M., Jackson, A. P., Calder, A. C., Chamulak, D. A., Brown, E. F., & Timmes, F. X. 2009, ApJ, 701, 1582
Vladimirova, N., Weirs, G., & Ryzhik, L. 2006, Combust. Theory Model., 10, 727
Woosley, S. E., Kerstein, A. R., Sankaran, V., Aspden, A. J., & Röpke, F. K. 2009, ApJ, 704, 255
Woosley, S. E., Wunsch, S., & Kuhlen, M. 2004, ApJ, 607, 921

Chapter 4

Turbulence–Flame Interaction Model for Astrophysical Flames

The need to realistically address the early flame evolution in the presence of a strong convection field motivated the development of a turbulence–flame interaction (TFI) model to account for under-resolved TFI [69]. Previous two-dimensional (2D) simulations have provided incredible insight into the explosion mechanism and possible systematic effects [94, 99, 164]; however, the ignition conditions that serve as the basis of these investigations have not previously been explored. 3D simulations are required to explore the evolution of the early flame, as turbulence is only captured correctly in 3D. Previous treatment of turbulent combustion has mainly tried to account for the RT instability [118, 165], and direct interaction with local turbulence has been considered only recently [166, 167].

Schmidt et al. [166, 167] developed a TFI sub-grid scale (SGS) model, but some features of their method are troubling. SGS turbulence energy is, in part, determined by the diffusion-gradient mechanism, which they have shown does not accurately calculate the direction of turbulence diffusion. The worry is that a considerable amount of turbulent energy is generated behind the flame, which may then "diffuse" into the flame-front, and the direction of propagation of the turbulent flame may be determined by the erroneous gradient-diffusion method, rather than the direction normal to the flame brush.

In the following work, I pull from several models used in terrestrial turbulent combustion modeling [168, 169], and apply them to the astrophysical regime. The result of this work is a TFI model provides a local, instantaneous measure of the SGS turbulent intensity, which is used to estimate the wrinkling of flame surface on unresolved scales that serves to increase the burning rate. The flame model used for this work described in was developed by myself, Dean Townsley, and Alan Calder [99, 116, 117, 164]. I lead the investigation of this work and made all decisions related to the implementation of the TFI model. I performed all simulations and analyzed all results.

This work has been submitted to *The Astrophysical Journal* for publication.

TURBULENCE–FLAME INTERACTION MODEL FOR ASTROPHYSICAL FLAMES

AARON P. JACKSON[1], DEAN M. TOWNSLEY[2], ALAN C. CALDER[1,3]

Submitted to the Astrophysical Journal June 8, 2011

ABSTRACT

We extend a model for turbulence–flame interactions (TFI) to consider astrophysical flames with a particular focus on combustion in type Ia supernovae. The inertial range of the turbulent cascade is often under-resolved in simulations of astrophysical flows requiring the use of a model to account for physical processes occurring on sub-grid scales. We provide implementation details to extend a well-tested TFI model to low-Prandtl number flames for use in the compressible hydrodynamics code FLASH. A local, instantaneous measure of the turbulent velocity is calibrated for FLASH and verification tests are provided. Particular care is taken to consider the relation between the sub-grid rms turbulent velocity and the turbulent flame speed, especially for high-intensity turbulence where the turbulent flame speed is not expected to scale with the turbulent velocity.

Subject headings: hydrodynamics—nuclear reactions, nucleosynthesis, abundances—supernovae: general—white dwarfs

1. INTRODUCTION

Type Ia supernovae (SNe) are bright stellar explosions that are characterized by strong P Cygni features in Si and by a lack of hydrogen in their spectra. It is generally accepted that these events follow from the thermonuclear incineration of a degenerate stellar core known as a white dwarf (WD) that produces ~ 0.6 M$_\odot$ of radioactive ^{56}Ni, the decay of which powers the light curve (see Filippenko 1997; Hillebrandt & Niemeyer 2000; Röpke 2006, and references therein for an overview). The light curves of SNe Ia have the property that the brightness of an event is correlated with its duration. This "brighter is broader" relation (Phillips 1993) is the basis for light curve calibration that allows use of these events as distance indicators for cosmological studies (see Conley et al. 2011 for a contemporary example).

While there is agreement on the general properties of thermonuclear SN, the progenitors of these events are not definitively known and their determination is the subject of active research. The possible progenitor systems are generally divided into two categories: single-degenerate (SD; Whelan & Iben 1973; Nomoto 1982b; Iben & Tutukov 1984) and double-degenerate (DD; Iben & Tutukov 1984; Webbink 1984) (*i. e.*, a binary system composed of either one WD or two). In the SD scenario, a ^{12}C-^{16}O WD accretes material from a main sequence or red giant companion. Either the WD accretes material from its companion until it approaches the Chandrasekhar mass ($M_{\rm ch}$) sufficiently heating the core to fuse C and begin the thermonuclear runaway (Woosley et al. 2007a) or a layer of He detonates on the surface of a sub-$M_{\rm ch}$ WD driving a compression wave into the core sufficiently strong to trigger a second detonation ("double-detonation"; Livne 1990). In the DD scenario, two WD's merge via gravitational radiation within a Hubble time. The less massive WD will be tidally disrupted and accreted onto the primary. As long as the accretion rate is not too high to ignite C at the edge (Saio & Nomoto 1985, 1998, 2004), it is possible for the primary to gain enough mass to approach $M_{\rm ch}$ and explode as a SN Ia via the same explosion mechanism as the $M_{\rm ch}$-WD in the SD channel (Yoon et al. 2007). Additionally, Pakmor et al. (2010, 2011) recently showed that under certain conditions, the merger is violent enough such that C ignition at the edge launches a detonation into the primary WD leading to a sub-luminous, super-$M_{\rm ch}$ SNe Ia.

Chandrasekhar-mass progenitor models have been widely accepted as the "standard" progenitor of SNe Ia, although the debate between the SD vs. DD channel is still very active. One-dimensional delayed detonation models have successfully reproduced many observed features that agree with "normal" SNe Ia (Höflich & Khokhlov 1996). Detonation-only models have been ruled out due to the over-production of ^{56}Ni (Nomoto 1982a; Nomoto et al. 1984) and deflagration-only models cannot account for brighter SNe Ia (Röpke et al. 2007). A delayed detonation mechanism best agrees with many observations of multi-band light curve shapes, nucleosynthetic yields, spectral evolution, and SN remnants (Höflich & Khokhlov 1996; Badenes et al. 2003; Kasen 2006; Kasen & Woosley 2007; Woosley et al. 2007b). This mechanism implies a phase of subsonic burning in which the star may respond to thermonuclear burning and expand before a detonation, or supersonic reaction wave, is somehow initiated to burn any remaining fuel on timescales much shorter than the dynamical timescale of the explosion. The standard delayed-detonation model is the so-called deflagration-to-detonation transition (DDT) scenario (Khokhlov 1991); however, the gravitationally-confined detonation (Plewa et al. 2004) and pulsating reverse detonation (Bravo & García-Senz 2006) scenarios have also been explored.

Thermonuclear flames for compositions, densities, and temperatures characteristic of the C-O WD near conditions for explosive C-burning are spatially thin owing to the extreme temperature dependence of the driving reaction, ^{12}C + ^{12}C (Timmes & Woosley 1992). A common computational challenge in modeling astrophysical explosions is that typically the physics of combustion is characterized on length scales well below that accessible in simulations that resolve the macroscopic explosive event. In the context of SNe Ia, combustion initially proceeds subsonically driven by the nuclear fusion of carbon. The flame width of a laminar carbon

[1] Department of Physics & Astronomy, The State University of New York - Stony Brook, Stony Brook, NY

[2] Department of Physics & Astronomy, The University of Alabama, Tuscaloosa, AL

[3] New York Center for Computational Sciences, The State University of New York - Stony Brook, Stony Brook, NY

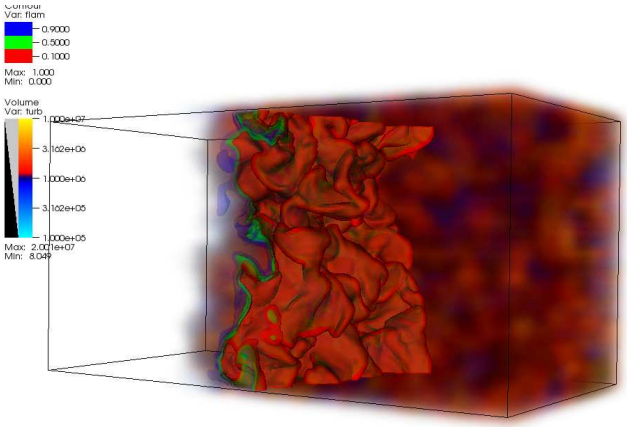

Figure 1. Iso-surface of the reaction progress variable at $\phi = \{0.1, 0.5, 0.9\}$. The volume rendering indicates the turbulent strength with stronger turbulence in orange and weaker in blue. An initially laminar flame propagating at 10 km s^{-1} interacts with decaying turbulence with an initial rms velocity of 100 km s^{-1}.

flame at the densities relevant in the WD is $\lesssim 10^{-1}$ cm, while the WD diameter is $\sim 10^8$ cm. The range of length scales involved in the calculation necessitates the use of a model flame that is resolvable by the computational domain.

Within the standard Chandrasekhar-mass models of SNe Ia, the rising temperature in the core allows carbon fusion before collapse. However, the energy generated from carbon fusion is carried away by convection and a thermonuclear flame is not born for yet another $\sim 10^3$ yr. By the time the energy generation rate exceeds the combined cooling rate from convection and free-streaming neutrinos, the convective region within the core of the WD encompasses $\sim 0.8-1.0$ M$_\odot$ with a root-mean-squared velocity $v_{\rm rms} \sim 300$ km s^{-1} (Zingale et al. 2009). While the character of this flow is still the subject of active research, it is clear the flow will strongly influence the subsequent thermonuclear flame.

The Reynolds number (Re) characteristic of a degenerate WD is practically infinite ($\sim 10^{14}$), which implies that $\ell_t \gg \eta_k$, where ℓ_t is the integral scale of the turbulent cascade and η_k is the dissipation scale due to electron-ion collisions (Woosley et al. 2009). In fact, η_k is typically smaller than the laminar flame width. In order to study the evolution of the early flame, it is necessary to not only to use a model flame, but also a model for unresolved turbulence. Additionally, the model flame should respond correctly to the modeled turbulence. Collectively, these models are known as turbulence–flame interaction (TFI) models. Figure 1 qualitatively shows TFI with the flame front being wrinkled by turbulence, increasing the burning surface area.

In addition to turbulence, the Rayleigh–Taylor (RT) and Kelvin–Helmholtz (KH) instabilities play an important role in generating flame surface in SNe Ia. The inclusion of their combined effects into a model for under-resolved turbulent combustion is a difficult problem (Khokhlov 1995; Schmidt et al. 2006b; Townsley et al. 2008) that we will not address in this work. This is partly due to the desire to assume homogeneous, isotropic turbulence, which is well described by Kolmogorov turbulence theory (Kolmogorov 1941). The inclusion of the RT instability breaks the assumption of isotropy, and greatly increases the complexity of the theoretical model.

Schmidt et al. (2006a, hereafter SNH) recently developed a sub-grid scale (SGS) model to account for under-resolved TFI and applied it to SNe Ia with the inclusion of under-resolved RT-modes in Schmidt et al. (2006b, hereafter SNHR). Part of the motivation for the present study is out of concern of some results in SNH and SNHR. SNH have shown that their method of computing the diffusion of SGS turbulent energy via gradient-diffusion yields an incorrect estimate of the direction of the diffusive flux. Following SNH, Equation (77), the constructed closure parameter underestimates the magnitude of the diffusive flux by an order of magnitude, which because of the dot product, indicates the direction of diffusive flux predicted by gradient-diffusion is different from the true direction. In order to use the gradient-diffusion method, SNH must choose between correctly estimating the direction of diffusive flux or correctly estimating the magnitude. By increasing the value of the closure parameter, they choose to accurately estimate the magnitude, but this choice results in a turbulent kinetic Prandtl number of order 10. From SNHR, Figures 4–6, the magnitude of SGS turbulent energy due to diffusion is comparable to production, and production occurs mostly in the ash behind the flame. Our concern is that the direction of gradient-diffusion is computed to generally align with the direction of flame propagation (since turbulence is generated behind the flame front), and the spread of the flame is dominated by turbulence diffusing from behind the flame to the flame front.

Additionally, SNH assume the interaction between the flame front and turbulence is scale invariant (Pocheau 1994). However, for high-intensity turbulent combustion, the turbulent flame speed has not been observed to scale with the turbulent intensity (Abdel-Gayed & Bradley 1981). The approximation of scale invariance for TFI in degenerate WDs is good near the core where the density is high and the ratio of turbulent intensity to the laminar flame speed is relatively low; however, as the flame propagates to lower densities and approaches conditions predicted for DDT, this approximation is no longer valid. The impact of this approximation on the explosion outcome is not yet known but should be explored.

In this work, we describe an alternative method to enhance the laminar front propagation speed of our model flame. This method is composed of two parts: measuring the SGS turbulent intensity and estimating the turbulent flame speed from the turbulent intensity. We utilize an instantaneous, local measure of the SGS turbulent intensity from the resolved fluid flow. In Section 2, we briefly discuss differences in current flame modeling approaches. In Section 3, we describe the implementation details of the method used to measure resolved turbulence following Colin et al. (2000, hereafter CVDP) and calibrate the operator to the FLASH code. In Section 4, we describe the assumptions made to implement a sub-grid scale TFI model developed by Charlette et al. (2002, hereafter CMV) that follows a sub-grid flame surface density approach. The TFI model provides a turbulent front propagation speed given the local turbulent intensity. In Section 5, we provide simple test problems to verify our scheme behaves as expected. In Section 6, we provide direction for expanding the model to new regimes of validity in future works.

2. BACKGROUND ON FLAME MODELING

Several approaches have been used to model flames, all of which will not be discussed here. Instead we focus the discussion towards the differences between artificially thickened flames and flame front tracking methods. Artificially thickened flames model the combustion as one might in a direct numerical simulation (DNS) with "simple chemistry" using

an Arrhenius law, except that the molecular and thermal diffusivities are increased by a thickening factor, such that the real flame structure is resolved on the computational domain. On the other hand, flame front tracking methods such as the *G*-equation (Schmidt et al. 2006a) and advection-reaction-diffusion (ARD or ADR) equation (Khokhlov 1995), do not retain information about the flame structure.

The thickened flame approach has the advantage of incorporating various phenomena naturally, such as effects due to flame curvature and stretch, by using the Arrhenius law. This is due to the fact that the flame structure is retained, including the pre-heat zone and the reaction zone. This structure is especially important for astrophysical flames in which the Lewis number (Le) is nearly infinite, *i. e.*, thermal diffusion dominates over species diffusion. This approach works well when the thickening factor is a few, such that not much flame structure can hide on unresolved scales; however, for large thickening factors, it is not obvious that the thickened flame structure represents the average behavior of the flame on unresolved scales.

For our simulations of SNe Ia in FLASH, the laminar flame width is under-resolved by a factor ranging $10^6 - 10^{10}$. In this case, we do not necessarily expect the model flame structure to behave the same way as the real physical flame. Instead, we use an ADR equation to define an implicit interface to the flame front, with the reaction and diffusion terms determined dynamically to provide a desired front-propagation speed and interface width (see Khokhlov 1995; Vladimirova et al. 2006; Townsley et al. 2007, 2009). Rather than having a peaked energy-generation rate in the reaction zone as with the Arrhenius law, the energy generated from combustion is smoothly distributed over the interface. This approach has the advantage of producing an acoustically quiet flame front, a feature not necessarily shared with the *G*-equation. Additionally, the energy release is entirely dominated by species diffusion rather than thermal diffusion; however, it is important to note that the ADR scheme is not intended to represent physical flame structure. A model is required to inform the ADR flame how fast to propagate given local conditions such as the local thermodynamic quantities, composition, and turbulent intensity.

3. MEASURING UNRESOLVED TURBULENCE

We want to measure resolved turbulent motions that are not caused by the expansion of material as it is burned. This component of turbulence can be argued to exist ahead of a propagating burning front such that it wrinkles the front and influences the local burning rate. CVDP describe a finite-difference operator "OP_2" to measure resolved turbulence with the expanding velocity component filtered out

$$OP_2(u) = (h\Delta_x)^3 \left| \boldsymbol{\nabla} \times \left(\nabla^2 u \right) \right|, \tag{1}$$

$$u'_\Delta = c_2^h OP_2(u), \tag{2}$$

where c_2^h is a calibrated constant, h is the index of the stride in the finite difference scheme, and Δ_x is the grid spacing. The constant c_2^h is determined by requiring that the kinetic energy of the turbulent velocity measured be equal to the kinetic energy contained in the turbulent cascade between Δ and the physical dissipation scale (η_k). Because the dissipation range of resolved turbulent flows begins well above the grid scale, the length scale Δ associated with the turbulence operator typically lies within the dissipation range, where Δ depends on h and Δ_x. Therefore, c_2^h serves to correct for the effects of numerical dissipation. This formulation allows some flexibility in Δ by choosing different values for the integer stride h. In general, c_2^h will depend on the choice of h and the numerical method used to evaluate Equation (1) (see Sytine et al. 2000 for more details about numerical dissipation with PPM). We use a fourth-order finite central difference with

$$\frac{\partial f}{\partial x} = \frac{f_{i-2h} - 8f_{i-h} + 8f_{i+h} - f_{i+2h}}{12h\Delta_x} \tag{3}$$

$$\frac{\partial^2 f}{\partial x^2} = \frac{-f_{i-2h} + 16f_{i-h} - 30f_i + 16f_{i+h} - f_{i+2h}}{12h^2\Delta_x^2}. \tag{4}$$

For this particular implementation, the length scale associated with the turbulence operator is approximated by $\Delta = 4h\Delta_x$, because the turbulence measured in a particular cell uses velocity information from cells up to $4h$ cells away.

For FLASH, we calibrate c_2^h using a Kolmogorov turbulence cascade generated by driving fluid motions on large scales. We drive turbulence in a triply-periodic Cartesian box with varying resolutions for 1.5 eddy-turnover times (τ_e), where $\tau_e = L/v_{\rm rms}$, L = 15 km is the size of the box, and $v_{\rm rms}$ is the root-mean-squared velocity of the resolved flow. We follow the simulation setup `StirTurb` distributed with FLASH (Fisher et al. 2008), except that we use a degenerate equation of state, the same as that used for our simulations of SNe Ia, with $\rho = 7.3 \times 10^7$ g cm^{-3} and $T = 4.3 \times 10^9$ K. We drive the turbulence at a scale $L/3$ with an energy to achieve $v_{\rm rms} \approx 0.1 c_s$, where $c_s \approx 6 \times 10^3$ km s^{-1} is the sound speed. The turbulence cascade for all simulations converge to a single steady-state profile in phase space by $t = 1.5\tau_e$. Because we want to correct for numerical dissipation, we construct an idealized energy cascade that follows the well-known $-5/3$ power law for homogeneous and isotropic turbulence, *i. e.*, $E(k) = Ak^{-5/3}$ergscmg^{-1}, where k is the norm of the vector wavenumber and A is a proportionality constant. This energy function represents the turbulence we would expect if we had infinite resolution (and no numerical dissipation). We solve for A by realizing that integrating over the energy function from the integral scale (ℓ_t) to η_k is equal to the kinetic energy per unit mass

$$\int_{2\pi/\ell_t}^{2\pi/\eta_k} E(k)dk = \frac{1}{2} v_{\rm rms}^2, \tag{5}$$

where $\ell_t = L/3$, the scale at which turbulence is driven. For the astrophysical flows of interest, Re $\sim 10^{14}$ such that $\eta_k \ll \ell_t$ and the upper bound of the integrand goes to infinity. Then, defining $k_{\rm drive} = 2\pi/\ell_t$, A becomes

$$A = \frac{1}{3} v_{\rm rms}^2 k_{\rm drive}^{2/3}, \tag{6}$$

We want u'_Δ to represent the turbulent energy on unresolved scales ($E_{\rm SGS}$), so instead of integrating from the driving scale, we integrate from the wave number corresponding to the length scale associated with the turbulence operator, $k_\Delta = 2\pi/\Delta$

$$E_{\rm SGS} = \int_{k_\Delta}^{\infty} E(k)dk = \frac{3}{2} A k_\Delta^{-2/3}. \tag{7}$$

The calibration constant is then derived from the desire for

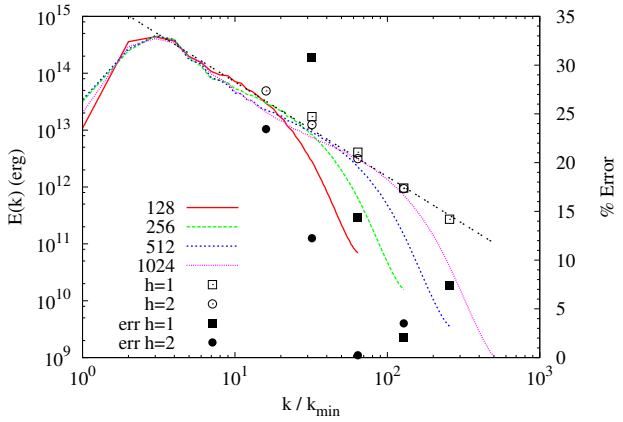

Figure 2. The spectral energy content for four different resolutions that range 128–1024 computational cells along one dimension are shown as a function of wave number in units of $k_{\rm min} = 2\pi/L$. The open points show $E(k = k_\Delta)$, the energy contained in the length scale Δ (for different integer strides h), as inferred from the turbulence operator (see text for details). The dashed line is computed from $E(k) = Ak^{-5/3}$ and Equation (6) showing the expected $-5/3$ power-law. Because each resolution results in a slightly different calibration for c_2^h, we choose one representative value (provided in Table 1) and show the error in the turbulent intensity with filled points associated with the second y-axis using Equation (9).

$$u'^{\,2}_\Delta = 2E_{\rm SGS}$$

$$(c_2)^2 = \frac{2E_{\rm SGS}}{\langle OP_2(u)^2\rangle} = \frac{v_{\rm rms}^2}{\langle OP_2(u)^2\rangle}\left(\frac{k_{\rm drive}}{k_\Delta}\right)^{2/3}. \qquad (8)$$

Figure 2 shows the spectral energy content for four different resolutions that range 128–1024 computational cells along one dimension. The energy spectra are computed by taking the Fourier transform of the velocity field and binning energy in spherical shells of wavenumber $k = \sqrt{k_x^2+k_y^2+k_z^2}$. The Fourier transforms are computed using the publicly available FFTW routines, with a normalization of $1/\sqrt{N}$ where N is the product of the number of cells in each direction. From the energy spectrum, the driving scale can be discerned as $k_{\rm drive} = 3k_{\rm min}$, as specified in the simulation. The dashed line is computed from $E(k) = Ak^{-5/3}$ and Equation (6) with $v_{\rm rms}$ from the 1024-resolution simulation. The open points show what the turbulent operator infers the energy to be at a particular wavenumber, where $E(k) = 2E_{\rm SGS}/3k$. Because each resolution results in a slightly different calibration for c_2^h provided in Table 1, we choose one representative value and show the error in the turbulent intensity with filled points associated with the second y-axis, where the error is given by

$$\%\ {\rm err}\left(u'_\Delta\right) = \frac{{\rm abs}\left(u'_\Delta - \sqrt{2E_{\rm SGS}}\right)}{\sqrt{2E_{\rm SGS}}} \times 100, \qquad (9)$$

which reduces to

$$\%\ {\rm err}\left(u'_\Delta\right) = {\rm abs}\left(\frac{c_2}{c_{2,N}} - 1\right) \times 100. \qquad (10)$$

4. TURBULENCE–FLAME INTERACTION MODEL

A turbulence–flame interaction (TFI) model estimates the turbulent flame speed from the characteristics of the turbulent cascade and the laminar flame. For the TFI models discussed in this work, we limit our analysis to combustion regimes in which the flame is a well-defined concept.

Table 1
Calibrated Constants c_2^h for Varying Resolutions N

N	128	256	512	1024	c_2
h = 1	0.688159	0.786560	0.919036	0.972137	0.9
h = 2	0.243039	0.267279	0.300725	0.310929	0.3

4.1. *Model Construction and Comparison*

We implement a few models based on CVDP and CMV, finally deciding that CMV is most appropriate for simulations of SNe Ia with FLASH. While we summarize the approaches here, see CVDP and CMV for a full description. CVDP specifically investigate a model applicable to artificially thickened flames. Using direct numerical simulations (DNS) of single flame–vortex interactions, they investigate the efficiency of the vortex to wrinkle the flame when the ratio of the vortex size (r) to laminar flame width and ratio of the vortex velocity (v') to the laminar flame speed varies. A subgrid scale model is constructed by calculating the effective strain rate on the flame by integrating the efficiency of single flame–vortex interactions (computed from DNS) through the unresolved inertial range of the turbulent cascade. In addition, CVDP attempt to account for inefficient wrinkling of the artificially thickened flame by resolved turbulence. The turbulent enhancement to the laminar flame speed is taken to be the ratio of wrinkling factors between the thickened flame and physical flame. Because of this construction, the wrinkling factors must be normalized to reproduce the limiting behavior of Damköhler scaling, *i.e.*, the turbulent flame speed scales with the turbulent intensity ($s_{\rm t} \propto u'$). This normalization requires integral scale quantities to be known, such as the integral scale (ℓ_t), turbulent intensity (u'), and Reynolds number (Re).

CMV point out that methods used to measure turbulence on scales larger than the artificially thickened flame are impractical in most simulation codes. In practice, the length scale used to measure turbulence is approximately the same as the length scale used to resolve the thickened flame. Therefore, CMV neglect inefficient wrinkling of the artificially thickened flame and focus on modeling the wrinkling of the unresolved physical flame. They apply the techniques described by CVDP to a flame that is fractal in nature, where there is a defined inner and outer length scale associated to the structure, but where the fractal dimension could depend on other local properties. CMV postulate that the inner length scale is the inverse mean curvature of the flame, which they solve for directly using the flame surface density balance equation and the hypothesis that flame surface destruction and production are in equilibrium on unresolved scales. This construction requires only grid-scale quantities to be known since normalization is not required. The only stipulation to recover Damköhler scaling is that, in this limit, the fractal dimension of the flame should be $D = 7/3$.

4.2. *Application to Astrophysical Flames*

In order to apply these models to flames in SNe Ia, we must revisit assumptions and model choices that may be different in an astrophysical context. In particular, we consider a different normalization for the parameter α in CVDP used to recover Damköhler scaling. To implement CMV, we recalculate numerical integrals with a dependence on the Prandtl number

(Pr) and confirm fitting functions developed for Pr ~ 1 also apply to low-Pr flames.

In CVDP, the enhancement to the laminar flame speed is given by the ratio of the wrinkling factor for the thin flame to the wrinkling factor for the thick flame, $E = \Xi^0/\Xi^1$. Here, the superscript 0 refers to the real physical "thin" flame, and the superscript 1 refers to the model "thick" flame. The wrinkling factor is given by equating sub-grid flame surface production from turbulent wrinkling to subgrid flame surface destruction by propagation and diffusion from the subgrid flame surface density balance equation in CVDP, Equation (18):

$$\Xi \approx 1 + \alpha \frac{\Delta}{s_l^0} \langle a_T \rangle_s , \tag{11}$$

where α is a model constant, Δ is the length scale associated with the turbulence operator, and $\langle a_T \rangle_s$ is the effective strain rate averaged over the flame surface on subgrid scales. The effective strain rate is given by CVDP, Equation (24) calculated by integrating turbulent motions over the inertial range by an efficiency function derived from DNS calculations:

$$\langle a_T \rangle_s = \frac{c_{ms}}{\ln(2)} \int_{\text{scales}} C\left(\frac{r}{\delta_l^1}, \frac{v'}{s_l^0}\right) \frac{v'}{r} d\left[\ln\left(\frac{\ell_t}{r}\right)\right], \tag{12}$$

where c_{ms} is a constant determined from DNS calculations (Yeung et al. 1990) and s_l^0 refers to the unstrained laminar flame speed (superscript 0 referring to unstrained). In order to evaluate the limiting case of Damköhler scaling ($\Xi \approx 1 + u'/s_l^0$), a simple Heaviside efficiency function is introduced with a cut-off scale δ_l^c, such that $C = 0$ for $r < \delta_l^c$ and $C = 1$ for $r > \delta_l^c$. In this case, the integral can be solved analytically with the caveat that $\delta_l^c \geq \eta_k$:

$$\alpha = \beta \frac{2\ln(2)}{3c_{ms}} \left[\left(\frac{\ell_t}{\delta_l^c}\right)^{2/3} - 1\right]^{-1}, \tag{13}$$

where β is a model constant of order unity. We describe two procedures to calculate α that lead to two different models.

4.3. *Full Inertial Range Model*

CVDP argue Damköhler scaling is achieved only when the flame front is wrinkled by *all* turbulent motions in the inertial range, from η_k to ℓ_t. This hypothesis defines the model we call the "Full Inertial Range" (FIR) model. For astrophysical flames, typically $\eta_k \ll \delta_l^0$, which means that α will be relatively small, and the model will not predict much enhancement.

CVDP let $\delta_l^c = \eta_k$ to evaluate α in Equation (13). When $\delta_l^c = \eta_k$, $\left(\ell_t/\delta_l^c\right)^{2/3} = \text{Re}^{1/2}$. Here, the evaluation of Re becomes important, where $\text{Re} = \ell_t u'/\nu$, and integral scale quantities are necessary. We prefer to write Re in terms of the ratios u'_Δ/s_l^0 and Δ/δ_l^0

$$\text{Re}_\Delta = \frac{u'_\Delta}{s_l^0}\frac{\Delta}{\delta_l^0}\frac{s_l^0\delta_l^0}{\nu} = \frac{u'_\Delta}{s_l^0}\frac{\Delta}{\delta_l^0}\text{Pr}^{-1}, \tag{14}$$

where $s_l^0 \approx \sqrt{\kappa/\tau_r}$ and $\delta_l^0 \approx \sqrt{\kappa\tau_r}$, such that $s_l^0\delta_l^0 = \kappa$, where κ is the thermal diffusion coefficient and τ_r is the reaction timescale. Then, $\text{Pr} = \nu/\kappa$. Here, δ_l^0 refers to the physical laminar flame width; whereas, δ_l^1 will refer to the model flame width. Re at the integral scale can be evaluated with $\Delta = \ell_t$. For terrestrial flames, Pr ~ 1 with CVDP choosing $\text{Pr} = 1/4$; however, astrophysical flames characteristic for a degenerate WD have Pr as low as 10^{-5} (Nandkumar & Pethick 1984; Niemeyer & Kerstein 1997; Kerstein 2001). In our simulations, integral scale quantities are not easily accessible and it's useful to solve for α at the scale Δ such that

$$\Xi_\Delta = 1 + \alpha \frac{\Delta}{s_l^0} \langle a_T \rangle_s = 1 + \beta \frac{u'_\Delta}{s_l^0}. \tag{15}$$

This means that the turbulent flame speed at the scale Δ obeys Damköhler scaling when all turbulent motions of size r with $\delta_l^c < r < \Delta$ wrinkle the flame with full efficiency. For the implementation in which $\delta_l^c = \eta_k$, we obtain

$$\alpha_{\text{FIR}} = \beta \frac{2\ln(2)}{3c_{ms}} \text{Re}_\Delta^{-1/2}. \tag{16}$$

For low-Pr flames, we never actually recover $\Xi_\Delta = 1 + \beta u'_\Delta/s_l^0$ because $\eta_k < \delta_l^0$. For this reason, we consider another normalization to solve for α.

4.4. *Gibson Scale Model*

Instead of only allowing Damköhler scaling when the flame is wrinkled by the full inertial range, we allow Damköhler scaling when the flame is influenced by all turbulent eddies ranging from Δ to the flame scale, letting $\delta_l^c = \delta_l^0$. This hypothesis defines the model we call the "Gibson Scale" (GS) model, because Damköhler scaling is only achieved when the Gibson length scale equals the physical laminar flame width ($\ell_G = \delta_l^0$), where

$$\ell_G = \ell_t \left(\frac{u'}{s_l^0}\right)^{-3}. \tag{17}$$

Based on timescale arguments, turbulent motions in a Kolmogorov cascade on length scales $r < \ell_G$, should not influence the flame. With $\Delta/\delta_l^0 \gg 1$, the evaluation of α becomes

$$\alpha_{\text{GS}} = \beta \frac{2\ln(2)}{3c_{ms}} \left(\frac{\Delta}{\delta_l^0}\right)^{-2/3}. \tag{18}$$

The purpose of the FIR and GS model approaches is to account for inefficient wrinkling of the artificially thickened model flame due to resolved turbulence, while still accounting for unresolved turbulence–flame interactions. However, if the length scale used to resolve the model flame (δ_l^1) is approximately the same as Δ, then the wrinkling factor of the model flame $\Xi_\Delta^1\left(\delta_l^1 \sim \Delta\right) \approx 1$. With this insight, it may be impractical to try to account for inefficient wrinkling of the model flame, and a normalization parameter α may not be necessary.

4.5. *Power-Law Flame Wrinkling Model*

CMV describe their power-law flame wrinkling (PLFW) model by revisiting the analysis of CVDP. CMV neglect inefficient wrinkling of the artificially thickened model flame because $\Xi^1 \approx 1$ (*i. e.*, $E = \Xi^0$) and postulate that the wrinkling factor is described by CMV, Equation (3):

$$\Xi_\Delta = \left(1 + \frac{\Delta}{\eta_c}\right)^\gamma, \tag{19}$$

where γ is not necessarily constant. If γ is independent of scale and restricted to $0 < \gamma < 1$, the fractal model is recovered where the fractal dimension $D = \gamma + 2$. In the limit

of strong turbulence, $\gamma = 1/3$ in order to recover Damköhler scaling as shown in Figure 4. The inner cut-off scale η_c is estimated to be the inverse mean curvature of the flame ($\left|\langle\nabla\cdot n\rangle_s\right|^{-1}$) given in CMV, Equation (10):

$$\left|\langle\nabla\cdot n\rangle_s\right| = \Delta^{-1}\frac{u'_\Delta}{s_l^0}\Gamma\left(\frac{\Delta}{\delta_l^0},\frac{u'_\Delta}{s_l^0},\mathrm{Re}_\Delta\right), \tag{20}$$

which is solved from the equilibrium condition of subgrid flame surface density production and destruction. The inverse mean curvature is related to the Gibson scale, although it is not immediately obvious. If solve for Γ from CVDP, Equation (29),

$$\Gamma = \frac{\langle a_T\rangle_s}{u'_\Delta/\Delta}, \tag{21}$$

using the Heaviside function as an approximation to the efficiency function in Equation (12) to solve for $\langle a_T\rangle_s$ while letting $\delta_l^c \approx \ell_\mathrm{G}$, then

$$\left|\langle\nabla\cdot n\rangle_s\right|^{-1} \approx \frac{2\ln 2}{3c_{ms}}\ell_\mathrm{G}. \tag{22}$$

By using an efficiency function derived from DNS of flame–vortex interactions, the inverse mean curvature provides a better cut-off scale influenced by direct measurement rather than ℓ_G that serves as an order-of-magnitude estimate from dimensional analysis.

CMV prevent the unphysical result, $\eta_c < \delta_l^0$, with

$$\eta_c = \max\left(\left|\langle\nabla\cdot n\rangle_s\right|^{-1},\delta_l^0\right). \tag{23}$$

This limiting behavior provides a natural and physical way to quench flames. Even for a space-filling flame with $\gamma = 1$, there is a finite amount of flame surface that can physically exist on unresolved scales for a finite-width flame. Models currently in use, including Khokhlov (1995) and SNHR, do not consider this effect, which may be important for combustion in SNe Ia for the density range $10^7 - 10^8$ g cm^{-3}. Instead, these approaches typically set $s_{t\Delta} = 0$ for $\rho < 10^7$ g cm^{-3}, where ρ is the fuel density.

The spectral efficiency function Γ utilizes a modified efficiency function C, such that vortices with speed $v' < s_l^0/2$ do not wrinkle the flame. Additionally, the integration over length scales is performed in phase-space in CMV, Equation (13):

$$\left(\Gamma\frac{u'_\Delta}{\Delta}\right)^2 = \int_{\pi/\Delta}^{\infty}[C(k)]^2 k^2 E_{11}(k)\,dk, \tag{24}$$

where $E_{11}(k)$ is the one-dimensional energy spectrum describing homogeneous, isotropic turbulence in the direction of the wavenumber k, given in CMV, Equation (16). Because $E_{11}(k)$ depends on Pr, we re-evaluate the numerical integral for Pr = 10^{-5} to compare with fitting functions provided by CMV in Figure 3. Numerical integrals are computed using CMV, Equations (18–21) and Equation (14) with subroutine `dqag` from the publicly available `SLATEC` library. Because the integrand is non-oscillatory, smooth and tends toward zero exponentially as the argument goes to infinity, we choose an upper bound to the integral such that the integrand evaluates to a number less than 10^{-10}. This criterion is sufficiently small as compared to the integrand evaluated at the lower bound. A good initial guess at the upper bound is given by 10^3 multiplied by CMV, Equation (26). We evaluate Γ with an error

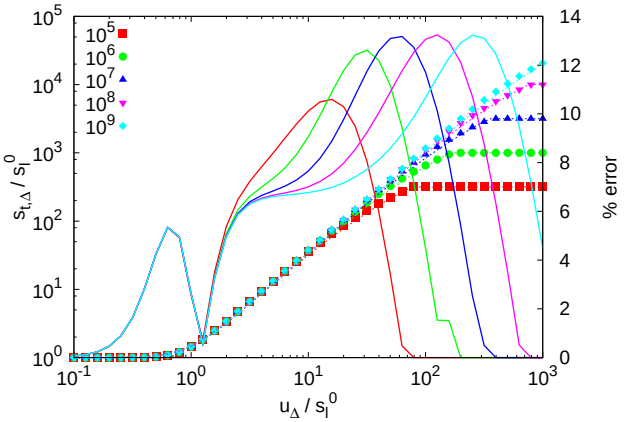

Figure 3. The enhancement to the laminar flame speed for Pr = 10^{-5} is shown as a function of the ratio of the turbulent intensity at the scale Δ to the laminar flame speed (u'_Δ/s_l^0) on the x-axis and the ratio of Δ to the laminar flame width (Δ/δ_l^0) with different colors. The numerically integrated values are shown as points while the fit values are shown as thin dashed lines. The percent error between the fit and the numerically integrated result are shown as thick solid lines with the error given on the second y-axis. The range of values chosen represents the range of expected values for a moderate resolution SNe Ia simulation. The fit-errors are all $\lesssim 10\%$.

tolerance of 0.1% and found that a Gauss–Kronrod pair with 15 − 31 points provides consistent results for a wide range of parameter space. We also use the fitting function for Γ given in CMV, Equations (30–34) in a range outside that explored by CMV. We compare numerically integrated values (points) to the fit (thin lines) for $\Delta/\delta_l^0 = 10^5 - 10^9$ and a range of u'_Δ/s_l^0 up to 10^3. The associated percent errors are provided as thick lines in Figure 3.

4.6. *Comparing Models*

In Figure 4, a simple Kolmogorov cascade is constructed with $u' = 300$ km s^{-1} and $\ell_t = 100$ km, where both the laminar flame speeds and widths are log–log fits as functions of density for a 50/50 C-O fuel mixture from Chamulak et al. (2007) with Pr = 10^{-5}. The red and green lines are constructed using the FIR and GS models with Equations 16 and 18. The blue line shows the limiting behavior with $\Xi_\Delta = 1 + \beta u'_\Delta/s_l^0$, while the black line is the fitted laminar flame speed. For comparison, results from the PLFW model with $\gamma = 1/3$ corresponding to the limiting Damköhler scaling behavior are shown in magenta. In all cases, these estimates were calculated with $\Delta = 16$ km, which is approximately the length scale associated with the turbulence measure for $h = 1$ in a 4 km resolution simulation. The cut-off to $s_{t\Delta}$ that has typically been used in previous models (Schmidt et al. 2006b; Townsley et al. 2007) is given by the vertical dashed line. This line corresponds to estimates of the density at which combustion in a degenerate WD transitions from the flame-let regime to the "distributed burning" or "broken reaction zone" regime. This estimate is typically derived from the condition that $\ell_\mathrm{G} = \delta_l^0$. If this transition occurs, the flame is no longer a well-defined concept, and the assumptions used in the construction of the models for turbulent combustion are no longer valid.

Given the arguments by CMV that $\Xi^1 \approx 1$ and the ambiguities associated with choosing a cut-off scale δ_l^c in the FIR and GS models derived from CVDP, we choose to implement the PLFW model. The PLFW model provides a more natural mechanism to quench turbulent flames rather than supplying

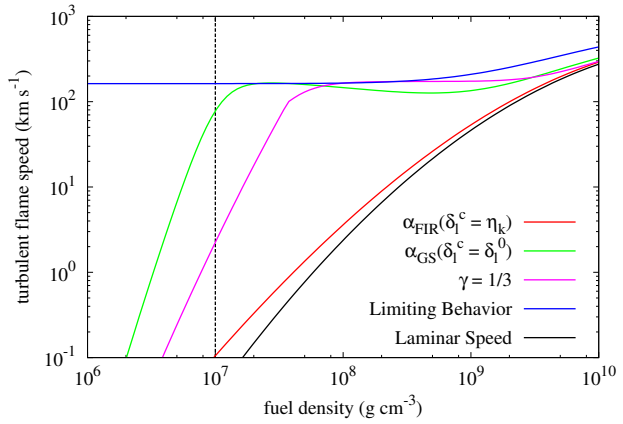

Figure 4. The turbulent flame speed is estimated using a simple Kolmogorov cascade constructed with $u' = 300$ km s^{-1} and $\ell_t = 100$ km, where both the laminar flame speeds and widths are log–log fits as functions of density for a 50/50 C-O fuel mixture from Chamulak et al. (2007) with Pr = 10^{-5}. The red and green lines are constructed using the FIR and GS models with Equations 16 and 18. The blue line shows the limiting behavior with $\Xi_\Delta = 1 + \beta u'_\Delta / s_l^0$, while the black line is the fitted laminar flame speed as a function of fuel density. For comparison, results from the PLFW model using a $\gamma = 1/3$ power-law are shown in magenta. In all cases, $\Delta = 16$ km. The cut-off to $s_{t\Delta}$ that has typically been used in previous models occurs at the suspected transition away from the flame-let regime (vertical dashed line) (Schmidt et al. 2006b; Townsley et al. 2007).

some ad-hoc prescription as in other models (Schmidt et al. 2006a; Townsley et al. 2007). Additionally, the implementation requires only grid-scale quantities, which are computationally accessible.

5. VERIFICATION

In order to test our implementation of the PLFW subgrid-scale TFI, we use a simple 1-stage model flame described in Vladimirova et al. (2006); Townsley et al. (2007). The model flame is described by a reaction progress variable, ϕ, that is evolved by an advection-reaction-diffusion equation where the reaction and diffusion terms are chosen to yield a specified front propagation speed and model flame width (Khokhlov 1995). The use of a 1-stage burner with a known energy release results in an analytic solution to the Rankine-Hugonoit jump conditions across the flame used to set up the initial conditions. For our tests, our flame burns a 50/50 carbon-oxygen mixture by mass to 50/50 oxygen-magnesium, which is equivalent to the simplified prescription of the carbon burning stage in our 3-stage flame model that is designed to capture the energetics (Townsley et al. 2007). For simplicity, we specify constant laminar flame speed properties with a speed of 10 km s^{-1} and physical width of 10^{-3} cm. The flame is initialized in the center of a box that is four times longer than it is wide using Cartesian coordinates with the model flame resolved using four zones propagating in the positive direction of the first dimension. Subsonic inflow and outflow boundary conditions motivated by Poinsot & Veynante (2005) are imposed. A subsonic inflow boundary condition is used with an inflow velocity initially equal to the specified front propagation speed such that the model flame remains in the center of the box. The inflow velocity is allowed to vary for turbulent flows such that fuel is in-flowing at the burning rate

$$v_{\rm inflow} = \frac{\dot{m}_b}{A_{\rm inflow}\rho_{\rm fuel}}, \tag{25}$$

where $v_{\rm inflow}$ is the inflow velocity defined to be positive in the $-x$ direction, $\dot{m}_b$ is the burning rate and $A_{\rm inflow}$ is the cross-sectional area of the inlet. The burning rate is calculated from the change in mass of ash on the grid between time steps and the ash outflow rate

$$\dot{m}_b = \frac{m^n_{\rm ash} - m^{n-1}_{\rm ash}}{t^n - t^{n-1}} + \langle \rho v_{\rm outflow} \rangle A_{\rm outflow}, \tag{26}$$

where $v_{\rm outflow}$ is the outflow velocity defined to be positive in the $-x$ direction, $A_{\rm outflow}$ is the cross-sectional area of the outlet, $m_{\rm ash} = \int \phi \rho \, dV$ and t^n denotes the n-th time step. A static-pressure subsonic outflow boundary condition is imposed that conserves mass and energy through the boundary using the steady-state Euler equations and divergence theorem assuming zero-gradient velocities in orthogonal directions. Because the steady-state continuity equation is satisfied, $\rho v_{\rm outflow}$ is constant across the boundary allowing an average over the interior boundary cells. A static-pressure outflow reflects sound waves back into the computational domain, which are necessary to stabilize the flow. The inflow temperature is strictly maintained, while the inflow velocities are allowed to vary to ensure acoustic reflections back into the computational domain are dampened. If perfectly reflecting boundary conditions are used on both the outflow and inflow, sound waves never leave the computational domain. Periodic boundary conditions are imposed in the second and third dimensions.

Our verification tests include simulating a laminar flame in a channel with varying resolutions from 64x64 to 256x256 zones in cross-sectional resolution. Because the initial profile given for the reaction progress variable, ϕ, is not equal to the true steady state profile, it takes tens of sound-crossing times to obtain a steady state solution. Firstly, we verify that for perfectly laminar flow, the TFI model recovers the laminar flame speed as expected. Afterwards, we restart the simulation by superimposing a turbulence field with a specified turbulent intensity in the fuel. The turbulence field used is the same as the 1024^3-resolution run used to calibrate the constant c_2 in Section 3 with the velocities normalized by $v_{\rm rms}$. In addition, velocities are smoothed via direct averaging to obtain lower-resolution turbulent velocity fields. This procedure allows a direct comparison of the TFI model as the inertial range of the turbulent cascade is better resolved. The power spectra of the smoothed velocity fields is provided in Figure 5. These simulations are computed for various resolutions to verify that the combined effects of resolved and unresolved TFI result in a consistent overall turbulent flame speed independent of the grid resolution.

In each of these tests, the flame speed is computed with

$$s_A = \frac{\dot{m}_b}{A \langle \rho_{\rm fuel} \rangle}, \tag{27}$$

where s_A is the flame speed computed from using area A, which is the surface area of an iso-contour of the reaction progress variable to compute the front-propagation speed or the cross-sectional area of the channel to compute the turbulent flame speed. In the case of an iso-contour, the surface area is computed using the marching cubes algorithm. We estimate the fuel density by assuming a low-Mach number isobaric burn and solving for $\rho(\phi = 0)$ from (Vladimirova et al. 2006)

$$e(p,\rho) + \frac{p}{\rho} + q\phi = const \tag{28}$$

$$p = const, \tag{29}$$

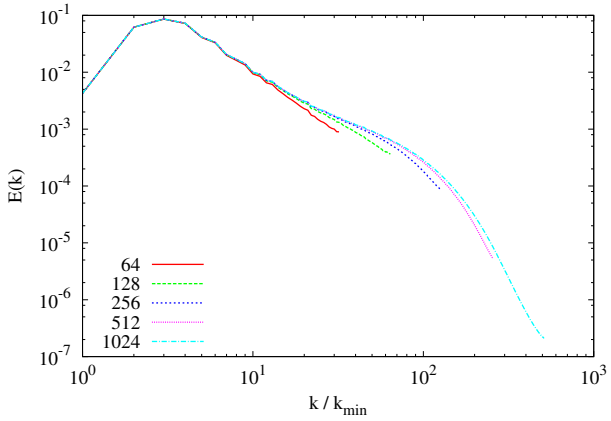

Figure 5. The normalized spectral energy content for smoothed velocity fields resulting from the 1024^3-resolution turbulence run in Figure 2 as a function of wavenumber in units of $2\pi/L$.

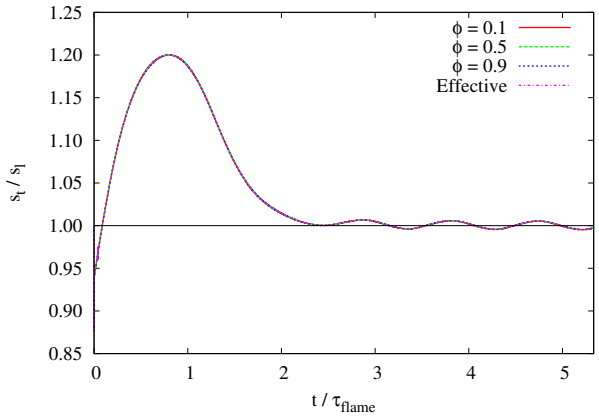

Figure 6. The ratio of the front propagation speed to input speed of the iso-contours of the reaction progress variable for $\phi = \{0.1, 0.5, 0.9\}$ (red, green, and blue lines, respectively) as well as the turbulent flame speed (magenta) are compared. The initial flow is computed by solving the Rankine-Hugonoit jump conditions in the reference frame of the flame such that the flame remains in the center of the domain (Vladimirova et al. 2006). The small oscillations in the estimated flame speed are discussed in Townsley et al. (2007).

where q is the total energy released through the burn, p is the pressure, and e is the specific internal energy determined from the equation of state. The averaging procedure is performed on densities just ahead of the flame with $10^{-6} < \phi < 5 \times 10^{-2}$.

5.1. *Recovering the Laminar Flame Speed*

We test the implementation of u'_Δ in Equation (2) and the PLFW subgrid-scale TFI model in the limit of $u'_\Delta / s_l^0 \to 0$. In this limit, the turbulence operator is constructed to ignore the expansion of material due to laminar flame propagation and $u'_\Delta = 0$ should be observed. In addition, the TFI model should calculate the enhancement $\Xi_\Delta = 1$ such that $s_{t\Delta} = s_l^0$. For this test, we fix the inflow velocity equal to the input front-propagation speed and do not allow it to vary. In Figure 6, we plot the ratios of the front-propagation speeds to the input speed of the iso-contours of the reaction progress variable for $\phi = \{0.1, 0.5, 0.9\}$ as well as the turbulent flame speed compared. All estimated flame speeds are perfectly consistent with one another indicating that the area of each iso-contour and the cross-sectional area of the channel are all equivalent. The initial adjustment and subsequent oscillation of the $\phi(x)$ profile is related to the flame self-crossing time $\tau_{\rm flame} = \delta_l^1 / s_l^0$, which is described in detail in Townsley et al. (2007). This shows that the turbulence operator indeed measures $u'_\Delta = 0$ and that the resulting flame speed is equivalent to the laminar (or input) flame speed.

5.2. *Convergence Study*

By increasing the resolution of the computational domain, more of the turbulent cascade is resolved and wrinkling of the flame is captured directly. By virtue of using a sub-grid scale model to account for unresolved turbulence, we expect that combined effects of unresolved and resolved turbulence should result in the same global turbulent flame speed independent of the resolution chosen. Figure 7 and Figure 8 show the results of three different simulations each with 64^2, 128^2, and 256^2 cells resolving the plane orthogonal to the direction of propagation. Figure 7 shows results if an SGS model is not used, and Figure 8 shows results using the SGS model implemented in this work. Initially, the turbulent velocity field is scaled to $v_{\rm rms} = 100\ {\rm km\,s^{-1}}$. The global turbulent flame speeds computed from the fuel consumption rates are given by the thick solid lines, which are consistent with one another. The front-propagation speeds of iso-contours of the reaction progress variable $\phi = \{0.1, 0.5, 0.9\}$ are given as dashed, dotted, and dot-dashed lines with the $\phi = 0.5$ line thickened to illustrate that with increased resolution, the unresolved portion of the inertial range contributes less to the global turbulent flame speed. Because the turbulence field is not driven in the fuel ahead of the flame, the turbulent velocity decays relatively quickly. In a separate calculation, the 256^3-resolution run from Section 3 was restarted with no stirring to characterize the decaying turbulence field. The decaying power spectra maintain a Kolmogorov spectrum, while $v_{\rm rms}$ is described by

$$v_{\rm rms,decay}(t) = A e^{-t/\tau_e(t)}, \tag{30}$$

where $\tau_e(t) = B * t + C$ is the eddy turn-over timescale, which is a linear function of t. As the velocity decays, the eddy turn-over timescale increases. The constants A, B, and C were determined using least-squares fits with $A = 1.448 v_{\rm rms,0}$, $B = 0.3549 \tau_{e,0}$, and $C = 0.415 \tau_{e,0}$. An eddy turn-over time is approximated by $\tau_e = L / v_{\rm rms}$ where $L = 15$ km. Therefore, an estimate of the turbulent velocity at a particular scale is provided by

$$u'_\Delta(t) = v_{\rm rms,decay}(t) \left(\frac{\Delta}{L} \right)^{1/3}. \tag{31}$$

An estimated turbulent flame speed is calculated analytically using the TFI model and provided for comparison in Figure 8.

6. FUTURE CONSIDERATIONS

In order to improve upon this model, DNS calculations of single vortex-flame interactions should be computed for low-Pr, high-Le flames to verify the efficiency function for astrophysical flames. Unfortunately, these calculations are expensive and outside the scope of the present study. Zingale et al. (2001) provided preliminary results of exactly this calculation; however, a more comprehensive and complete analysis is required.

Future calculations should also consider flame curvature and stretch effects, especially for high-Le flames. Currently,

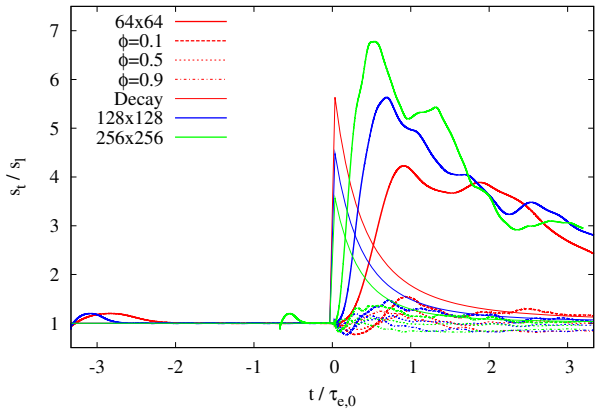

Figure 7. The ratio of the front propagation speed to input speed of the iso-contours of the reaction progress variable for $\phi = \{0.1, 0.5, 0.9\}$ (dashed, dotted, and dot-dashed lines, respectively) as well as the turbulent flame speed (thick solid lines) are compared to the estimated turbulent flame speed from the decaying turbulence (thin solid lines). Cross-sectional resolutions of 64x64 (red), 128x128 (blue), and 256x256 (green) are compared by superimposing a turbulent velocity field in the fuel with $v_{\rm rms}$ = 100 km s^{-1}. The flow is not driven, so the turbulence field decays from numerical dissipation at the grid scale and the estimated front-propagation speeds of iso-contours of ϕ return to the input front-propagation speed. An SGS model is not used for these calculations, and the solution does not converge with resolution.

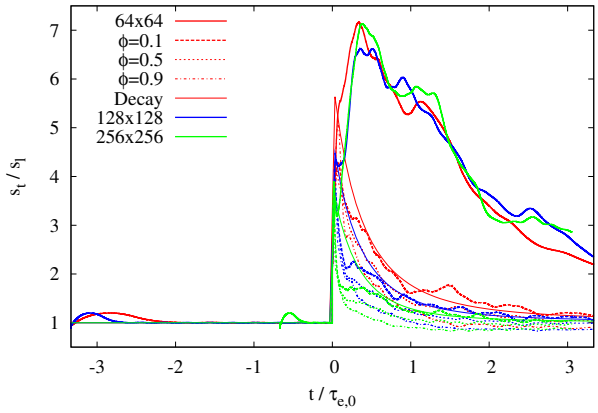

Figure 8. The same as Figure 7, except that the PLFW model is used and convergence with resolution is achieved.

this model assumes CMV, Equation (6):

$$-\langle w\nabla\cdot n\rangle_s \approx s_{\rm l}^0 \left|\langle\nabla\cdot n\rangle_s\right|, \tag{32}$$

which describes the destruction of flame surface density due to the laminar flame propagation. Here, w is the flame front displacement speed, $\left|\langle\nabla\cdot n\rangle_s\right|$ is the mean curvature of the flame, and $s_{\rm l}^0$ is the unstrained laminar flame speed. This approximation assumes that the local front propagation speed of the flame is the unstrained laminar flame speed on average over the flame surface. It is not clear whether the local flame speed in regions of strong positive curvature will average out regions of strong negative curvature especially if cusps are expected to form. Even if cusps do not form, the average local front propagation speed may be better estimated using the resolved curvature of the model flame to estimate the strained laminar flame speed $s_{\rm l}$ instead of the unstrained planar flame speed $s_{\rm l}^0$. Dursi et al. (2003) explored curvature effects relevant for astrophysical flames in the context of SNe Ia and computed Markstein numbers for a range of parameters relevant to Chandrasekhar-mass C/O WDs. Given the local strain rate on the flame surface (that may be computed by future DNS vortex-flame calculations) and the computed Markstein numbers, flame curvature and flame stretch effects may be included in a future version of this TFI model.

While the inverse mean curvature of the flame is prevented from becoming smaller than the laminar flame width artificially, more physical constraints may be constructed by considering flame merging and quenching processes. As the mean curvature increases, higher-order flame surface density destruction terms due to merging may become important (Meneveau & Poinsot 1991). The inclusion of merging and quenching processes into the model may naturally prevent the mean curvature of the flame from becoming too large and will provide a smooth transition from moderate mean curvature to strong mean curvature. Recent calculations by Poludnenko & Oran (2010, 2011) indicate that the transition to "distributed burning" or "broken reaction zones" require higher turbulent intensities than previously thought. This result implies that the flame remains a well-defined concept into the "thin reaction zone" and that model improvements may extend the range of validity to higher-intensity turbulence.

Additionally, the effect of unresolved RT modes should be self-consistently incorporated into the subgrid-scale TFI model. This instability could be incorporated into the energy function $E(k)$ using an appropriate efficiency function with a critical scale being the so-called "fire-polishing" scale $\ell_{\rm fp}$. Ciaraldi-Schoolmann et al. (2009) has shown that the turbulent energy spectrum for $k \parallel g$ follows that expected from Rayleigh-Taylor scaling, while for $k \perp g$ the energy spectrum follows homogeneous and isotropic turbulence. We plan to include the effect of increased flame surface due to RTI in future modeling efforts. Currently, we instead choose the turbulent flame speed based on the dominant effect such that

$$s_{\rm t} = \max\left(s_{\rm TFI}, s_{\rm RTI}\right), \tag{33}$$

where $s_{\rm TFI}$ is the turbulent flame speed estimated from the TFI model described in this work and $s_{\rm RTI}$ is the turbulent flame speed estimated from RTI described in Khokhlov (1995) and Townsley et al. (2007). However, we still prevent $s_{\rm t}$ from increasing beyond the limit $s_{\rm l}^0(1+\Delta/\delta_{\rm l}^0)^\gamma$, which provides a natural quenching process as burning progresses toward lower densities (see Figure 4).

7. CONCLUSIONS

We have implemented a PLFW TFI model based on CVDP and CMV. We calibrated a method used in FLASH to measure the turbulent velocity at the grid scale and have shown its validity over a range of calculations with increasing resolution. We compared and explored different implementation choices relevant for astrophysical flames ultimately deciding that a low-Pr extension of the CMV TFI model is most appropriate for SNe Ia simulation. We provided two convincing test problems of the TFI model in FLASH for laminar and turbulent flows. Of most importance, we have shown that the global turbulent flame speed is consistent with increasing resolution where more of the inertial range is resolved on the computational domain. The combined effects of the subgrid-scale TFI model with the resolved wrinkling of the model flame produce a consistent burning rate independent of resolution. Additionally, we have shown that a laminar flame is recovered in the limiting case of laminar flow.

This model limits the growth of flame surface based on the fact that the inverse mean curvature of the flame should not become smaller than the laminar flame width. This condition was shown to be similar to to arguments that the turbulent flame should quench when $\ell_{\rm G} < \delta_{\rm l}^0$, although derived from DNS calculations of flame–vortex interactions.

Future calculations of SNe Ia will also benefit from the reliable measure of the turbulent intensity on unresolved scales in determining more realistic conditions for DDT. Previous calculations by Townsley et al. (2009); Jackson et al. (2010), and Krueger et al. (2010) determined DDT conditions simply by the requirement that the flame reach a particular density, $\rho_{\rm DDT}$. This condition resulted in detonation ignitions at the "tops" of rising plumes where turbulence is expected to be relatively weak. With a more realistic DDT condition based on u'_Δ, detonations will likely ignite in the turbulent regions underneath plume caps.

The authors thank Alexei Poludnenko and Elaine Oran for useful discussions that contributed to this work. This work was supported by NASA through grant NNX09AD19G. ACC also acknowledges support from the Department of Energy under grant DE-FG02-87ER40317. DMT received support from the Bart J. Bok fellowship at the University of Arizona for part of this work. The authors acknowledge the hospitality of the Kavli Institute for Theoretical Physics, which is supported by the NSF under grant PHY05-51164, during the programs "Accretion and Explosion: the Astrophysics of Degenerate Stars" and "Stellar Death and Supernovae." The software used in this work was in part developed by the DOE-supported ASC/Alliances Center for Astrophysical Thermonuclear Flashes at the University of Chicago. We thank Nathan Hearn for making his QuickFlash analysis tools publicly available at http://quickflash.sourceforge.net. This work was also supported in part by the US Department of Energy, Office of Nuclear Physics, under contract DE-AC02-06CH11357 and utilized resources at the New York Center for Computational Sciences at Stony Brook University/Brookhaven National Laboratory which is supported by the U.S. Department of Energy under Contract No. DE-AC02-98CH10886 and by the State of New York.

REFERENCES

Abdel-Gayed, R. G. & Bradley, D. 1981, Royal Society of London Philosophical Transactions Series A, 301, 1
Badenes, C., Bravo, E., Borkowski, K. J., & Domínguez, I. 2003, ApJ, 593, 358
Bravo, E. & García-Senz, D. 2006, ApJ, 642, L157
Chamulak, D. A., Brown, E. F., & Timmes, F. X. 2007, ApJ, 655, L93
Charlette, F., Meneveau, C., & Veynante, D. 2002, Combust. Flame, 131, 159
Ciaraldi-Schoolmann, F., Schmidt, W., Niemeyer, J. C., Röpke, F. K., & Hillebrandt, W. 2009, ApJ, 696, 1491
Colin, O., Ducros, F., Veynante, D., & Poinsot, T. 2000, Physics of Fluids, 12, 1843
Conley, A., Guy, J., Sullivan, M., Regnault, N., Astier, P., Balland, C., Basa, S., Carlberg, R. G., Fouchez, D., Hardin, D., Hook, I. M., Howell, D. A., Pain, R., Palanque-Delabrouille, N., Perrett, K. M., Pritchet, C. J., Rich, J., Ruhlmann-Kleider, V., Balam, D., Baumont, S., Ellis, R. S., Fabbro, S., Fakhouri, H. K., Fourmanoit, N., González-Gaitán, S., Graham, M. L., Hudson, M. J., Hsiao, E., Kronborg, T., Lidman, C., Mourao, A. M., Neill, J. D., Perlmutter, S., Ripoche, P., Suzuki, N., & Walker, E. S. 2011, ApJS, 192, 1
Dursi, L. J., Zingale, M., Calder, A. C., Fryxell, B., Timmes, F. X., Vladimirova, N., Rosner, R., Caceres, A., Lamb, D. Q., Olson, K., Ricker, P. M., Riley, K., Siegel, A., & Truran, J. W. 2003, ApJ, 595, 955
Filippenko, A. V. 1997, ARA&A, 35, 309
Fisher, R. T., Kadanoff, L. P., Lamb, D. Q., Dubey, A., Plewa, T., Calder, A., Cattaneo, F., Constantin, P., Foster, I., Papka, M. E., Abarzhi, S. I., Asida, S. M., Rich, P. M., Glendening, C. C., Antypas, K., Sheeler, D. J., Reid, L. B., Gallagher, B., & Needham, S. G. 2008, IBM J. Res. Dev., 52, 127
Hillebrandt, W. & Niemeyer, J. C. 2000, ARA&A, 38, 191
Höflich, P. & Khokhlov, A. 1996, ApJ, 457, 500
Iben, Jr., I. & Tutukov, A. V. 1984, ApJS, 54, 335
Jackson, A. P., Calder, A. C., Townsley, D. M., Chamulak, D. A., Brown, E. F., & Timmes, F. X. 2010, ApJ, 720, 99
Kasen, D. 2006, ApJ, 649, 939
Kasen, D. & Woosley, S. E. 2007, ApJ, 656, 661
Kerstein, A. R. 2001, Phys. Rev. E, 64, 066306
Khokhlov, A. M. 1991, A&A, 245, 114
—. 1995, ApJ, 449, 695
Kolmogorov, A. 1941, Akademiia Nauk SSSR Doklady, 30, 301
Krueger, B. K., Jackson, A. P., Townsley, D. M., Calder, A. C., Brown, E. F., & Timmes, F. X. 2010, ApJ, 719, L5
Livne, E. 1990, ApJ, 354, L53
Meneveau, C. & Poinsot, T. 1991, Combust. Flame, 86, 311
Nandkumar, R. & Pethick, C. J. 1984, MNRAS, 209, 511
Niemeyer, J. C. & Kerstein, A. R. 1997, NewA, 2, 239
Nomoto, K. 1982a, ApJ, 257, 780
—. 1982b, ApJ, 253, 798
Nomoto, K., Thielemann, F.-K., & Yokoi, K. 1984, ApJ, 286, 644
Pakmor, R., Hachinger, S., Röpke, F. K., & Hillebrandt, W. 2011, A&A, 528, A117+
Pakmor, R., Kromer, M., Röpke, F. K., Sim, S. A., Ruiter, A. J., & Hillebrandt, W. 2010, Nature, 463, 61
Phillips, M. M. 1993, ApJ, 413, L105
Plewa, T., Calder, A. C., & Lamb, D. Q. 2004, ApJ, 612, L37
Pocheau, A. 1994, Phys. Rev. E, 49, 1109
Poinsot, T. & Veynante, D. 2005, Theoretical and Numerical Combustion, 2nd edn. (Philadelphia, PA: R.T. Edwards, Inc.)
Poludnenko, A. & Oran, E. 2010, Combust. Flame, 157, 995
—. 2011, Combust. Flame, 158, 301
Röpke, F. K. 2006, in Reviews in Modern Astronomy, Vol. 19, Reviews in Modern Astronomy, ed. S. Roeser, 127
Röpke, F. K., Hillebrandt, W., Schmidt, W., Niemeyer, J. C., Blinnikov, S. I., & Mazzali, P. A. 2007, ApJ, 668, 1132
Saio, H. & Nomoto, K. 1985, A&A, 150, L21
—. 1998, ApJ, 500, 388
—. 2004, ApJ, 615, 444
Schmidt, W., Niemeyer, J. C., & Hillebrandt, W. 2006a, A&A, 450, 265
Schmidt, W., Niemeyer, J. C., Hillebrandt, W., & Röpke, F. K. 2006b, A&A, 450, 283
Sytine, I. V., Porter, D. H., Woodward, P. R., Hodson, S. W., & Winkler, K.-H. 2000, J. of Comput. Phys., 158, 225
Timmes, F. X. & Woosley, S. E. 1992, ApJ, 396, 649
Townsley, D. M., Asida, S., Jena, T., & Lamb, D. Q. 2008, in preparation
Townsley, D. M., Calder, A. C., Asida, S. M., Seitenzahl, I. R., Peng, F., Vladimirova, N., Lamb, D. Q., & Truran, J. W. 2007, ApJ, 668, 1118
Townsley, D. M., Jackson, A. P., Calder, A. C., Chamulak, D. A., Brown, E. F., & Timmes, F. X. 2009, ApJ, 701, 1582
Vladimirova, N., Weirs, G., & Ryzhik, L. 2006, Combust. Theory Modelling, 10, 727
Webbink, R. F. 1984, ApJ, 277, 355
Whelan, J. & Iben, Jr., I. 1973, ApJ, 186, 1007
Woosley, S. E., Almgren, A., Bell, J. B., Glatzmaier, G., Kasen, D., Kerstein, A. R., Ma, H., Nugent, P., Röpke, F., Sankaran, V., & Zingale, M. 2007a, Journal of Physics Conference Series, 78, 012081
Woosley, S. E., Kasen, D., Blinnikov, S., & Sorokina, E. 2007b, ApJ, 662, 487
Woosley, S. E., Kerstein, A. R., Sankaran, V., Aspden, A. J., & Röpke, F. K. 2009, ApJ, 704, 255
Yeung, P., Girimaji, S., & Pope, S. 1990, Combust. Flame, 79, 340
Yoon, S.-C., Podsiadlowski, P., & Rosswog, S. 2007, MNRAS, 380, 933
Zingale, M., Almgren, A. S., Bell, J. B., Nonaka, A., & Woosley, S. E. 2009, ApJ, 704, 196
Zingale, M., Niemeyer, J. C., Timmes, F. X., Dursi, L. J., Calder, A. C., Fryxell, B., Lamb, D. Q., MacNeice, P., Olson, K., Ricker, P. M., Rosner, R., Truran, J. W., & Tufo, H. M. 2001, in American Institute of Physics Conference Series, Vol. 586, 20th Texas Symposium on relativistic astrophysics, ed. J. C. Wheeler & H. Martel, 490–492

Chapter 5

Conclusion

The research conducted for this dissertation has provided useful insight into the explosion mechanism of SNe Ia. Motivated by the desire to reduce systematic uncertainties in correlations between SN observables, a framework for studying systematic effects was utilized to explore the influence of the DDT density on the average yield of radioactive ^{56}Ni that powers the light curve. I showed that the choice of transition density influences both the average peak brightness and the magnitude of the dispersion in the sample population of events. A lower transition density allows more time to be spent during the nonlinear evolution of the deflagration phase, allowing both a larger dispersion and lower average yield of ^{56}Ni. The dependence of the dispersion of the sample population on metallicity is an important contribution to SNe Ia theory. The framework developed in Townsley et al. [99] has enabled this kind of study for the first time. Observations have identified that the dispersion in brightness is much larger in younger stellar populations than older [see, *e. g.*, 35], which may be a property that can be demonstrated in future investigations.

While this study demonstrates a robust result with respect to the dependence of the average brightness on transition density, a further study is warranted to explore the dependence of the variance on transition density. The behavior that the variance increases with decreasing transition density may be due in part to the axial symmetry constraint of the 2D simulation. 3D simulations will alleviate this symmetry constraint.

While the ignition conditions were motivated only by the requirement to obtain a sample population of events with the observed distribution of peak brightnesses, the distribution clearly depends on some combination of ignition conditions and transition density. With the development of an accurate measure of SGS turbulent intensity, new, more physically motivated, DDT criterion should be determined dynamically from local conditions including density, temperature, composition, and turbulence. While some aspects of the DDT will still need to be assumed, the criteria themselves will not be met so regularly as in Chapter 3, possibly allowing for additional dispersion in the explosion outcome. The range of ignition conditions considered in the statistical framework will need to be re-calibrated to reproduce the observed range of SN, but future systematic studies performed will be subject to variations in both the ignition conditions and DDT conditions in a self-consistent way.

The development and implementation of a TFI model for astrophysical flames provides a key ingredient necessary to address both the early flame evolution and the DDT. This model enables SNe Ia to be simulated with the inclusion of a realistic convective velocity

field expected from pre-ignition ^{12}C burning [69]. The TFI model allows the initial hot spots to respond realistically to the pre-existing turbulence. Results expected from these calculations will allow an unprecedented understanding of the intrinsic variation in the explosion outcome and may be used to calibrate parameterized ignition conditions, such as Equation (2.12). The contribution of the observed dispersion in explosion outcomes due to variations in ignition conditions may be more readily quantifiable, particularly if the DDT is determined dynamically based on local conditions.

Understanding how the dispersion in the peak brightness of SNe Ia depends on the properties of the progenitor WD is important for determining whether the observed scatter in SN light curves is intrinsic to the event or extrinsic due to uncorrected effects such as dust extinction or metallicity. The identification of uncorrected systematic effects will reduce the overall uncertainty in the equation of state parameter of dark energy, which is needed to discriminate between different cosmological models. This process has already started from an empirical basis [see, *e. g.*, 184], but a physical understanding of these systematic effects must be realized. Observations have indicated that metallicity, mean stellar age, and dust play are the most probable "secondary" parameters to the Phillips relation. I have taken the approach to understand systematic effects on the primary parameter (Δm_{15}) first to determine whether the dispersion about the Phillips relation is due to a secondary parameter or higher-order terms of Δm_{15}.

Future works will explore the influence of the core ^{12}C to ^{16}O ratio on the explosion outcome, as this property of the pre-ignition WD is influenced by both the metallicity and mean age of the parent stellar population. In addition, I plan to revisit some calculations performed in 2D. In particular, I will investigate the dispersion in explosion brightness due to variations in the DDT criterion with 3D simulations and improved estimates of DDT conditions. In addition, improvements will continue to be made to the TFI model to account for non-isotropic, inhomogeneous turbulence. In future iterations of the TFI model, I also hope to account for unresolved RT growth modes.

While the model development and systematic studies performed for this thesis dissertation are important contributions in their own right, they have opened the door to a new round of state-of-the-art 3D simulations that promise to provide unprecedented realism and physical insight into the explosion mechanism of SNe Ia.

Bibliography

[1] J. C. Wheeler, R. P. Harkness. Type I supernovae. *Reports on Progress in Physics*, 53:1467–1557 (1990).

[2] M. M. Phillips. The absolute magnitudes of type Ia supernovae. *ApJ*, 413:L105 (1993).

[3] A. G. Riess, A. V. Filippenko, P. Challis, A. Clocchiatti, A. Diercks, P. M. Garnavich, R. L. Gilliland, C. J. Hogan, S. Jha, R. P. Kirshner, B. Leibundgut, M. M. Phillips, D. Reiss, B. P. Schmidt, R. A. Schommer, R. C. Smith, J. Spyromilio, C. Stubbs, N. B. Suntzeff, J. Tonry. Observational evidence from supernovae for an accelerating universe and a cosmological constant. *AJ*, 116:1009 (1998).

[4] S. Perlmutter, G. Aldering, G. Goldhaber, R. A. Knop, P. Nugent, P. G. Castro, S. Deustua, S. Fabbro, A. Goobar, D. E. Groom, I. M. Hook, A. G. Kim, M. Y. Kim, J. C. Lee, N. J. Nunes, R. Pain, C. R. Pennypacker, R. Quimby, C. Lidman, R. S. Ellis, M. Irwin, R. G. McMahon, P. Ruiz-Lapuente, N. Walton, B. Schaefer, B. J. Boyle, A. V. Filippenko, T. Matheson, A. S. Fruchter, N. Panagia, H. J. M. Newberg, W. J. Couch, The Supernova Cosmology Project. Measurements of Omega and Lambda from 42 high-redshift supernovae. *ApJ*, 517:565 (1999).

[5] M. Hamuy, M. M. Phillips, N. B. Suntzeff, R. A. Schommer, J. Maza, R. Aviles. The Absolute Luminosities of the Calan/Tololo Type IA Supernovae. *AJ*, 112:2391–+ (1996).

[6] A. Conley, J. Guy, M. Sullivan, N. Regnault, P. Astier, C. Balland, S. Basa, R. G. Carlberg, D. Fouchez, D. Hardin, I. M. Hook, D. A. Howell, R. Pain, N. Palanque-Delabrouille, K. M. Perrett, C. J. Pritchet, J. Rich, V. Ruhlmann-Kleider, D. Balam, S. Baumont, R. S. Ellis, S. Fabbro, H. K. Fakhouri, N. Fourmanoit, S. González-Gaitán, M. L. Graham, M. J. Hudson, E. Hsiao, T. Kronborg, C. Lidman, A. M. Mourao, J. D. Neill, S. Perlmutter, P. Ripoche, N. Suzuki, E. S. Walker. Supernova Constraints and Systematic Uncertainties from the First Three Years of the Supernova Legacy Survey. *ApJS*, 192:1–+ (2011).

[7] F. Hoyle, W. A. Fowler. Nucleosynthesis in Supernovae. *ApJ*, 132:565–+ (1960).

[8] J. W. Truran, W. D. Arnett, A. G. W. Cameron. Nucleosynthesis in supernova shock waves. *Canadian Journal of Physics*, 45:2315–+ (1967).

[9] S. A. Colgate, C. McKee. Early Supernova Luminosity. *ApJ*, 157:623–+ (1969).

[10] W. D. Arnett. Type I supernovae. I - analytic solutions for the early part of the light curve. *ApJ*, 253:785 (1982).

[11] P. A. Pinto, R. G. Eastman. The Physics of Type IA Supernova Light Curves. I. Analytic Results and Time Dependence. *ApJ*, 530:744–756 (2000).

[12] S. E. Woosley, D. Kasen, S. Blinnikov, E. Sorokina. Type Ia Supernova Light Curves. *ApJ*, 662:487–503 (2007).

[13] D. Kasen, S. E. Woosley. On the Origin of the Type Ia Supernova Width-Luminosity Relation. *ApJ*, 656:661–665 (2007).

[14] D. Branch, G. A. Tammann. Type IA supernovae as standard candles. *ARA&A*, 30:359–389 (1992).

[15] M. Hamuy, M. M. Phillips, J. Maza, N. B. Suntzeff, R. A. Schommer, R. Aviles. A Hubble diagram of distant type IA supernovae. *AJ*, 109:1–13 (1995).

[16] R. Tripp. A two-parameter luminosity correction for Type IA supernovae. *A&A*, 331:815–820 (1998).

[17] W. D. Li, Y. L. Qiu, Q. Y. Qiao, J. Ma, J. Y. Hu, L. Wang, J. C. Wheeler. Supernova 1996W in NGC 4027. *IAU Circ.*, 6379:1 (1996).

[18] W. Li, A. V. Filippenko, R. R. Treffers, A. G. Riess, J. Hu, Y. Qiu. A High Intrinsic Peculiarity Rate among Type IA Supernovae. *ApJ*, 546:734–743 (2001).

[19] R. R. Treffers, C. Y. Peng, A. V. Filippenko, M. W. Richmond, A. J. Barth, A. M. Gilbert. Supernova 1997bs in NGC 3627. *IAU Circ.*, 6627:1 (1997).

[20] P. Astier, J. Guy, N. Regnault, R. Pain, E. Aubourg, D. Balam, S. Basa, R. G. Carlberg, S. Fabbro, D. Fouchez, I. M. Hook, D. A. Howell, H. Lafoux, J. D. Neill, N. Palanque-Delabrouille, K. Perrett, C. J. Pritchet, J. Rich, M. Sullivan, R. Taillet, G. Aldering, P. Antilogus, V. Arsenijevic, C. Balland, S. Baumont, J. Bronder, H. Courtois, R. S. Ellis, M. Filiol, A. C. Gonçalves, A. Goobar, D. Guide, D. Hardin, V. Lusset, C. Lidman, R. McMahon, M. Mouchet, A. Mourao, S. Perlmutter, P. Ripoche, C. Tao, N. Walton. The Supernova Legacy Survey: measurement of $\Omega_{\rm M}$, Ω and w from the first year data set. *A&A*, 447:31–48 (2006).

[21] M. Hamuy, G. Folatelli, N. I. Morrell, M. M. Phillips, N. B. Suntzeff, S. E. Persson, M. Roth, S. Gonzalez, W. Krzeminski, C. Contreras, W. L. Freedman, D. C. Murphy, B. F. Madore, P. Wyatt, J. Maza, A. V. Filippenko, W. Li, P. A. Pinto. The Carnegie Supernova Project: The Low-Redshift Survey. *PASP*, 118:2–20 (2006).

[22] Y. Copin, N. Blanc, S. Bongard, E. Gangler, L. Saugé, G. Smadja, P. Antilogus, G. Garavini, S. Gilles, R. Pain, G. Aldering, S. Bailey, B. C. Lee, S. Loken, P. Nugent, S. Perlmutter, R. Scalzo, R. C. Thomas, L. Wang, B. A. Weaver, E. Pécontal, R. Kessler, C. Baltay, D. Rabinowitz, A. Bauer. The Nearby Supernova Factory. *New Astronomy Review*, 50:436–438 (2006).

[23] S. C. Keller, B. P. Schmidt, M. S. Bessell, P. G. Conroy, P. Francis, A. Granlund, E. Kowald, A. P. Oates, T. Martin-Jones, T. Preston, P. Tisserand, A. Vaccarella, M. F. Waterson. The SkyMapper Telescope and The Southern Sky Survey. *PASA*, 24:1–12 (2007).

[24] W. M. Wood-Vasey, G. Miknaitis, C. W. Stubbs, S. Jha, A. G. Riess, P. M. Garnavich, R. P. Kirshner, C. Aguilera, A. C. Becker, J. W. Blackman, S. Blondin, P. Challis, A. Clocchiatti, A. Conley, R. Covarrubias, T. M. Davis, A. V. Filippenko, R. J. Foley, A. Garg, M. Hicken, K. Krisciunas, B. Leibundgut, W. Li, T. Matheson, A. Miceli, G. Narayan, G. Pignata, J. L. Prieto, A. Rest, M. E. Salvo, B. P. Schmidt, R. C. Smith, J. Sollerman, J. Spyromilio, J. L. Tonry, N. B. Suntzeff, A. Zenteno. Observational Constraints on the Nature of Dark Energy: First Cosmological Results from the ESSENCE Supernova Survey. *ApJ*, 666:694–715 (2007).

[25] M. T. Botticella, M. Riello, E. Cappellaro, S. Benetti, G. Altavilla, A. Pastorello, M. Turatto, L. Greggio, F. Patat, S. Valenti, L. Zampieri, A. Harutyunyan, G. Pignata, S. Taubenberger. Supernova rates from the Southern inTermediate Redshift ESO Supernova Search (STRESS). *A&A*, 479:49–66 (2008).

[26] J. A. Holtzman, J. Marriner, R. Kessler, M. Sako, B. Dilday, J. A. Frieman, D. P. Schneider, B. Bassett, A. Becker, D. Cinabro, F. DeJongh, D. L. Depoy, M. Doi, P. M. Garnavich, C. J. Hogan, S. Jha, K. Konishi, H. Lampeitl, J. L. Marshall, D. McGinnis, G. Miknaitis, R. C. Nichol, J. L. Prieto, A. G. Riess, M. W. Richmond, R. Romani, M. Smith, N. Takanashi, K. Tokita, K. van der Heyden, N. Yasuda, C. Zheng. The Sloan Digital Sky Survey-II Photometry and Supernova IA Light Curves from the 2005 Data. *AJ*, 136:2306–2320 (2008).

[27] H. Furusawa, G. Kosugi, M. Akiyama, T. Takata, K. Sekiguchi, I. Tanaka, I. Iwata, M. Kajisawa, N. Yasuda, M. Doi, M. Ouchi, C. Simpson, K. Shimasaku, T. Yamada, J. Furusawa, T. Morokuma, C. M. Ishida, K. Aoki, T. Fuse, M. Imanishi, M. Iye, H. Karoji, N. Kobayashi, T. Kodama, Y. Komiyama, Y. Maeda, S. Miyazaki, Y. Mizumoto, F. Nakata, J. Noumaru, R. Ogasawara, S. Okamura, T. Saito, T. Sasaki, Y. Ueda, M. Yoshida. The Subaru/XMM-Newton Deep Survey (SXDS). II. Optical Imaging and Photometric Catalogs. *ApJS*, 176:1–18 (2008).

[28] T. Totani, T. Morokuma, T. Oda, M. Doi, N. Yasuda. Delay Time Distribution Measurement of Type Ia Supernovae by the Subaru/XMM-Newton Deep Survey and Implications for the Progenitor. *PASJ*, 60:1327– (2008).

[29] S. G. Djorgovski, C. Baltay, A. A. Mahabal, A. J. Drake, R. Williams, D. Rabinowitz, M. J. Graham, C. Donalek, E. Glikman, A. Bauer, R. Scalzo, N. Ellman. The Palomar-Quest digital synoptic sky survey. *Astronomische Nachrichten*, 329:263 (2008).

[30] M. Hicken, P. Challis, S. Jha, R. P. Kirshner, T. Matheson, M. Modjaz, A. Rest, W. Michael Wood-Vasey, G. Bakos, E. J. Barton, P. Berlind, A. Bragg, C. Briceño, W. R. Brown, N. Caldwell, M. Calkins, R. Cho, L. Ciupik, M. Contreras, K.-C.

Dendy, A. Dosaj, N. Durham, K. Eriksen, G. Esquerdo, M. Everett, E. Falco, J. Fernandez, A. Gaba, P. Garnavich, G. Graves, P. Green, T. Groner, C. Hergenrother, M. J. Holman, V. Hradecky, J. Huchra, B. Hutchison, D. Jerius, A. Jordan, R. Kilgard, M. Krauss, K. Luhman, L. Macri, D. Marrone, J. McDowell, D. McIntosh, B. McNamara, T. Megeath, B. Mochejska, D. Munoz, J. Muzerolle, O. Naranjo, G. Narayan, M. Pahre, W. Peters, D. Peterson, K. Rines, B. Ripman, A. Roussanova, R. Schild, A. Sicilia-Aguilar, J. Sokoloski, K. Smalley, A. Smith, T. Spahr, K. Z. Stanek, P. Barmby, S. Blondin, C. W. Stubbs, A. Szentgyorgyi, M. A. P. Torres, A. Vaz, A. Vikhlinin, Z. Wang, M. Westover, D. Woods, P. Zhao. CfA3: 185 Type Ia Supernova Light Curves from the CfA. *ApJ*, 700:331–357 (2009).

[31] A. J. Drake, S. G. Djorgovski, A. Mahabal, E. Beshore, S. Larson, M. J. Graham, R. Williams, E. Christensen, M. Catelan, A. Boattini, A. Gibbs, R. Hill, R. Kowalski. First Results from the Catalina Real-Time Transient Survey. *ApJ*, 696:870–884 (2009).

[32] S. Kulkarni, N. Law, M. Kasliwal, R. Quimby, E. Ofek, P. Nugent, I. Arcavi, L. Bildsten, J. Bloom, J. Brewer, T. Brown, S. B. Cenko, D. Ciardi, E. Croner, R. Dekany, G. Djorgovski, A. V. Filippenko, D. Fox, A. Gal-Yam, C. Grillmair, D. Hale, N. Hamam, D. Helfand, G. Helou, I. Hook, A. Howell, J. Jacobsen, M. Kiewe, R. Laher, A. Mahabal, S. Mattingly, J. Patterson, H. Perets, S. Perlmutter, A. Pickles, D. Poznanski, A. Rau, G. Rahmer, W. Reach, W. Rosing, M. Shara, R. Smith, D. Starr, M. Sullivan, J. Surace, R. Thomas, V. Velur. Supernova Discovery from the Palomar Transient Factory. *The Astronomer's Telegram*, 1964:1 (2009).

[33] D. A. Howell, A. Conley, M. Della Valle, P. E. Nugent, S. Perlmutter, G. H. Marion, K. Krisciunas, C. Badenes, P. Mazzali, G. Aldering, P. Antilogus, E. Baron, A. Becker, C. Baltay, S. Benetti, S. Blondin, D. Branch, E. F. Brown, S. Deustua, A. Ealet, R. S. Ellis, D. Fouchez, W. Freedman, A. Gal-Yam, S. Jha, D. Kasen, R. Kessler, A. G. Kim, D. C. Leonard, W. Li, M. Livio, D. Maoz, F. Mannucci, T. Matheson, J. D. Neill, K. Nomoto, N. Panagia, K. Perrett, M. Phillips, D. Poznanski, R. Quimby, A. Rest, A. Riess, M. Sako, A. M. Soderberg, L. Strolger, R. Thomas, M. Turatto, S. van Dyk, W. M. Wood-Vasey. Type Ia supernova science 2010-2020. *ArXiv e-prints* (2009). 0903.1086.

[34] E. Scannapieco, L. Bildsten. The Type Ia Supernova Rate. *ApJ*, 629:L85–L88 (2005).

[35] F. Mannucci, M. Della Valle, N. Panagia. Two populations of progenitors for Type Ia supernovae? *MNRAS*, 370:773–783 (2006).

[36] D. A. Howell, M. Sullivan, A. Conley, R. Carlberg. Predicted and observed evolution in the mean properties of Type Ia supernovae with redshift. *ApJ*, 667:L37 (2007).

[37] J. S. Gallagher, P. M. Garnavich, N. Caldwell, R. P. Kirshner, S. W. Jha, W. Li, M. Ganeshalingam, A. V. Filippenko. Supernovae in Early-Type Galaxies: Directly Connecting Age and Metallicity with Type Ia Luminosity. *ApJ*, 685:752–766 (2008).

[38] C. A. Tremonti, T. M. Heckman, G. Kauffmann, J. Brinchmann, S. Charlot, S. D. M. White, M. Seibert, E. W. Peng, D. J. Schlegel, A. Uomoto, M. Fukugita, J. Brinkmann.

The Origin of the Mass-Metallicity Relation: Insights from 53,000 Star-forming Galaxies in the Sloan Digital Sky Survey. *ApJ*, 613:898–913 (2004).

[39] E. Bravo, C. Badenes. Is the metallicity of their host galaxies a good measure of the metallicity of Type Ia supernovae? *MNRAS*, pp. 464–+ (2011).

[40] P. Höflich, K. Krisciunas, A. M. Khokhlov, E. Baron, G. Folatelli, M. Hamuy, M. M. Phillips, N. Suntzeff, L. Wang, NSF07-SNIa Collaboration. Secondary Parameters of Type Ia Supernova Light Curves. *ApJ*, 710:444–455 (2010).

[41] P. Ruiz-Lapuente, D. J. Jeffery, P. M. Challis, A. V. Filippenko, R. P. Kirshner, L. C. Ho, B. P. Schmidt, F. Sánchez, R. Canal. A possible low-mass type Ia supernova. *Nature*, 365:728–730 (1993).

[42] A. V. Filippenko, M. W. Richmond, T. Matheson, J. C. Shields, E. M. Burbidge, R. D. Cohen, M. Dickinson, M. A. Malkan, B. Nelson, J. Pietz, D. Schlegel, P. Schmeer, H. Spinrad, C. C. Steidel, H. D. Tran, W. Wren. The peculiar Type IA SN 1991T - Detonation of a white dwarf? *ApJ*, 384:L15–L18 (1992).

[43] W. Li, A. V. Filippenko, R. Chornock, E. Berger, P. Berlind, M. L. Calkins, P. Challis, C. Fassnacht, S. Jha, R. P. Kirshner, T. Matheson, W. L. W. Sargent, R. A. Simcoe, G. H. Smith, G. Squires. SN 2002cx: The Most Peculiar Known Type Ia Supernova. *PASP*, 115:453–473 (2003).

[44] R. A. Scalzo, G. Aldering, P. Antilogus, C. Aragon, S. Bailey, C. Baltay, S. Bongard, C. Buton, M. Childress, N. Chotard, Y. Copin, H. K. Fakhouri, A. Gal-Yam, E. Gangler, S. Hoyer, M. Kasliwal, S. Loken, P. Nugent, R. Pain, E. Pécontal, R. Pereira, S. Perlmutter, D. Rabinowitz, A. Rau, G. Rigaudier, K. Runge, G. Smadja, C. Tao, R. C. Thomas, B. Weaver, C. Wu. Nearby Supernova Factory Observations of SN 2007if: First Total Mass Measurement of a Super-Chandrasekhar-Mass Progenitor. *ApJ*, 713:1073–1094 (2010).

[45] J. Whelan, I. Iben, Jr. Binaries and Supernovae of Type I. *ApJ*, 186:1007–1014 (1973).

[46] K. Nomoto. Accreting white dwarf models for type I supernovae. I - Presupernova evolution and triggering mechanisms. *ApJ*, 253:798–810 (1982).

[47] I. Iben, Jr., A. V. Tutukov. Supernovae of type I as end products of the evolution of binaries with components of moderate initial mass (M not greater than about 9 solar masses). *ApJS*, 54:335–372 (1984).

[48] R. F. Webbink. Double white dwarfs as progenitors of R Coronae Borealis stars and Type I supernovae. *ApJ*, 277:355–360 (1984).

[49] S. Rosswog, D. Kasen, J. Guillochon, E. Ramirez-Ruiz. Collisions of White Dwarfs as a New Progenitor Channel for Type Ia Supernovae. *ApJ*, 705:L128–L132 (2009).

[50] D. M. Townsley, L. Bildsten. Theoretical Modeling of the Thermal State of Accreting White Dwarfs Undergoing Classical Nova Cycles. *ApJ*, 600:390–403 (2004).

[51] K. J. Shen, D. Kasen, N. N. Weinberg, L. Bildsten, E. Scannapieco. Thermonuclear .Ia Supernovae from Helium Shell Detonations: Explosion Models and Observables. *ApJ*, 715:767–774 (2010).

[52] E. Livne. Successive detonations in accreting white dwarfs as an alternative mechanism for type I supernovae. *ApJ*, 354:L53–L55 (1990).

[53] K. Nomoto, I. Iben, Jr. Carbon ignition in a rapidly accreting degenerate dwarf - A clue to the nature of the merging process in close binaries. *ApJ*, 297:531–537 (1985).

[54] H. Saio, K. Nomoto. Evolution of a merging pair of C + O white dwarfs to form a single neutron star. *A&A*, 150:L21–L23 (1985).

[55] M. Hicken, P. M. Garnavich, J. L. Prieto, S. Blondin, D. L. DePoy, R. P. Kirshner, J. Parrent. The Luminous and Carbon-rich Supernova 2006gz: A Double Degenerate Merger? *ApJ*, 669:L17–L20 (2007).

[56] M. Yamanaka, K. S. Kawabata, K. Kinugasa, M. Tanaka, A. Imada, K. Maeda, K. Nomoto, A. Arai, S. Chiyonobu, Y. Fukazawa, O. Hashimoto, S. Honda, Y. Ikejiri, R. Itoh, Y. Kamata, N. Kawai, T. Komatsu, K. Konishi, D. Kuroda, H. Miyamoto, S. Miyazaki, O. Nagae, H. Nakaya, T. Ohsugi, T. Omodaka, N. Sakai, M. Sasada, M. Suzuki, H. Taguchi, H. Takahashi, H. Tanaka, M. Uemura, T. Yamashita, K. Yanagisawa, M. Yoshida. Early Phase Observations of Extremely Luminous Type Ia Supernova 2009dc. *ApJ*, 707:L118–L122 (2009).

[57] K. Maeda, K. Kawabata, W. Li, M. Tanaka, P. A. Mazzali, T. Hattori, K. Nomoto, A. V. Filippenko. Subaru and Keck Observations of the Peculiar Type Ia Supernova 2006GZ at Late Phases. *ApJ*, 690:1745–1752 (2009).

[58] M. Tanaka, K. S. Kawabata, M. Yamanaka, K. Maeda, T. Hattori, K. Aoki, K. Nomoto, M. Iye, T. Sasaki, P. A. Mazzali, E. Pian. Spectropolarimetry of Extremely Luminous Type Ia Supernova 2009dc: Nearly Spherical Explosion of Super-Chandrasekhar Mass White Dwarf. *ApJ*, 714:1209–1216 (2010).

[59] S. Taubenberger, S. Benetti, M. Childress, R. Pakmor, S. Hachinger, P. A. Mazzali, V. Stanishev, N. Elias-Rosa, I. Agnoletto, F. Bufano, M. Ergon, A. Harutyunyan, C. Inserra, E. Kankare, M. Kromer, H. Navasardyan, J. Nicolas, A. Pastorello, E. Prosperi, F. Salgado, J. Sollerman, M. Stritzinger, M. Turatto, S. Valenti, W. Hillebrandt. High luminosity, slow ejecta and persistent carbon lines: SN 2009dc challenges thermonuclear explosion scenarios. *MNRAS*, 412:2735–2762 (2011).

[60] J. M. Silverman, M. Ganeshalingam, W. Li, A. V. Filippenko, A. A. Miller, D. Poznanski. Fourteen months of observations of the possible super-Chandrasekhar mass Type Ia Supernova 2009dc. *MNRAS*, 410:585–611 (2011).

[61] M. Childress, G. Aldering, C. Aragon, P. Antilogus, S. Bailey, C. Baltay, S. Bongard, C. Buton, A. Canto, N. Chotard, Y. Copin, H. K. Fakhouri, E. Gangler, M. Kerschhaggl, M. Kowalski, E. Y. Hsiao, S. Loken, P. Nugent, K. Paech, R. Pain, E. Pecontal, R. Pereira, S. Perlmutter, D. Rabinowitz, K. Runge, R. Scalzo, R. C. Thomas,

G. Smadja, C. Tao, B. A. Weaver, C. Wu. Keck Observations of the Young Metal-poor Host Galaxy of the Super-Chandrasekhar-mass Type Ia Supernova SN 2007if. *ApJ*, 733:3–+ (2011).

[62] H. Saio, K. Nomoto. Inward Propagation of Nuclear-burning Shells in Merging C-O and He White Dwarfs. *ApJ*, 500:388 (1998).

[63] H. Saio, K. Nomoto. Off-Center Carbon Ignition in Rapidly Rotating, Accreting Carbon-Oxygen White Dwarfs. *ApJ*, 615:444–449 (2004).

[64] R. Pakmor, M. Kromer, F. K. Röpke, S. A. Sim, A. J. Ruiter, W. Hillebrandt. Subluminous type Ia supernovae from the mergers of equal-mass white dwarfs with mass $\sim 0.9 M_{solar}$. *Nature*, 463:61–64 (2010).

[65] R. Pakmor, S. Hachinger, F. K. Röpke, W. Hillebrandt. Violent mergers of nearly equal-mass white dwarf as progenitors of subluminous Type Ia supernovae. *A&A*, 528:A117+ (2011).

[66] S.-C. Yoon, P. Podsiadlowski, S. Rosswog. Remnant evolution after a carbon-oxygen white dwarf merger. *MNRAS*, 380:933–948 (2007).

[67] W.-M. Liu, W.-C. Chen, B. Wang, Z. W. Han. Helium-star evolutionary channel to super-Chandrasekhar mass type Ia supernovae. *A&A*, 523:A3+ (2010).

[68] S. E. Woosley, A. Almgren, J. B. Bell, G. Glatzmaier, D. Kasen, A. R. Kerstein, H. Ma, P. Nugent, F. Röpke, V. Sankaran, M. Zingale. Type Ia supernovae. *Journal of Physics Conference Series*, 78(1):012081–+ (2007).

[69] M. Zingale, A. S. Almgren, J. B. Bell, A. Nonaka, S. E. Woosley. Low Mach Number Modeling of Type IA Supernovae. IV. White Dwarf Convection. *ApJ*, 704:196–210 (2009).

[70] W. D. Arnett. A Possible Model of Supernovae: Detonation of 12C. *Ap&SS*, 5:180–212 (1969).

[71] C. J. Hansen, J. C. Wheeler. A Calculation of a White Dwarf Supernova. *Ap&SS*, 3:464–474 (1969).

[72] K. Nomoto, D. Sugimoto, S. Neo. Carbon deflagration supernova, an alternative to carbon detonation. *Ap&SS*, 39:L37–L42 (1976).

[73] A. M. Khokhlov. Delayed detonation model for type IA supernovae. *A&A*, 245:114–128 (1991).

[74] K. Nomoto. Accreting white dwarf models for type 1 supernovae. II - Off-center detonation supernovae. *ApJ*, 257:780–792 (1982).

[75] K. Nomoto, F.-K. Thielemann, K. Yokoi. Accreting white dwarf models of Type I supernovae. III - Carbon deflagration supernovae. *ApJ*, 286:644–658 (1984).

[76] A. M. Khokhlov. Mechanisms for the initiation of detonations in the degenerate matter of supernovae. *A&A*, 246:383–396 (1991).

[77] P. Höflich, A. Khokhlov. Explosion Models for Type IA Supernovae: A Comparison with Observed Light Curves, Distances, H 0, and Q 0. *ApJ*, 457:500–+ (1996).

[78] J. C. Niemeyer, W. Hillebrandt, S. E. Woosley. Off-Center Deflagrations in Chandrasekhar Mass Type IA Supernova Models. *ApJ*, 471:903 (1996).

[79] A. C. Calder, T. Plewa, N. Vladimirova, D. Q. Lamb, J. W. Truran. Type Ia Supernovae: An Asymmetric Deflagration Model. *ArXiv Astrophysics e-prints* (2004).

[80] E. Livne, S. M. Asida, P. Höflich. On the Sensitivity of Deflagrations in a Chandrasekhar Mass White Dwarf to Initial Conditions. *ApJ*, 632:443–449 (2005).

[81] I. Golombek, J. C. Niemeyer. A model for multidimensional delayed detonations in SN Ia explosions. *A&A*, 438:611–616 (2005).

[82] V. N. Gamezo, A. M. Khokhlov, E. S. Oran. Three-dimensional delayed-detonation model of type Ia supernovae. *ApJ*, 623:337–346 (2005).

[83] F. K. Röpke, J. C. Niemeyer. Delayed detonations in full-star models of type Ia supernova explosions. *A&A*, 464:683–686 (2007).

[84] E. Bravo, D. García-Senz. A three-dimensional picture of the delayed-detonation model of type Ia supernovae. *A&A*, 478:843–853 (2008).

[85] F. K. Röpke, W. Hillebrandt, W. Schmidt, J. C. Niemeyer, S. I. Blinnikov, P. A. Mazzali. A Three-Dimensional Deflagration Model for Type Ia Supernovae Compared with Observations. *ApJ*, 668:1132–1139 (2007).

[86] T. Plewa, A. C. Calder, D. Q. Lamb. Type Ia Supernova Explosion: Gravitationally Confined Detonation. *ApJ*, 612:L37–L40 (2004).

[87] E. Bravo, D. García-Senz. Beyond the Bubble Catastrophe of Type Ia Supernovae: Pulsating Reverse Detonation Models. *ApJ*, 642:L157–L160 (2006).

[88] C. Badenes, E. Bravo, K. J. Borkowski, I. Domínguez. Thermal X-Ray Emission from Shocked Ejecta in Type Ia Supernova Remnants: Prospects for Explosion Mechanism Identification. *ApJ*, 593:358–369 (2003).

[89] P. A. Pinto, R. G. Eastman. The Physics of Type IA Supernova Light Curves. II. Opacity and Diffusion. *ApJ*, 530:757–776 (2000).

[90] D. Kasen. Secondary Maximum in the Near-Infrared Light Curves of Type Ia Supernovae. *ApJ*, 649:939–953 (2006).

[91] P. A. Mazzali, F. K. Röpke, S. Benetti, W. Hillebrandt. A common explosion mechanism for type Ia supernovae. *Science*, 315:825 (2007).

[92] D. Kasen. Seeing the Collision of a Supernova with Its Companion Star. *ApJ*, 708:1025–1031 (2010).

[93] L. Greggio. The rates of type Ia supernovae - II. Diversity of events at low and high redshifts. *MNRAS*, 406:22–42 (2010).

[94] B. K. Krueger, A. P. Jackson, D. M. Townsley, A. C. Calder, E. F. Brown, F. X. Timmes. On Variations of the Brightness of Type Ia Supernovae with the Age of the Host Stellar Population. *ApJ*, 719:L5–L9 (2010).

[95] P. Höflich, J. C. Wheeler, F. K. Thielemann. Type Ia supernovae: Influence of the initial composition on the nucleosynthesis, light curves, and spectra and consequences for the determination of Omega M and Lambda. *ApJ*, 495:617 (1998).

[96] K. Iwamoto, F. Brachwitz, K. Nomoto, N. Kishimoto, H. Umeda, W. R. Hix, F.-K. Thielemann. Nucleosynthesis in Chandrasekhar Mass Models for Type IA Supernovae and Constraints on Progenitor Systems and Burning-Front Propagation. *ApJS*, 125:439–462 (1999).

[97] P. Höflich, K. Nomoto, H. Umeda, J. C. Wheeler. Influence of the Stellar Population on Type IA Supernovae: Consequences for the Determination of Ω. *ApJ*, 528:590–596 (2000).

[98] I. Domínguez, P. Höflich, O. Straniero. Constraints on the progenitors of type Ia supernovae and implications for the cosmological equation of state. *ApJ*, 557:279 (2001).

[99] D. M. Townsley, A. P. Jackson, A. C. Calder, D. A. Chamulak, E. F. Brown, F. X. Timmes. Evaluating Systematic Dependencies of Type Ia Supernovae: The Influence of Progenitor Ne-22 Content on Dynamics. *ApJ*, 701:1582–1604 (2009).

[100] A. C. Calder, B. K. Krueger, A. P. Jackson, D. M. Townsley, F. X. Timmes, E. F. Brown, D. A. Chamulak. Evaluating Systematic Dependencies of Type Ia Supernovae. *ArXiv e-prints* (2010).

[101] F. K. Röpke, M. Gieseler, M. Reinecke, C. Travaglio, W. Hillebrandt. Type Ia Supernova Diversity in Three-Dimensional Models. *A&A*, 453:203 (2006).

[102] S. Perlmutter, S. Gabi, G. Goldhaber, A. Goobar, D. E. Groom, I. M. Hook, A. G. Kim, M. Y. Kim, J. C. Lee, R. Pain, C. R. Pennypacker, I. A. Small, R. S. Ellis, R. G. McMahon, B. J. Boyle, P. S. Bunclark, D. Carter, M. J. Irwin, K. Glazebrook, H. J. M. Newberg, A. V. Filippenko, T. Matheson, M. Dopita, W. J. Couch, The Supernova Cosmology Project. Measurements of the Cosmological Parameters Omega and Lambda from the First Seven Supernovae at Z $\geq$ 0.35. *ApJ*, 483:565–+ (1997).

[103] O. Straniero, I. Domínguez, G. Imbriani, L. Piersanti. The Chemical Composition of White Dwarfs as a Test of Convective Efficiency during Core Helium Burning. *ApJ*, 583:878–884 (2003).

[104] F. X. Timmes, E. F. Brown, J. W. Truran. On Variations in the Peak Luminosity of Type Ia Supernovae. *ApJ*, 590:L83–L86 (2003).

[105] L. G. Althaus, E. García-Berro, I. Renedo, J. Isern, A. H. Córsico, R. D. Rohrmann. Evolution of White Dwarf Stars with High-metallicity Progenitors: The Role of ^{22}Ne Diffusion. *ApJ*, 719:612–621 (2010).

[106] P. Lesaffre, Z. Han, C. A. Tout, P. Podsiadlowski, R. G. Martin. The C flash and the ignition conditions of Type Ia supernovae. *MNRAS*, 368:187–195 (2006).

[107] A. L. Piro, L. Bildsten. Neutronization during Type Ia Supernova Simmering. *ApJ*, 673:1009–1013 (2008).

[108] D. A. Chamulak, E. F. Brown, F. X. Timmes, K. Dupczak. The reduction of the electron abundance during the pre-explosion simmering in white dwarf supernovae. *ApJ*, 677:160 (2008).

[109] B. Fryxell, K. Olson, P. Ricker, F. X. Timmes, M. Zingale, D. Q. Lamb, P. MacNeice, R. Rosner, J. W. Truran, H. Tufo. FLASH: An adaptive mesh hydrodynamics code for modeling astrophysical thermonuclear flashes. *ApJS*, 131:273–334 (2000).

[110] A. C. Calder, B. Fryxell, T. Plewa, R. Rosner, L. J. Dursi, V. G. Weirs, T. Dupont, H. F. Robey, J. O. Kane, B. A. Remington, R. P. Drake, G. Dimonte, M. Zingale, F. X. Timmes, K. Olson, P. Ricker, P. MacNeice, H. M. Tufo. On Validating an Astrophysical Simulation Code. *ApJS*, 143:201–229 (2002).

[111] P. Colella, P. R. Woodward. The Piecewise Parabolic Method (PPM) for Gas-Dynamical Simulations. *Journal of Computational Physics*, 54:174–201 (1984).

[112] P. Colella, H. M. Glaz. Efficient solution algorithms for the Riemann problem for real gases. *Journal of Computational Physics*, 59:264–289 (1985).

[113] P. MacNeice, K. M. Olson, C. Mobarry, R. de Fainchtein, C. Packer. PARAMESH: A parallel adaptive mesh refinement community toolkit. *Computer Physics Communications*, 126:330–354 (2000).

[114] F. X. Timmes, F. D. Swesty. The Accuracy, Consistency, and Speed of an Electron-Positron Equation of State Based on Table Interpolation of the Helmholtz Free Energy. *ApJS*, 126:501 (2000).

[115] N. Vladimirova, G. Weirs, L. Ryzhik. Flame capturing with an advection-reaction-diffusion model. *Combust. Theory Modelling*, 10(5):727–747 (2006).

[116] A. C. Calder, D. M. Townsley, I. R. Seitenzahl, F. Peng, O. E. B. Messer, N. Vladimirova, E. F. Brown, J. W. Truran, D. Q. Lamb. Capturing the Fire: Flame Energetics and Neutronization for Type Ia Supernova Simulations. *ApJ*, 656:313–332 (2007).

[117] D. M. Townsley, A. C. Calder, S. M. Asida, I. R. Seitenzahl, F. Peng, N. Vladimirova, D. Q. Lamb, J. W. Truran. Flame Evolution During Type Ia Supernovae and the Deflagration Phase in the Gravitationally Confined Detonation Scenario. *ApJ*, 668:1118–1131 (2007).

[118] A. M. Khokhlov. Propagation of turbulent flames in supernovae. *ApJ*, 449:695 (1995).

[119] F. X. Timmes, R. D. Hoffman, S. E. Woosley. An Inexpensive Nuclear Energy Generation Network for Stellar Hydrodynamics. *ApJS*, 129:377–398 (2000).

[120] D. A. Howell, M. Sullivan, E. F. Brown, A. Conley, D. LeBorgne, E. Y. Hsiao, P. Astier, D. Balam, C. Balland, S. Basa, R. G. Carlberg, D. Fouchez, J. Guy, D. Hardin, I. M. Hook, R. Pain, K. Perrett, C. J. Pritchet, N. Regnault, S. Baumont, J. LeDu, C. Lidman, S. Perlmutter, N. Suzuki, E. S. Walker, J. C. Wheeler. The Effect of Progenitor Age and Metallicity on Luminosity and ^{56}Ni Yield in Type Ia Supernovae. *ApJ*, 691:661–671 (2009).

[121] P. Höflich, A. M. Khokhlov, J. C. Wheeler. Delayed detonation models for normal and subluminous type Ia supernovae: Absolute brightness, light curves, and molecule formation. *ApJ*, 444:831–847 (1995).

[122] A. M. Khokhlov, E. S. Oran, J. C. Wheeler. Deflagration-to-Detonation Transition in Thermonuclear Supernovae. *ApJ*, 478:678–+ (1997).

[123] P. Hoeflich, J. C. Wheeler, F. K. Thielemann. Type IA Supernovae: Influence of the Initial Composition on the Nucleosynthesis, Light Curves, and Spectra and Consequences for the Determination of Omega M and Lambda. *ApJ*, 495:617–+ (1998).

[124] J. C. Niemeyer. Can Deflagration-Detonation Transitions Occur in Type IA Supernovae? *ApJ*, 523:L57–L60 (1999).

[125] M. Zingale, S. E. Woosley, C. A. Rendleman, M. S. Day, J. B. Bell. Three-dimensional Numerical Simulations of Rayleigh-Taylor Unstable Flames in Type Ia Supernovae. *ApJ*, 632:1021–1034 (2005).

[126] S. E. Woosley. Type Ia Supernovae: Burning and Detonation in the Distributed Regime. *ApJ*, 668:1109–1117 (2007).

[127] F. K. Röpke. Flame-driven Deflagration-to-Detonation Transitions in Type Ia Supernovae? *ApJ*, 668:1103–1108 (2007).

[128] A. J. Aspden, J. B. Bell, M. S. Day, S. E. Woosley, M. Zingale. Turbulence-Flame Interactions in Type Ia Supernovae. *ApJ*, 689:1173–1185 (2008).

[129] L. Pan, J. C. Wheeler, J. Scalo. The Effect of Turbulent Intermittency on the Deflagration to Detonation Transition in Supernova Ia Explosions. *ApJ*, 681:470–481 (2008).

[130] S. E. Woosley, A. R. Kerstein, V. Sankaran, A. J. Aspden, F. K. Röpke. Type Ia Supernovae: Calculations of Turbulent Flames Using the Linear Eddy Model. *ApJ*, 704:255–273 (2009).

[131] E. Bravo, I. Domínguez, C. Badenes, L. Piersanti, O. Straniero. Metallicity as a Source of Dispersion in the SNIa Bolometric Light Curve Luminosity-Width Relationship. *ApJ*, 711:L66–L70 (2010).

[132] A. Albrecht, G. Bernstein, R. Cahn, W. L. Freedman, J. Hewitt, W. Hu, J. Huth, M. Kamionkowski, E. W. Kolb, L. Knox, J. C. Mather, S. Staggs, N. B. Suntzeff. Report of the Dark Energy Task Force. *ArXiv Astrophysics e-prints*, astro-ph/0609591 (2006).

[133] A. J. Aspden, J. B. Bell, S. E. Woosley. Distributed Flames in Type Ia Supernovae. *ApJ*, 710:1654–1663 (2010).

[134] A. C. Calder, T. Plewa, N. Vladimirova, E. F. Brown, D. Q. Lamb, K. Robinson, J. W. Truran. Deflagrating white dwarfs: a Type Ia supernova model. In *Bulletin of the American Astronomical Society*, vol. 35 of *Bulletin of the American Astronomical Society*, p. 1278 (2003).

[135] D. A. Chamulak, E. F. Brown, F. X. Timmes. The Laminar Flame Speedup by ^{22}Ne Enrichment in White Dwarf Supernovae. *ApJ*, 655:L93–L96 (2007).

[136] W. Fickett, W. C. Davis. *Detonation*. University of California Press, Berkeley (1979).

[137] A. V. Filippenko. Optical Spectra of Supernovae. *ARA&A*, 35:309–355 (1997).

[138] J. S. Gallagher, P. M. Garnavich, P. Berlind, P. Challis, S. Jha, R. P. Kirshner. Chemistry and Star Formation in the Host Galaxies of Type Ia Supernovae. *ApJ*, 634:210–226 (2005).

[139] V. N. Gamezo, A. M. Khokhlov, E. S. Oran. Deflagrations and detonations in thermonuclear supernovae. *Phys. Rev. Lett.*, 92:211102 (2004).

[140] M. Hicken, W. M. Wood-Vasey, S. Blondin, P. Challis, S. Jha, P. L. Kelly, A. Rest, R. P. Kirshner. Improved Dark Energy Constraints from ˜100 New CfA Supernova Type Ia Light Curves. *ApJ*, 700:1097–1140 (2009).

[141] W. Hillebrandt, J. C. Niemeyer. Type IA Supernova Explosion Models. *ARA&A*, 38:191–230 (2000).

[142] G. C. Jordan, IV, R. T. Fisher, D. M. Townsley, A. C. Calder, C. Graziani, S. Asida, D. Q. Lamb, J. W. Truran. Three-Dimensional Simulations of the Deflagration Phase of the Gravitationally Confined Detonation Model of Type Ia Supernovae. *ApJ*, 681:1448–1457 (2008).

[143] D. Kasen, T. Plewa. Spectral Signatures of Gravitationally Confined Thermonuclear Supernova Explosions. *ApJ*, 622:L41–L44 (2005).

[144] A. M. Khokhlov. The structure of detonation waves in supernovae. *MNRAS*, 239:785–808 (1989).

[145] R. P. Kirshner. Foundations of Supernova Cosmology. *ArXiv e-prints* (2009).

[146] E. Kolb, et al. Report of the Dark Energy Task Force. electronic (2006). Http://www.science.doe.gov/hep/DETF-FinalRptJune30,2006.pdf.

[147] H. Lampeitl, R. C. Nichol, H. Seo, T. Giannantonio, C. Shapiro, B. Bassett, W. J. Percival, T. M. Davis, B. Dilday, J. Frieman, P. Garnavich, M. Sako, M. Smith, J. Sollerman, A. C. Becker, D. Cinabro, A. V. Filippenko, R. J. Foley, C. J. Hogan, J. A. Holtzman, S. W. Jha, K. Konishi, J. Marriner, M. W. Richmond, A. G. Riess, D. P. Schneider, M. Stritzinger, K. J. van der Heyden, J. T. Vanderplas, J. C. Wheeler, C. Zheng. First-year Sloan Digital Sky Survey-II supernova results: consistency and constraints with other intermediate-redshift data sets. *MNRAS*, 401:2331–2342 (2010).

[148] M. Livio. The Progenitors of Type Ia Supernovae. In J. C. Niemeyer & J. W. Truran, ed., *Type Ia Supernovae, Theory and Cosmology*, p. 33 (2000).

[149] C. A. Meakin, I. Seitenzahl, D. Townsley, G. C. Jordan, J. Truran, D. Lamb. Study of the Detonation Phase in the Gravitationally Confined Detonation Model of Type Ia Supernovae. *ApJ*, 693:1188–1208 (2009).

[150] J. D. Neill, M. Sullivan, D. A. Howell, A. Conley, M. Seibert, D. C. Martin, T. A. Barlow, K. Foster, P. G. Friedman, P. Morrissey, S. G. Neff, D. Schiminovich, T. K. Wyder, L. Bianchi, J. Donas, T. M. Heckman, Y. Lee, B. F. Madore, B. Milliard, R. M. Rich, A. S. Szalay. The Local Hosts of Type Ia Supernovae. *ApJ*, 707:1449–1465 (2009).

[151] J. C. Niemeyer, A. R. Kerstein. Burning regimes of nuclear flames in SN IA explosions. *NewA*, 2:239–244 (1997).

[152] J. C. Niemeyer, S. E. Woosley. The Thermonuclear Explosion of Chandrasekhar Mass White Dwarfs. *ApJ*, 475:740 (1997).

[153] N. Peters. *Turbulent Combustion*. Cambridge University Press (2000).

[154] A. L. Piro, P. Chang. Convection during the Late Stages of Simmering in Type Ia Supernovae. *ApJ*, 678:1158–1164 (2008).

[155] T. Plewa. Detonating Failed Deflagration Model of Thermonuclear Supernovae. I. Explosion Dynamics. *ApJ*, 657:942–960 (2007).

[156] A. Poludnenko, E. Oran. The interaction of high-speed turbulence with flames: Global properties and internal flame structure. *Combustion and Flame*, 157(5):995–1011 (2010).

[157] A. G. Riess, W. H. Press, R. P. Kirshner. A Precise Distance Indicator: Type IA Supernova Multicolor Light-Curve Shapes. *ApJ*, 473:88–+ (1996).

[158] F. K. Röpke. Multi-dimensional numerical simulations of type Ia supernova explosions (With 7 Figures). In S. Roeser, ed., *Reviews in Modern Astronomy*, vol. 19 of *Reviews in Modern Astronomy*, p. 127 (2006).

[159] F. K. Röpke, S. E. Woosley, W. Hillebrandt. Off-Center Ignition in Type Ia Supernovae. I. Initial Evolution and Implications for Delayed Detonation. *ApJ*, 660:1344–1356 (2007).

[160] W. Schmidt, F. Ciaraldi-Schoolmann, J. C. Niemeyer, F. K. Röpke, W. Hillebrandt. Turbulence in a Three-Dimensional Deflagration Model For Type Ia Supernovae. II. Intermittency and the Deflagration-to-Detonation Transition Probability. *ApJ*, 710:1683–1693 (2010).

[161] I. R. Seitenzahl, C. A. Meakin, D. M. Townsley, D. Q. Lamb, J. W. Truran. Spontaneous Initiation of Detonations in White Dwarf Environments: Determination of Critical Sizes. *ApJ*, 696:515–527 (2009).

[162] I. R. Seitenzahl, D. M. Townsley, F. Peng, J. W. Truran. Nuclear statistical equilibrium for Type Ia supernova simulations. *Atomic Data and Nuclear Data Tables*, 95:96–114 (2009).

[163] S. E. Woosley, S. Wunsch, M. Kuhlen. Carbon Ignition in Type Ia Supernovae: An Analytic Model. *ApJ*, 607:921–930 (2004).

[164] A. P. Jackson, A. C. Calder, D. M. Townsley, D. A. Chamulak, E. F. Brown, F. X. Timmes. Evaluating Systematic Dependencies of Type Ia Supernovae: The Influence of Deflagration to Detonation Density. *ApJ*, 720:99–113 (2010).

[165] D. M. Townsley, S. Asida, T. Jena, D. Q. Lamb. Simulating self-regulated rayleigh-taylor driven flames (2008). In preparation.

[166] W. Schmidt, J. C. Niemeyer, W. Hillebrandt. A localised subgrid scale model for fluid dynamical simulations in astrophysics. I. Theory and numerical tests. *A&A*, 450:265–281 (2006).

[167] W. Schmidt, J. C. Niemeyer, W. Hillebrandt, F. K. Röpke. A localised subgrid scale model for fluid dynamical simulations in astrophysics. II. Application to type Ia supernovae. *A&A*, 450:283–294 (2006).

[168] O. Colin, F. Ducros, D. Veynante, T. Poinsot. A thickened flame model for large eddy simulations of turbulent premixed combustion. *Physics of Fluids*, 12:1843–1863 (2000).

[169] F. Charlette, C. Meneveau, D. Veynante. A power-law flame wrinkling model for les of premixed turbulent combustion part i: non-dynamic formulation and initial tests. *Combustion and Flame*, 131(1-2):159–180 (2002).

[170] F. X. Timmes, S. E. Woosley. The conductive propagation of nuclear flames. I - Degenerate C + O and O + NE + MG white dwarfs. *ApJ*, 396:649–667 (1992).

[171] A. Kolmogorov. The Local Structure of Turbulence in Incompressible Viscous Fluid for Very Large Reynolds' Numbers. *Akademiia Nauk SSSR Doklady*, 30:301–305 (1941).

[172] R. G. Abdel-Gayed, D. Bradley. A Two-Eddy Theory of Premixed Turbulent Flame Propagation. *Royal Society of London Philosophical Transactions Series A*, 301:1–25 (1981).

[173] I. V. Sytine, D. H. Porter, P. R. Woodward, S. W. Hodson, K.-H. Winkler. Convergence Tests for the Piecewise Parabolic Method and Navier-Stokes Solutions for Homogeneous Compressible Turbulence. *Journal of Computational Physics*, 158:225–238 (2000).

[174] R. T. Fisher, L. P. Kadanoff, D. Q. Lamb, A. Dubey, T. Plewa, A. Calder, F. Cattaneo, P. Constantin, I. Foster, M. E. Papka, S. I. Abarzhi, S. M. Asida, P. M. Rich, C. C. Glendening, K. Antypas, D. J. Sheeler, L. B. Reid, B. Gallagher, S. G. Needham. Terascale turbulence computation using the flash3 application framework on the ibm blue gene/l system. *IBM J. Res. Dev.*, 52:127–136 (2008).

[175] P. Yeung, S. Girimaji, S. Pope. Straining and scalar dissipation on material surfaces in turbulence: Implications for flamelets. *Combustion and Flame*, 79(3-4):340 – 365 (1990).

[176] R. Nandkumar, C. J. Pethick. Transport coefficients of dense matter in the liquid metal regime. *MNRAS*, 209:511–524 (1984).

[177] A. R. Kerstein. Prandtl-number dependence of turbulent flame propagation. *Phys. Rev. E*, 64(6):066306 (2001).

[178] T. Poinsot, D. Veynante. *Theoretical and Numerical Combustion*. R.T. Edwards, Inc., Philadelphia, PA, 2nd ed. (2005).

[179] M. Zingale, J. C. Niemeyer, F. X. Timmes, L. J. Dursi, A. C. Calder, B. Fryxell, D. Q. Lamb, P. MacNeice, K. Olson, P. M. Ricker, R. Rosner, J. W. Truran, H. M. Tufo. Quenching processes in flame-vortex interactions. In J. C. Wheeler & H. Martel, ed., *20th Texas Symposium on relativistic astrophysics*, vol. 586 of *American Institute of Physics Conference Series*, pp. 490–492 (2001).

[180] L. J. Dursi, M. Zingale, A. C. Calder, B. Fryxell, F. X. Timmes, N. Vladimirova, R. Rosner, A. Caceres, D. Q. Lamb, K. Olson, P. M. Ricker, K. Riley, A. Siegel, J. W. Truran. The Response of Model and Astrophysical Thermonuclear Flames to Curvature and Stretch. *ApJ*, 595:955–979 (2003).

[181] C. Meneveau, T. Poinsot. Stretching and quenching of flamelets in premixed turbulent combustion. *Combustion and Flame*, 86(4):311–332 (1991).

[182] A. Poludnenko, E. Oran. The interaction of high-speed turbulence with flames: Turbulent flame speed. *Combustion and Flame*, 158(2):301–326 (2011).

[183] F. Ciaraldi-Schoolmann, W. Schmidt, J. C. Niemeyer, F. K. Röpke, W. Hillebrandt. Turbulence in a Three-Dimensional Deflagration Model for Type Ia Supernovae. I. Scaling Properties. *ApJ*, 696:1491–1497 (2009).

[184] S. Jha, A. G. Riess, R. P. Kirshner. Improved Distances to Type Ia Supernovae with Multicolor Light-Curve Shapes: MLCS2k2. *ApJ*, 659:122–148 (2007).